

Quantum Transport and Shot Noise in Graphene-Boron Nitride Heterostructures

Zur Erlangung des akademischen Grades eines
DOKTORS DER NATURWISSENSCHAFTEN
(Dr. rer. nat.)

von der Fakultät für Physik
des Karlsruher Instituts für Technologie (KIT)

genehmigte

DISSERTATION

von

Dipl.-Phys. Jens Mohrmann

aus Wuppertal

Datum der mündlichen Prüfung: 22. April 2016
Referent: Prof. Dr. Hilbert von Löhneysen
Korreferent: Prof. Dr. Ralph Krupke



This document is licensed under the
Creative Commons Attribution 3.0 DE License (CC BY 3.0 DE):
<http://creativecommons.org/licenses/by/3.0/de/>

Contents

1 Introduction	1
2 Theoretical Background	3
2.1 Graphene	3
2.1.1 Basic Properties	3
2.1.2 Electronic Transport, Dirac Fermions, Chirality	4
2.1.3 Graphene in Magnetic Fields	7
2.2 Proximity Induced Superconductivity	9
2.3 Noise	12
2.3.1 $1/f$ Noise, Thermal Noise and Shot Noise	12
2.3.2 Electronic Transport in Mesoscopic Samples	15
2.3.3 Noise at High Frequencies	18
2.3.4 Examples	19
3 Experimental Methods	21
3.1 Sample Fabrication	21
3.1.1 Graphene Sample Fabrication	21
3.1.2 Tunnel Junction Fabrication	28
3.2 Measurement Setup	29
3.2.1 Cryostat	29
3.2.2 DC Measurement	29
3.2.3 Shot Noise Measurement	31
3.2.4 Tunnel Junction Reference Measurements	41
4 Results and Discussion	45
4.1 Ballistic Graphene	46
4.1.1 Basic Characterization	46
4.1.2 Shot Noise	48
4.2 Dirac Fermion Optics	51
4.2.1 Fabry-Pérot Interference	51
4.2.2 Fabry-Pérot Interference in a p-n Junction	54
4.2.3 Shot Noise of a p-n Junction	57

4.2.4 Snake States	59
4.3 High Magnetic Fields	62
4.3.1 Shubnikov-de Haas Oscillations	62
4.3.2 Edge Mode Mixing	67
4.4 Proximity Induced Superconductivity	73
4.4.1 Gate and Temperature Dependence of the Critical Current	73
4.4.2 Current Distribution Analysis	77
4.4.3 Multiple Andreev Reflection	79
5 Summary and Outlook	87
Bibliography	91

Acronyms

Notation	Description
2DEG	two dimensional electron gas
AFM	atomic force microscopy
ALD	atomic layer deposition
GBW	gain bandwidth product
hBN	hexagonal boron nitride
MAR	multiple Andreev reflection
PDMS	polydimethylsiloxane
PMMA	poly(methyl-methacrylate)
PPC	polypropylene carbonate
PVD	physical vapor deposition
QHE	quantum Hall effect
RIE	reactive ion etching
TEM	transmission electron microscopy
VNA	vector network analyzer

CHAPTER 1

Introduction

This thesis presents experiments on electronic transport properties of mesoscopic graphene samples. Recent advancements in sample fabrication techniques, specifically the use of hexagonal boron nitride (hBN) as a substrate [Dea10] and the residue free encapsulation of graphene in hBN [May11; Wan13], have improved the sample quality up to a point where the mean free path is larger than the geometric sample dimensions. In this work, high frequency shot noise was measured in parallel to the conductance of such samples. Shot noise describes current fluctuations that are caused by the fundamental, quantum mechanical randomness of charge transmission. While technically challenging, its measurement reveals information about the charge carrier statistics and the underlying charge transport mechanisms that cannot be found from measurements of the conductance alone.

Graphene, a two dimensional allotrope of sp^2 -hybridized carbon, has attracted a lot of attention since its first experimental isolation in 2004. Due to the linear electronic band structure, charge carriers in graphene can be described as massless Dirac fermions, which leads to a variety of unique phenomena. One example presented in chapter 4.1 is the pseudo-diffusive transport regime at vanishing charge carrier density in graphene, where transport through evanescent modes has been predicted to cause a minimum conductivity despite a vanishing density of states, as well as shot noise comparable to a diffusive conductor, described by a Fano factor of $1/3$. The expected Fano factor and minimum conductivity were found in one sample of graphene on SiO_2 by Danneau et al. [Dan08], but with a weaker than expected gate dependence of the shot noise. On the other hand, DiCarlo et al. [DiC08] found $\mathcal{F} \approx 1/3$ independent of the density (as would be expected for diffusive transport). Recently, Mostovov [Mos14] attempted to clarify this disagreement using an improved measurement setup, yet failed to reach the ballistic regime in their SiO_2 -supported samples.

The wave-particle duality is one of the basic concepts of quantum mechanics. While shot noise is based on the discreteness of charge transport, interference is a hallmark of the wave character. In our clean hBN encapsulated samples, experiments with analogy in optics can be performed, considering both wave optics, as demonstrated by the observation of Fabry-Pérot interference in chapter 4.2, and geometrical optics, where charge transport is described by semi-classical

trajectories that can be manipulated by electrostatic gating and magnetic fields, as presented in chapter 4.2.4. Here, the peculiar properties of graphene come into play, where unimpeded transmission through a p-n barrier is possible due to a relativistic effect called “Klein tunneling” [Kat06b].

Chapter 4.3 presents experiments in a strong magnetic field, where the density of states splits into Landau levels, and charge transport occurs solely through topologically protected edge channels. Due to the ambipolar field effect in graphene, the direction and number of these channels can be tuned using electrostatic gating. In chapter 4.3.2, a graphene p-n junction sample is investigated, where modes can mix at the p-n interface and a transition from ballistic, noiseless conduction in the unipolar regime to enhanced noise in the bipolar regime is expected.

Finally, chapter 4.4 discusses effects of proximity induced superconductivity.

CHAPTER 2

Theoretical Background

2.1 Graphene

2.1.1 Basic Properties

Graphene is an allotrope of sp^2 -hybridized carbon. The three in-plane σ -bonds with bonding angles of 120° form a strictly two-dimensional honeycomb lattice which can be described with a triangular Bravais lattice

$$\mathbf{R} = \sum_{i=1,2} n_i \mathbf{a}_i \quad ; \quad n_i \in \mathbb{Z} \quad (2.1)$$

with primitive lattice vectors

$$\mathbf{a}_1 = \frac{a_b}{2} (3, \sqrt{3}) \quad \mathbf{a}_2 = \frac{a_b}{2} (3, -\sqrt{3}) \quad (2.2)$$

and a two atomic basis

$$\mathbf{r}_1 = (0, 0) \quad \mathbf{r}_2 = \frac{a_b}{2} (1, \sqrt{3}), \quad (2.3)$$

where $a_b = 0.142$ nm is the carbon-carbon distance and $|\mathbf{a}| = \sqrt{3}a_b = 0.246$ nm is the lattice constant. Since the two carbon sites in each primitive cell are not equivalent, they form two sublattices, labeled A and B. The nearest neighbor vectors, connecting the sublattices, are given by

$$\boldsymbol{\delta}_1 = \frac{a_b}{2} (1, \sqrt{3}) \quad \boldsymbol{\delta}_2 = \frac{a_b}{2} (1, -\sqrt{3}) \quad \boldsymbol{\delta}_3 = a_b (-1, 0). \quad (2.4)$$

This leads to a hexagonal reciprocal lattice with basis vectors

$$\mathbf{b}_1 = \frac{2\pi}{3a_b} (-1, -\sqrt{3}) \quad \mathbf{b}_2 = \frac{2\pi}{3a_b} (-1, \sqrt{3}). \quad (2.5)$$

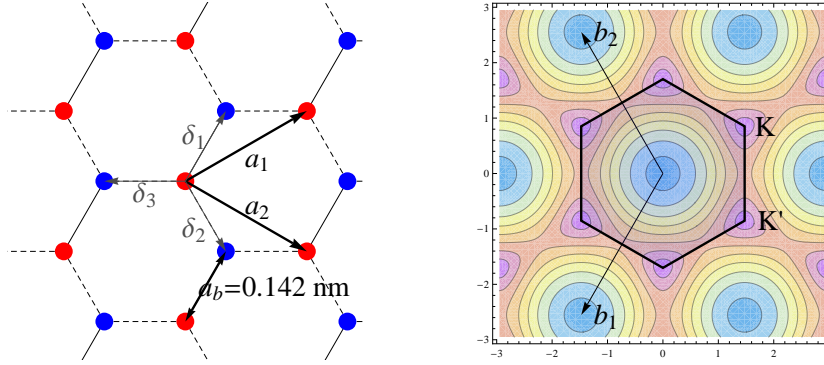


Figure 2.1: Graphene lattice in real space and reciprocal lattice. Red and blue dots indicate A and B sublattices. The reciprocal lattice is shown with an overlay of the first Brillouin zone and a contour plot of the gap between conduction and valence bands.

Compared to the real space lattice, the reciprocal lattice is rotated by 90° , which turn the "zigzag" direction into "armchair" and vice versa.

2.1.2 Electronic Transport, Dirac Fermions, Chirality

Band Structure

The electronic transport properties are governed by the delocalized π -electrons. Their band structure, shown in figure 2.2, can be calculated using the tight-binding approach [Wal47][Rei02].

With nearest-neighbor hopping energy $t \approx 2.8$ eV and next nearest-neighbor hopping energy $t' \approx 0.1$ eV, it can be approximated as (2.2)[Cas09]

$$E(\mathbf{k}) = \pm t \sqrt{3 + f(\mathbf{k})} - t' f(\mathbf{k}) \quad (2.6)$$

$$f(\mathbf{k}) = 2 \cos\left(\sqrt{3}k_y a_b\right) + 4 \cos\left(\frac{\sqrt{3}}{2}k_y a_b\right) \cos\left(\frac{3}{2}k_x a_b\right). \quad (2.7)$$

Here, the plus sign denotes the π^* or conduction band, and the minus sign the π or valence band. The two bands touch each other at two distinct, inequivalent points at the corners of the first Brillouin zone, called \mathbf{K} and \mathbf{K}' and given by

$$\mathbf{K} = \frac{2\pi}{3a_b} \left(1, \frac{1}{\sqrt{3}}\right) \quad \mathbf{K}' = \frac{2\pi}{3a_b} \left(1, -\frac{1}{\sqrt{3}}\right). \quad (2.8)$$

Due to the single electron left in the p_z orbital, the Fermi energy E_F lies exactly in between the bands in undoped graphene (half filling), which makes single layer graphene a zero bandgap semiconductor. The electronic transport properties are governed by the band structure in the vicinity of the \mathbf{K} points. At low energies ($\lesssim 1$ eV), it can be approximated as linear

$$E(\mathbf{k}) = \pm v_F \hbar \mathbf{k}, \quad (2.9)$$

where the Fermi velocity is $v_F = \frac{3ta_b}{2\hbar} \approx c/300 \approx 1 \times 10^6$ m s $^{-1}$. The linear dispersion relation means that the charge carriers in graphene can be treated as massless particles, analogous to the

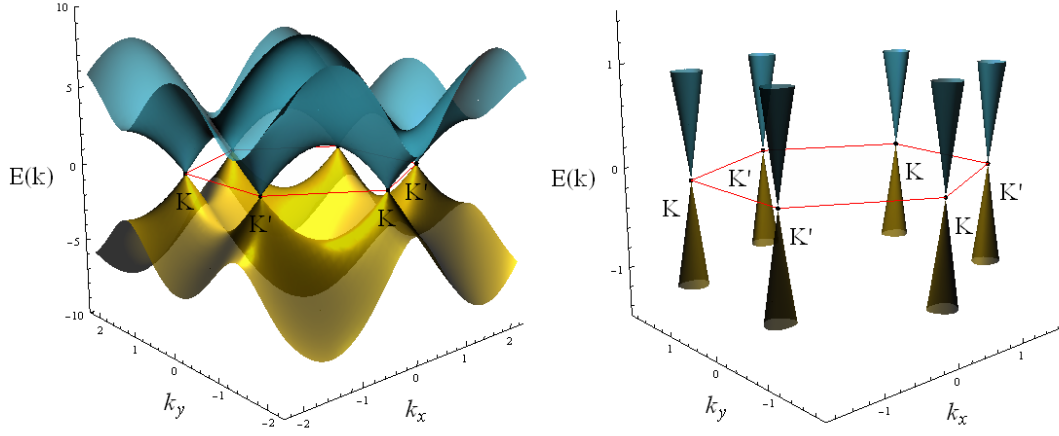


Figure 2.2: Band structure of graphene

dispersion relation of light $E(k) = c\hbar k$. The two independent sublattices cause an additional degree of freedom (“sublattice pseudospin”), which can be treated like the spin by using a two component spinor wave function

$$|\Psi_{\pm, \mathbf{K}}\rangle = \frac{1}{\sqrt{2}} (e^{-i\theta_{\mathbf{k}}/2}, \pm e^{i\theta_{\mathbf{k}}/2}) e^{i\mathbf{k}\cdot\mathbf{r}}. \quad (2.10)$$

Within the linear approximation, the Hamiltonian can be written as

$$\mathcal{H}_{\mathbf{K}} = v_F \boldsymbol{\sigma} \cdot \mathbf{p} \quad \mathcal{H}_{\mathbf{K}'} = -v_F \boldsymbol{\sigma}^* \cdot \mathbf{p} \quad (2.11)$$

where $\boldsymbol{\sigma} = (\sigma_x, \sigma_y)$ is the pseudospin. [Cas09]

The density of states can then be derived as [Cas09; Das11a]

$$\rho(E) = \frac{dN(E)}{dE} = \frac{g_{\text{es}} g_{\text{ps}}}{2\pi(\hbar v_F)^2} A_C |E| \quad \text{with } A_C = 3 \frac{\sqrt{3} a_b^2}{2} \text{ (area of unit cell).} \quad (2.12)$$

From the density of states (2.12) we find the relation of charge carrier density and Fermi energy as

$$n = \frac{N}{A_C} = \frac{1}{A_C} \int_0^{E_F} \rho(E) dE = \int_0^{E_F} \frac{2}{\pi(\hbar v_F)^2} E dE = \frac{E_F^2}{\pi(\hbar v_F)^2} \Rightarrow E_F = \hbar v_F \sqrt{n\pi} \quad (2.13)$$

and

$$k_F = \sqrt{n\pi}, \quad \lambda_F = \frac{2\pi}{k_F} = 2\sqrt{\frac{\pi}{n}}. \quad (2.14)$$

Klein Tunneling

Following the analogy to spin, we can define a helicity operator \hat{h} as the projection of pseudospin σ on the direction of motion:

$$\mathcal{H} |\Psi\rangle = E |\Psi\rangle \Rightarrow \sigma \cdot \mathbf{p} |\Psi\rangle = \pm p |\Psi\rangle \Rightarrow \underbrace{\sigma \cdot \frac{\mathbf{p}}{p}}_{=: \hat{h}} \Psi = \pm |\Psi\rangle. \quad (2.15)$$

For massless particles, helicity is equal to chirality. In graphene, \hat{h} and \mathcal{H} are proportional to each other and share their eigenstates, so chirality is conserved. Chirality/pseudospin is positive for electrons (holes) residing in the \mathbf{K} (\mathbf{K}') valley, and negative for holes (electrons) in the \mathbf{K}' (\mathbf{K}) valley. In this sense, charge carriers in graphene are often referred to as “massless chiral particles”, and in many cases their behavior is fundamentally different than in “ordinary” materials with massive charge carriers. An intriguing example is Klein tunneling, a mechanism that was theoretically proposed for relativistic particles by Klein in 1929 [Kle29], adapted for graphene by Katsnelson et al. [Kat06b] and experimentally observed by Young et al. [You09] and others. It allows relativistic particles to be transmitted through a high barrier with a transmission probability of one. For a potential step that is smooth on the scale of the lattice constant, intervalley scattering $\mathbf{K} \rightarrow \mathbf{K}'$ and vice versa (called “Umklapp” scattering) is suppressed and chirality conserved. Therefore, particles cannot be backscattered $\mathbf{k} \rightarrow -\mathbf{k}$, since chirality conservation would require their sublattice pseudospin to flip, too $\sigma \rightarrow -\sigma$, which would require an external potential that acts differently on the sublattices. For non-perpendicular incidence $k_y \neq 0$, backscattering is allowed with a angle dependent transmission coefficient [Kat06b].

Ambipolar Electric Field Effect

Such a potential barrier can easily be created experimentally. The charge carrier density, and therefore the Fermi energy E_F , can be tuned by applying a voltage V_G to a gate electrode. The gate and the graphene sheet form a plate capacitor, so the induced charge carrier (number) density can be estimated as

$$n = \frac{Q}{|e|A} = \frac{C_G V_G}{|e|A} = \frac{\epsilon_0 \epsilon_r}{\underbrace{|e|d}_{=: \alpha_G}} V_G, \quad (2.16)$$

where $C_G = \epsilon_0 \epsilon_r \frac{A}{d}$ is the gate capacitance, A is the gate area, ϵ_r is the dielectric constant, and d is the thickness of the gate dielectric. The field effect in graphene is “ambipolar”, so by applying a positive or negative gate voltage, either electrons or holes can be induced. In the following, negative n refers to holes, and positive n refers to electrons.

Minimum Conductivity

At $V_G = 0$, where no charge carriers should be present, one might expect a vanishing conductivity. But this is not what is being observed in experiments, and the charge transport mechanisms at vanishing density of states are still not fully understood. It is important to distinguish two cases: diffusive transport in large, disordered samples, and ballistic transport in short and wide samples.

In the first case, the minimum conductivity is caused by a finite local charge carrier density (“charge puddles”) at the global charge neutrality point, created by an inhomogeneous impurity potential. Already in 1998, Shon and Ando [Sho98] calculated a minimum conductivity of $\sigma_{\min} = \frac{4e^2}{\pi h}$ for disordered graphene with impurities with short range potential, independent of scattering strength. In the early experiments, a larger value of $\sigma_{\min}^{\text{Exp}} \approx \frac{4e^2}{h} = \pi \sigma_{\min}^{\text{Theory}}$ was found instead. The discrepancy is attributed to experimental deficiencies, like probe geometry and invasive contacts [Per10].

The finite conductivity of pristine graphene without disorder or in experimental terms, clean, short and wide samples within the ballistic regime has a different origin [Two06]. Here, the transport mechanism changes and charge is transmitted through evanescent modes, which will be explained in more detail in section 4.1.2.

2.1.3 Graphene in Magnetic Fields

Particles with charge $q = e$ moving in a magnetic field \mathbf{B} are subject to the Lorentz force $\mathbf{F}_L = e\mathbf{v} \times \mathbf{B}$. Charge carriers in graphene are confined into a two dimensional electron gas (2DEG), so if the field is applied perpendicular to the graphene plane, it is always perpendicular to the velocity. In semi classical terms, this leads to a circular trajectory. Setting the Lorentz force equal to the centripetal force $F_C = \frac{mv^2}{r}$, we get

$$F_L = F_C \Rightarrow e\mathbf{v}\mathbf{B} = \frac{mv^2}{r_C} = \frac{\hbar kv}{r_C} \Rightarrow eB = \frac{\hbar k}{r_C} \Rightarrow r_C = \frac{\hbar k}{eB}. \quad (2.17)$$

So the charge carriers move along a circular trajectory with cyclotron radius r_C and at the cyclotron frequency

$$\omega_C = \frac{2\pi}{T} = \frac{2\pi v_F}{2\pi r_C} = \frac{eB}{m^*} = \frac{eBv_F}{\hbar\sqrt{\pi n}}, \quad (2.18)$$

with $v = v_F$, and the “relativistic” dynamical mass $m^* = \frac{E}{v_F^2} = \frac{v_F \hbar k_F}{v_F^2} = \frac{\hbar\sqrt{\pi n}}{v_F}$.

Further increasing the field, the cyclotron diameter shrinks below the sample dimensions. When the circumference falls below the mean free path and charge carriers can complete one orbit without scattering, the density of states starts to split into Landau Levels and Shubnikov-de Haas oscillations appear in the conductance. The Bohr-Sommerfeld quantization conditions require the flux $\phi = BA = B\pi r_C^2$ which is enclosed by the orbit to be quantized in units of the flux quantum $\phi_0 := \frac{h}{e}$. This quantization condition only allows cyclotron radii of

$$r_{C,N} = \sqrt{\frac{\phi_0 N}{B\pi}} = \sqrt{\frac{2\hbar N}{eB}} = \sqrt{2N} l_B \quad N \in \mathbb{N} \quad (2.19)$$

with the magnetic length $l_B := \sqrt{\frac{\hbar}{eB}}$ and the density of states splits into Landau levels. In

graphene, the spectra for the two sublattices are given by [Nov05a; Zha05][Goe11]

$$E_N = \pm \sqrt{2e\hbar v_F^2 B \left(N + \frac{1}{2} \pm \frac{1}{2} \right)} \quad N = 0, 1, 2 \dots \quad (2.20)$$

where the first \pm denotes electrons/holes and the second \pm denotes the sublattice pseudospin. The level degeneracy is given by $n_L = \frac{eB}{h}$, and additionally each state is fourfold degenerate with respect to spin ($g_{es} = 2$) and pseudospin ($g_{ps} = 2$), leading to a total of $4n_L$ states at each energy level. The filling factor ν can be calculated from the charge carrier density as

$$\nu = \frac{n}{n_L} = \frac{nh}{eB}. \quad (2.21)$$

Compared to a 2DEG of massive fermions, an additional Landau level appears at zero energy, including both hole and electron like states. Since it is half filled at charge neutrality, it causes a shift of $\frac{1}{2} \cdot 4 = 2$ in ν . This is reflected in the plateaus of the quantum Hall effect (QHE) (fig. 2.3). Due to the fourfold degeneracy, they appear at

$$\sigma_{xy} = 4 \frac{e^2}{h} \left(N - \frac{1}{2} \right) \quad N \in \mathbb{N}, \quad (2.22)$$

i.e. at filling factors $\nu = \pm 2, \pm 6 \dots$, which is referred to as “anomalous quantum Hall effect”.

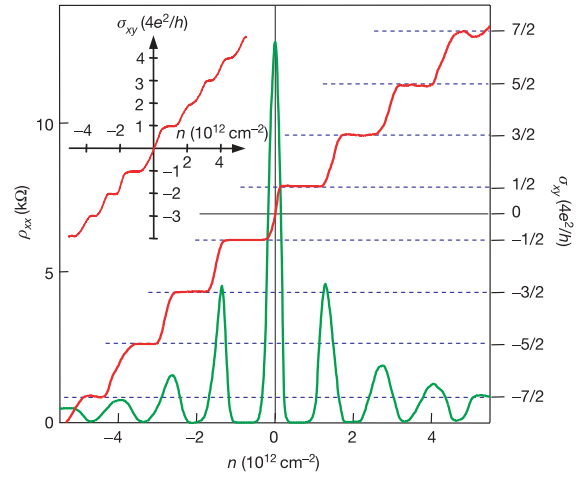


Fig. 2.3: Hall conductivity σ_{xy} and longitudinal resistivity ρ_{xx} of the anomalous QHE in graphene (main image) and QHE in graphene bilayer with normal plateau positions except for a missing plateau at $\nu = 0$ (inset) at $B = 14 \text{ T}$ and $T = 4 \text{ K}$. Source: [Nov05a]

©2005 Nature Publishing Group

2.2 Proximity Induced Superconductivity

In superconducting materials, a fraction of the electrons can condense into a macroscopic quantum state by forming Cooper pairs, as described by the BCS theory[Bar57]. Their collective behavior can then be described by a macroscopic wave function (the order parameter of the phase transition)

$$\Psi(\mathbf{r}, t) = \Psi_0(\mathbf{r}, t) e^{i\theta(\mathbf{r}, t)}, \quad (2.23)$$

normalized to the total number of Cooper pairs $\int \Psi^* \Psi dV = N_S$, such that the absolute square $|\Psi(\mathbf{r}, t)|^2 = \Psi^*(\mathbf{r}, t) \Psi(\mathbf{r}, t)$ describes the local Cooper pair density n_S .

When two superconductors are weakly connected, for example separated by a tunnel junction or a short normal conducting area, a **Josephson junction** is formed. Their wave functions remain separate, but Cooper pairs can be transmitted from one to the other. Below the critical current, the current density across the junction is defined by the phase difference $\varphi = \theta_2 - \theta_1$ according to the first Josephson equation

$$J_S(\varphi) = J_C \sin \varphi, \quad \text{First Josephson equation} \quad (2.24)$$

where J_C is the critical Josephson current density. The phase difference evolves according to the second Josephson equation

$$\frac{\partial \varphi}{\partial t} = \frac{2\pi}{\phi_0} U, \quad \text{Second Josephson equation} \quad (2.25)$$

so that a constant bias U causes an oscillating current with frequency $\frac{f}{U} = \frac{1}{\phi_0} \approx 483.597\,898 \text{ MHz } \mu\text{V}^{-1}$.

Resistively and Capacitively Shunted Junction Model

In a real junction, if the current is increased above the critical current $J > J_C$, a part of it has to be transmitted through additional channels of unpaired quasiparticles (resistive channel, I_N) and as displacement current through the capacitive channel (I_D). Furthermore, the junction dynamics can be influenced by the noise current I_F , so the total current is given by the sum $I = I_S + I_N + I_D + I_F$. Following [Gro10], this situation can be described by the Resistively and Capacitively Shunted Junction (RCSJ) model, with an equivalent circuit as shown in fig. 2.4. Assuming constant resistance R , the dynamics of the phase difference, and therefore the current and voltage, are determined by

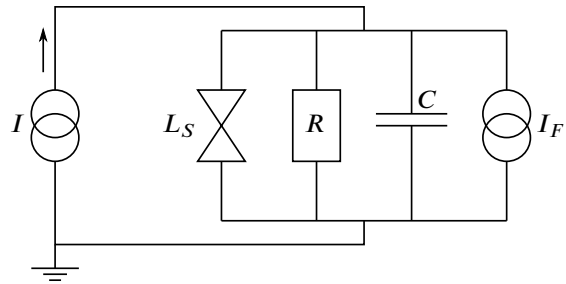


Fig. 2.4: RCSJ model.

an equation of motion

$$\beta_C \frac{d^2\varphi}{d\tau^2} + \frac{d\varphi}{d\tau} + \sin\varphi - \frac{I}{I_C} - \frac{I_F(\tau)}{I_C} = 0 \quad (2.26)$$

with the Stewart-McCumber parameter $\beta_C := \frac{2e}{\hbar} I_C R_N^2 C$ and normalized time $\tau := \frac{\hbar}{2eI_C R}$.

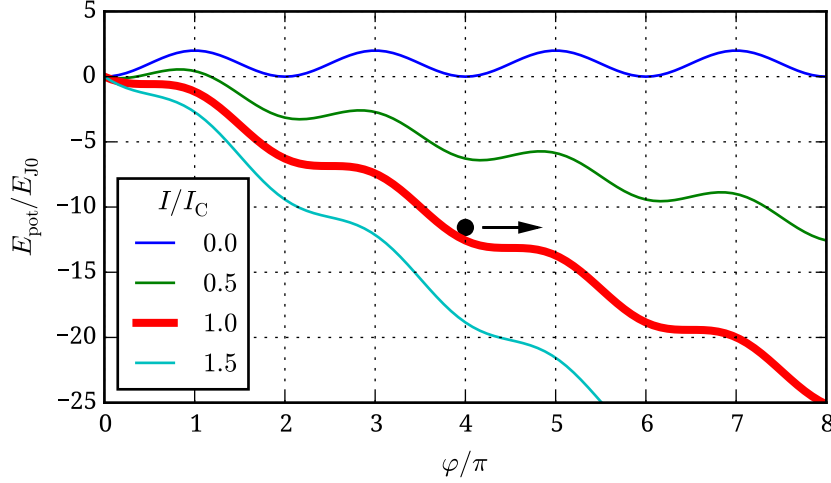


Figure 2.5: The tilted washboard potential of a Josephson junction given by the RCSJ model for various values of I/I_C

The equation is equivalent to a particle with mass $M = \left(\frac{\hbar}{2e}\right)^2 C$ and damping $\eta = \left(\frac{\hbar}{2e}\right)^2 \frac{1}{R}$, moving in a “tilted washboard potential” $E_{\text{pot}} = E_{J0} [1 - \cos\varphi - i\varphi + i_F(t)\varphi]$, with Josephson coupling energy $E_{J0} = \frac{\hbar I_C}{2e}$ (fig. 2.5). The slope of the potential then is given by $\frac{\partial U}{\partial\varphi} = E_{J0} \left[\sin\varphi - \frac{I}{I_C} + \frac{I_F}{I_C} \right] = \frac{\hbar}{2e} [I_F - I + I_C \sin\varphi]$. So, opposed to the ideal Josephson junction in zero voltage state, where the phase continuously increases, the slope of this potential can reach $\frac{\partial U}{\partial\varphi} = 0$ if $I < I_C$ and the phase can get stuck in local minima for $I < I_C$. To restart the motion (i.e. phase evolution), the current has to be increased above I_C , while when the current is decreased from $I > I_C$, the zero voltage state with constant phase difference is reached at a smaller effective I_C . In the picture of the moving particle, the inertia related to the mass term can push the phase difference across the local minima. This behavior shows as hysteresis in the IV-curves. The noise current I_F , for example caused by thermal fluctuations, additionally “shakes” the washboard potential and can make the phase leave a local minimum. Using an externally applied periodic RF signal (typically by exposing the junction to RF radiation), resonance effects called “Shapiro steps” or “Shapiro spikes” can be induced.

Andreev Reflection

The considerations of the previous section hold true for any “weak link”, as long as the transmission occurs in a coherent way. In a junction of two superconductors separated by a normal conducting section (SNS junction), for example a piece of graphene, charge transport through

Andreev Reflection [And64] can fulfill this requirement. Looking at a single normal conductor-superconductor interface, an electron within the normal conducting area cannot enter the superconducting lead if its energy is lower than the superconducting gap Δ , since there are no quasiparticle states available. But instead, it can generate a Cooper pair with charge $2e$, while being retro-reflected as a hole with opposite spin, preserving conservation charge and momentum. Due to time-reversal symmetry, the same process works for an incident hole, which can be reflected as an electron while annihilating a Cooper pair in the superconductor. In a confined region between two superconducting leads, electrons and holes can then be reflected back and forth continuously, forming Andreev bound states that mediate the supercurrent across the normal conductor.

Multiple Andreev Reflection

If the current is increased above I_C , in the voltage state, the charge carriers gain an energy of $\delta E = eV_{DS}$ each time they are transmitted through the normal conductor, and hence can reach the quasiparticle continuum after being transmitted N times, if $N \times eV_{DS} > 2\Delta$ (see fig. 2.6). This process, called multiple Andreev reflection (MAR), allows quasiparticle transmission for energies smaller than $V_{DS} = 2\Delta$ and is responsible for the “subharmonic gap structure” (SGS), i.e. features in the IV curve at positions $V_{DS} = \frac{2\Delta}{N}$.

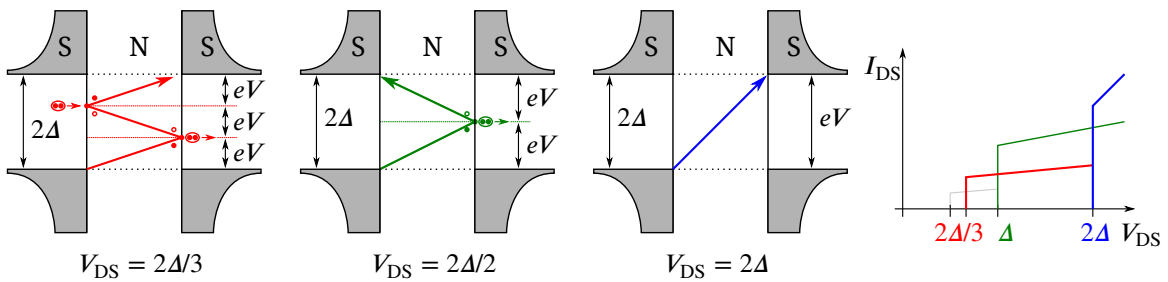


Figure 2.6: Schematic representation of multiple Andreev reflection (MAR). The images on the left show MAR processes for increasing energy $V_{DS} = 2\Delta/N$. The red process corresponds to $N = 3$, where a total charge of $Q = 3e$ is transmitted in the form of one Cooper pair and one quasiparticle. At energies above 2Δ direct transmission of quasiparticles becomes possible (blue). The right image shows a schematic plot of the contributions to the current of each process. For small transmission probabilities, higher order processes are less likely and contribute less (not to scale, based on [Cue99b]).

2.3 Noise

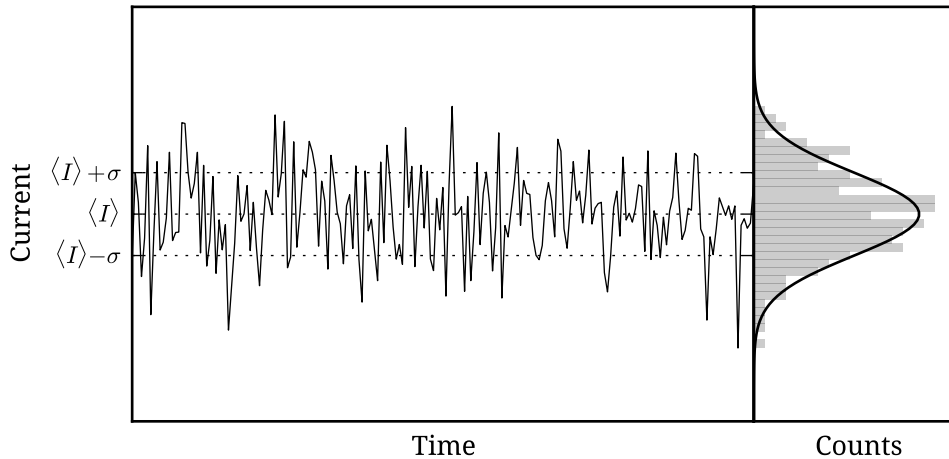


Figure 2.7: The current in a measurement fluctuates around a time averaged value $\langle I \rangle$ with fluctuations δI following a gaussian distribution

Whenever one performs a measurement of a physical quantity, it will be accompanied by random, time dependent fluctuations. For example, the current I through a resistor R could be written as

$$I(t) = \langle I \rangle + \delta I(t), \quad (2.27)$$

where $\langle I \rangle$ denotes the constant average current, with fluctuations $\delta I(t)$. In reality, the average will most likely be the average over a number of measurements at different times, but since the systems we are looking at are assumed to behave “ergodic”, it could just as well be the average over many copies of the system, measured at the same time. Most often, we are not interested in the fluctuating part. In these cases, the fluctuations define the limit of the accuracy of our measurement, and they can even make it impossible if the signal is swallowed by the noise. Sometimes, the term “noise” is being used complementary to “signal”, as something annoying that should be reduced as much as possible. With this definition, it may seem strange to try to measure noise on purpose. But as Landauer stated in 1998 [Lan98], sometimes “the noise is the signal”. To understand why, we have to take a look at where the fluctuations are coming from.

2.3.1 1/f Noise, Thermal Noise and Shot Noise

The first distinction has to be made concerning the source of the measured noise. *External noise*, which is introduced from sources like electromagnetic radiation and the measurement setup itself, obviously is not of interest and thus has to be reduced as much as possible, for example by shielding the measurement setup and by using lock-in techniques. What remains is the *internal noise* that is generated by the sample itself. It can be characterized by looking

at the probability density distribution of the amplitude of the fluctuations, the autocorrelation function $C(\delta t)$, the spectral density function $S(\nu)$ and the Fourier spectrum of the fluctuations themselves $i(\omega)$ [Ihn10].

The *probability distribution*, as shown in figure 2.7, is the histogram of amplitudes of the current. While individual processes can lead to noise with different probability distributions, the total noise will most likely follow a Gaussian distribution. This was pointed out by Landon [Lan41] with respect to the noise in electronics. It is similar to the central limit theorem, which states that the sum of independent random variables with the same arbitrary distribution function will follow a gaussian distribution function. Therefore, the probability distribution of the fluctuation amplitudes will not help distinguishing different components of the total noise.

The *autocorrelation function* $C(\delta t) := \langle \delta I(t) \delta I(t + \delta t) \rangle = \langle \delta I(t = 0) \delta I(\delta t) \rangle$ tells us how fluctuations at one point in time are connected to fluctuations at other times. It can only depend on the time difference between these points, since $\delta I(t)$ is a random function. For large δt , $\lim_{\delta t \rightarrow \infty} C(\delta t) = 0$, and $C(\delta t = 0) = \langle \delta I(t)^2 \rangle$. After Fourier transforming the autocorrelation function, we get the *spectral density* of the current noise

$$\tilde{S}_I(\omega) = \int_{-\infty}^{\infty} e^{-i\omega t} C(\delta I) dt = \int_{-\infty}^{\infty} e^{-i\omega t} \langle \delta I(0) \delta I(\delta t) \rangle dt, \quad (2.28)$$

or with $S_I(\nu) = 2\tilde{S}_I(2\pi\nu)$, where $\omega = 2\pi\nu$

$$\langle \delta I^2 \rangle = \int_0^{\infty} S_I(\nu) d\nu. \quad (2.29)$$

For gaussian white noise, $\sigma_I = \sqrt{\langle \delta I^2 \rangle} = \Delta\nu S_I$. The spectral density can be used for a first classification of the measured noise. Typically, it shows a frequency dependence. In analogy to the colors of light, the $1/f$ part is commonly referred to as “*pink noise*”, while noise with a constant spectral density is called “*white noise*”. In a real measurement, noise cannot be absolutely white, as the lowest frequency will be limited by the measurement time and there will be a cut off at high frequencies when $h\nu \gg k_B T, eV$. In practical measurements, it is more likely to be limited by the bandwidth of the measurement setup.

1/f noise is merely a phenomenological classification. First observed in vacuum tubes by Johnson in 1925 [Joh25], it generally describes noise with a spectral density proportional to $1/f^\alpha$, with α typically ranging from 0.5 to 1.5. $1/f$ noise seems to be ubiquitous in nature and it can be observed in examples as diverse as the water level of the Nile, stock markets, heart beat intervals, and music. It is not determined by a single physical process, but it originates from a more fundamental mathematical reason related to the fractal nature of many phenomena in nature. While the original data from vacuum tubes was explained by Schottky with relaxation processes of trapped surface charges, Bak et al. [Bak87] explain $1/f$ noise more generally by “self-organized criticality”, causing processes where the lifetime of events is linked to their size. Thus, it is hard to directly relate the observed noise in an experiment to physical mechanisms within the sample. A study about $1/f$ noise in graphene has been published by Balandin [Bal13]. While it can be dominant at low frequencies, $1/f$ noise can be avoided by measuring at higher frequencies. The remaining thermal and shot noise originate from distinct physical processes: Random

energies of charge carriers incident to the sample, and quantum mechanical randomness of the transmission of discrete charge carriers through the sample.

Thermal noise was first investigated by Johnson [Joh27], who reported voltage fluctuations resulting from “thermal agitation of the electric charges in the material of the conductor”, and theoretically explained by Nyquist in 1928 [Nyq28]. Using a simple gedankenexperiment of two arbitrary resistors connected in parallel, Nyquist showed that the voltage fluctuations can only be a universal function of frequency, resistance, and temperature, independent of any material properties. If the noise power would depend on any other variable, the second law of thermodynamics could be violated as energy could be transferred from one resistor to the other. The spectral density of the voltage fluctuations caused by thermal noise can be derived from the black-body radiation law [Poz12]

$$\sigma_V = \sqrt{\langle \delta V^2 \rangle} = \sqrt{\frac{4h\nu R \text{BW}}{e^{h\nu/k_B T} - 1}} \approx \sqrt{4k_B T R \text{BW}}, \quad (2.30)$$

with Boltzmann constant $k_B = 1.38065 \times 10^{-23} \text{ J K}^{-1}$, temperature T and resistance R . which is frequency independent (“white”) for $h\nu \ll k_B T$ (Rayleigh-Jeans approximation). With $\langle \delta V^2 \rangle = R\langle \delta I^2 \rangle$, this leads to the spectral density of current noise

$$S_I^{\text{Th}} = \langle \delta I^2 \rangle \text{BW}^{-1} = 4k_B T G \quad \text{Thermal (Johnson-Nyquist) Noise} \quad (2.31)$$

Thermal noise and conductance are linked by the fluctuation-dissipation theorem, which relates equilibrium fluctuations (current noise) to a linear response function (conductance $G = R^{-1}$). While the conductance can usually be measured in an easier way, there are only few methods to access the *electronic* temperature T_e , so the measurement of thermal noise is a valuable primary thermometer (see chapter 3.2.4). Thermal noise is always present in a resistor at finite temperature, and it appears both in and out of equilibrium.

Shot noise, on the other hand, originates from the transmission of discrete charge quanta through the sample. It only appears out of equilibrium and it typically is proportional to the current passing through the sample. It was first measured by Walter Schottky in 1918 [Sch18], who investigated current fluctuations in vacuum tubes. The basic mechanism can be understood from a simple model of a particle hitting a barrier with transmission probability T and reflection probability $R = 1 - T$. If the transmission events of individual particles are independent of one another, the probability of finding n transmitted particles out of N total particles incident on the barrier is given by the binomial distribution

$$P_N(n) = \binom{N}{n} T^n (1 - T)^{N-n} \quad (2.32)$$

where $\binom{N}{n} = \frac{N!}{(N-n)!n!}$. The mean value and variance are:

$$\langle n \rangle = nT \quad (2.33)$$

$$\langle \delta n^2 \rangle = \langle n^2 \rangle - \langle n \rangle^2 = nT(1 - nT) \quad (2.34)$$

For $T \ll 1$, the discrete binomial distribution can be approximated by the *Poisson distribution*

$$P(n) = \frac{\mu^n}{n!} e^{-\mu} \quad \text{Poisson distribution} \quad (2.35)$$

where the mean value $\mu = \langle n \rangle = nT$ is equal to the variance $\sigma^2 = \mu = nT$. The mean current then follows as

$$I = q \langle n \rangle \frac{1}{t_0} = \frac{qnT}{t_0} \quad (2.36)$$

with integration time t_0 , or bandwidth $\Delta\nu = \frac{1}{2t_0}$. From the fluctuations of the number of transmitted particles

$$\langle (\delta n)^2 \rangle = \langle (n - \langle n \rangle)^2 \rangle = \mu = nT \quad (2.37)$$

we get the noise current

$$\langle \delta I^2 \rangle_{t_0} = \langle (I - \langle I \rangle)^2 \rangle = \langle I^2 \rangle - \langle I \rangle^2 = q^2 \delta n^2 \frac{1}{t_0^2} = \frac{q^2}{t_0^2} nT = \frac{q}{t_0} |\langle I \rangle| = 2q |\langle I \rangle| \Delta\nu \quad (2.38)$$

and the spectral density of shot noise

$$S_I^P = 2q |\langle I \rangle| \quad \text{Poisson Value of Shot Noise} \quad (2.39)$$

which is also referred to as the **Poisson value** of shot noise, or as **Schottky formula** [Sch18].

2.3.2 Electronic Transport in Mesoscopic Samples

Eq. 2.39 was derived in a purely classical way, assuming independent particles and a single, defined barrier. On the other hand, a mesoscopic sample is not a single barrier in vacuum. The analogy of charge transmission through a mesoscopic sample to the classical transmission of electrons through a vacuum tube relies on the description of charge carriers as free quasiparticles which get transmitted through the sample *as a whole* through parallel transmission channels, each with a transmission probability T_n according to the Landauer-Büttiker formalism. The total conductance of a two lead conductor is given by

$$G = 2 \frac{e^2}{h} \sum_n T_n \quad \text{Two-terminal Landauer Formula} \quad (2.40)$$

With conductance quantum $G_0 := \frac{e^2}{h}$. Its first version was derived by Rolf Landauer in 1957 and it was further developed and extended by Büttiker and others, especially after the observation of systems with few and perfectly transmitting channels, leading to conductance quantization. From the experimental point of view, according to Landauer's formula (2.40) measuring the conductance of a sample means measuring the total sum of the transmission probabilities of all channels. The total shot noise of the sample is generated by the "parallel connection" of all transmission channels. Here, the approach following [Bla00] is outlined.

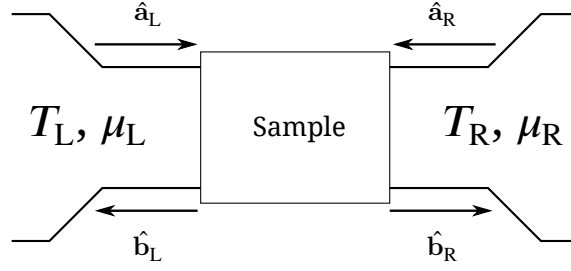


Figure 2.8: Reservoirs and scattering states in a two lead conductor. Source: Adapted from [Bla00]

2.8 shows the schematic image of a two lead sample. The sample is connected to the reservoirs denoted by L and R, each characterized by their total number of channels $N_{L/R}$, temperatures $T_{L/R}$ and electrochemical potentials $\mu_{L/R}$, where a bias voltage can be introduced as $eU = \mu_L - \mu_R$. States in the reservoirs are occupied according to the Fermi distribution function

$$f_\alpha(E) = \left(e^{\frac{E-\mu_\alpha}{k_B T}} + 1 \right)^{-1} \quad \alpha = L, R. \quad \text{Fermi distribution function} \quad (2.41)$$

The creation and annihilation operators of incoming states $\hat{a}_{L,R}^{(\dagger)}$ and outgoing states $\hat{b}_{L,R}^{(\dagger)}$ are related by the $(N_L + N_R) \times (N_L + N_R)$ dimensional scattering matrix s (s^\dagger):

$$\begin{pmatrix} \hat{b}_{L1} \\ \vdots \\ \hat{b}_{LN_L} \\ \hat{b}_{R1} \\ \vdots \\ \hat{b}_{RN_R} \end{pmatrix} = s \begin{pmatrix} \hat{a}_{L1} \\ \vdots \\ \hat{a}_{LN_L} \\ \hat{a}_{R1} \\ \vdots \\ \hat{a}_{RN_R} \end{pmatrix} \quad \text{with} \quad s = \begin{pmatrix} r & t' \\ t & r' \end{pmatrix} \quad (2.42)$$

For the charge transport, the off-diagonal block t of the scattering matrix which links incoming states from the left lead to outgoing states in the right lead is crucial. The transmission probabilities T_n in eq. 2.40 are the eigenvalues of t (at the Fermi energy E_F)

$$\sum_n T_n = \text{Tr} [t^\dagger t] \quad (2.43)$$

The eigenstates corresponding to the T_n , i.e. the transmission channels, are superpositions of the incoming and outgoing states $\hat{a}_{L,R}^{(\dagger)}$ and $\hat{b}_{L,R}^{(\dagger)}$.

Noise and Transmission Probabilities

The spectral density of current fluctuations can be calculated in analogy to eq. (2.28) as the Fourier transform of the correlation function ($\alpha, \beta \in \{L, R\}$)

$$2\pi\delta(\omega - \omega') S_I^{\alpha\beta}(\omega) := \langle \Delta \hat{I}_\alpha(\omega) \Delta \hat{I}_\beta(\omega') + \Delta \hat{I}_\beta(\omega') \Delta \hat{I}_\alpha(\omega) \rangle. \quad (2.44)$$

For a two lead conductor, it is given by

$$S_I = 2 \frac{e^2}{h} \sum_n \int dE \{ T_n(E) [f_L(1 \mp f_L) + f_R(1 \mp f_R)] \pm T_n(E) [1 - T_n(E)] (f_L - f_R)^2 \} \quad (2.45)$$

where f denotes either the Fermi (upper signs) or the Bose-Einstein distribution function (lower signs).

In the simplest case of zero temperature ($T = 0$, $f = \theta$) and zero frequency ($\omega = 0$)

$$S_I = 2 \frac{e^2}{h} \text{Tr} [r^\dagger r t^\dagger t] e|U| \quad (2.46)$$

or in the basis of eigen channels

$$S_I^{\text{LL}} = 2 \frac{e^2}{h} e|U| \sum_n T_n(1 - T_n) = 2e\langle I \rangle \frac{\sum_n T_n(1 - T_n)}{\sum_n T_n}. \quad (2.47)$$

Comparing eq. (2.47) to the conductance $G = 2 \frac{e^2}{h} \sum_n T_n$ (2.40), we see that the shot noise at zero temperature contains information about transmission probabilities beyond the total sum given by the conductance. A practical key figure called the *Fano Factor* \mathcal{F} can be defined as the ratio of actual shot noise versus the Poissonian value $S_I^{\text{P}} = 2e\langle I \rangle$ (2.39).

$$\mathcal{F} := \frac{S_I}{S_I^{\text{P}}} = \frac{q}{e} \frac{\sum_n T_n(1 - T_n)}{\sum_n T_n} \quad \text{Fano Factor} \quad (2.48)$$

Thus, $\mathcal{F} = 0$ for $T_n \equiv 0$ or $T_n \equiv 1$, and $\mathcal{F} \leq 1$. The factor $\frac{q}{e}$ appears because the quasiparticle charge q may be different from the electron charge e , a fact that was neglected in the derivations so far. This proportionality of the spectral density of shot noise to the size of the transmitted charge quanta can be used to directly measure the quasiparticle charge. The right hand side of (2.48) is only valid for energy independent T_n . In the general case, the Fano factor cannot be expressed in the form of transmission probabilities.

Finite Temperature

By taking the Fermi distribution of the occupation number of the incident states into account, and for energy independent transmission probabilities, a formula combining thermal noise and

shot noise can be derived [Khl87].

$$S_I = 2 \frac{e^2}{h} \left[2k_B T \sum_n T_n^2 + eV \coth \left(\frac{eV}{2k_B T} \right) \sum_n T_n (1 - T_n) \right] \quad (2.49)$$

$$= 4k_B T \frac{1}{R} \left[(1 - \mathcal{F}) + \mathcal{F} \frac{eV}{2k_B T} \coth \left(\frac{eV}{2k_B T} \right) \right] \quad (2.50)$$

At zero temperature, (2.47) is recovered, and at zero bias $V = 0$ we recover the thermal noise (2.31)

$$\lim_{eV \rightarrow 0} S_I = 2 \frac{e^2}{h} \left(2k_B T \sum_n T_n^2 + 2k_B T \sum_n (T_n - T_n^2) \right) = 4k_B T G \quad (2.51)$$

since $\lim_{x \rightarrow 0} \{x \coth(x)\} = 1$.

Using equation (2.50), the electronic temperature T_e can be derived from the shape of the noise curve [Spi03].

2.3.3 Noise at High Frequencies

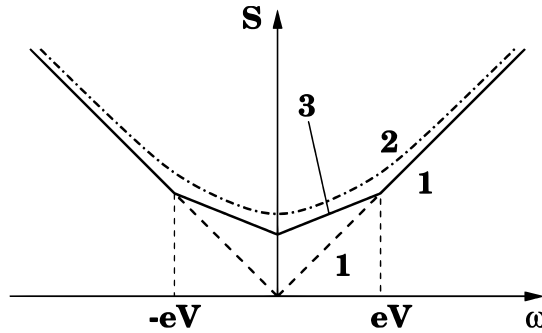


Figure 2.9: Frequency dependence of shot noise at finite (2) and zero temperature (1 and 3). (1) and (3) correspond to the lower and upper line of equation (2.54). Source: [Bla00] ©2000 Elsevier Science B.V.

In the previous section, the noise was calculated in the “zero frequency limit” at $\omega = 0$. But the typical bandwidth in our measurement setup is 4 GHz to 8 GHz, corresponding to a temperature of approximately $T = \frac{h\nu}{k_B} = 190 \text{ mK}$ to 380 mK , which is in the same order of magnitude as the temperatures we can expect to reach in our experiments. For arbitrary frequencies, voltages and temperatures, the spectral density of current noise is given by [Bla00; Büt92]

$$S_I(\omega) = 2 \frac{e^2}{h} \left\{ 2\hbar\omega \coth \left(\frac{\hbar\omega}{2k_B T} \right) \sum_n T_n^2 + \left[(\hbar\omega + eV) \coth \left(\frac{\hbar\omega + eV}{2k_B T} \right) + (\hbar\omega - eV) \coth \left(\frac{\hbar\omega - eV}{2k_B T} \right) \right] \sum_n T_n (1 - T_n) \right\}. \quad (2.52)$$

While $\omega = 0$ reproduces equation (2.49), setting $V = 0$ leads to the frequency dependent thermal

noise

$$S_I^{\text{eq}}(\omega) = \frac{e^2 \omega}{\pi} \coth\left(\frac{\hbar \omega}{2k_B T}\right) \sum_n T_n = \frac{\hbar \omega}{R} \coth\left(\frac{\hbar \omega}{2k_B T}\right) \quad (2.53)$$

and $T = 0$ results in

$$S_I(\omega) = 2 \frac{e^2}{h} \begin{cases} \hbar |\omega| \sum_n T_n^2 + eV \sum_n T_n(1 - T_n), & \hbar |\omega| < eV, \\ \hbar |\omega| \sum_n T_n = \hbar |\omega| G, & \hbar |\omega| > eV. \end{cases} \quad (2.54)$$

Thus, at very high frequencies, the shot noise is no longer “white”, as shown in fig. 2.9.

2.3.4 Examples

Figure 2.10 shows the conductance and shot noise of a **quantum point contact**, i.e. a constriction in a 2DEG where the conductance can be controlled to single conductance quanta by tuning the potential of a split gate structure. For ballistic transport, the transmission probability is $T_n = 1$, so we expect noiseless conduction within the conductance plateaus. Maxima in the noise appear only during the transition from one plateau to the next, where a new channel appears. Experiments confirming this prediction by Lesovik [Les89] were carried out by Reznikov et al. [Rez95] and Kumar et al. [Kum96].

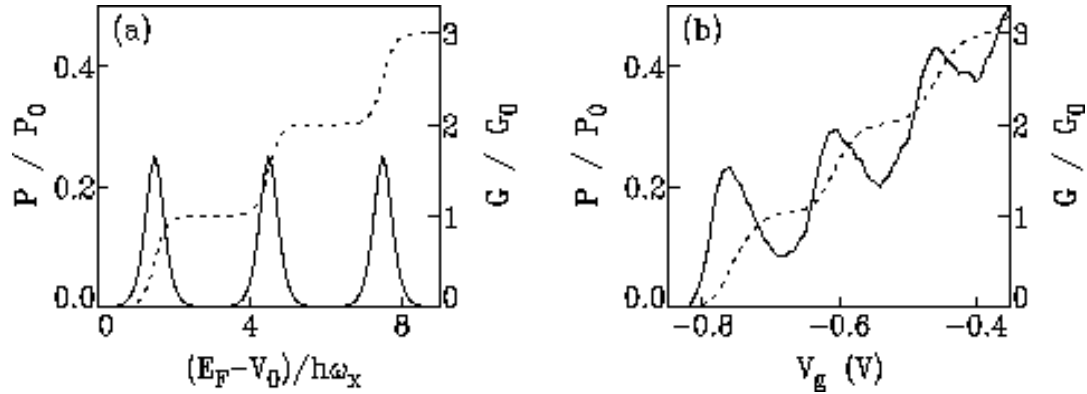


Figure 2.10: (a) Calculated and (b) measured conductance (dashed) and shot noise (solid) of a QPC with respect to Fermi energy / gate voltage. Source: Unpublished data from Reznikov *et al.* (similar to [Rez95]), cited from [Jon97] ©1997 Springer Science+Business Media Dordrecht

The use of the noise of a tunnel junction as a **primary thermometer** was investigated by Spietz et al. [Spi03]. While the electronic temperature can also be measured using only the thermal noise $S_I^{\text{Th}} = \frac{4k_B T}{R}$, measuring the shot noise has the advantage that no separate calibration of additional noise, gain and bandwidth of the amplifier chain are required, since these values can be deduced from the shot noise measurement itself.

Examples for **determination of quasiparticle charge** are the observation of superpoissonian noise in superconductor-normal metal junctions (Nb-Cu), where the Cooper pair charge of $q = 2e$ causes doubling of the noise power [Jeh00], and the experiments by Saminadayar et al. and De-Picciotto et al. proving the $e^* = \frac{1}{3}$ Laughlin quasiparticle charge in the Fractional Quantum

Hall Effect [DeP98; Sam97].

Another interesting example is a **mesoscopic diffusive nanowire** [Bla00]. Macroscopic conductors don't show shot noise because current fluctuations are smoothed out by electron-phonon scattering. But if the size of the system is reduced, different regimes can be identified from the shot noise. The relevant length scales are the elastic mean free path l_{mfp} , the dephasing length L_φ , the electron-electron scattering length $L_{\text{e-e}}$, and the electron-phonon scattering length $L_{\text{e-ph}}$, where usually $l_{\text{mfp}} < L_\varphi < L_{\text{e-e}} < L_{\text{e-ph}}$. Typical values for these lengths are 50 nm, 1 μm , 10 μm , and 10 mm for metal at 50 mK. Figure 2.11 shows the calculated shot noise of a metallic thin film resistor with respect to its length L . For ballistic transport at $L \ll l_{\text{mfp}}$ and for $L \gg L_{\text{e-ph}}$, the shot noise disappears. For $L_{\text{e-e}} \ll L \ll L_{\text{e-ph}}$ electron heating and thermalization through the contacts lead to thermal noise, giving rise to $\mathcal{F} = \frac{\sqrt{3}}{4}$. Within the metallic diffusive regime $l_{\text{mfp}} \ll L \ll L_\xi$, with elastic mean free path l_{mfp} , localization length $L_\xi = N_T l$ and number of transverse channels N_T , the transmission probabilities follow the distribution function

$$P(T) = \frac{l_{\text{mfp}}}{2L} \frac{1}{T\sqrt{1-T}}, \quad T_{\text{min}} < T < 1 \quad \text{with } T_{\text{min}} = 4e^{-2L/l_{\text{mfp}}} \quad \text{and} \quad P(T) = 0 \quad \text{otherwise.} \quad (2.55)$$

This leads to a universal result of $\mathcal{F} = \frac{1}{3}$ for metallic diffusive wires, which has been observed experimentally by [Bee92],[Lie94; Ste96]. Coincidentally, the same Fano factor is expected for a ballistic graphene strip, as will be explained in more detail in section 4.1.2.

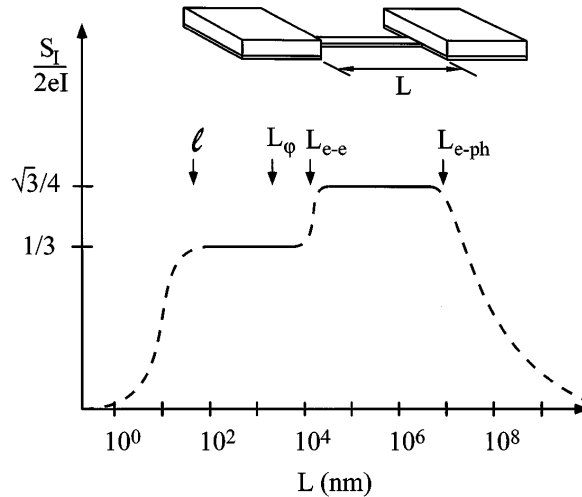


Figure 2.11: Calculated shot noise of a metallic nanowire. Source: [Ste96]
©1996 American Physical Society

CHAPTER 3

Experimental Methods

3.1 Sample Fabrication

3.1.1 Graphene Sample Fabrication

Soon after the first successful isolation of graphene monolayers in 2004, Novoselov et al. [Nov05b] started applying the “Scotch-Tape” technique to other layered materials, already including hBN. At that time, silicon wafers with 300 nm thermally grown SiO₂ were the substrate of choice, since interference in the oxide layer increases the optical contrast of graphene, allowing the identification of monolayers among thicker graphite pieces after exfoliation. With the development of transfer techniques for graphene, starting in 2008 [Rei08], new possibilities to investigate the influence of different substrates on graphene were opened up. A tremendous improvement of sample quality was reached by Dean et al. [Dea10] by combining graphene and hexagonal boron nitride, an atomically flat, insulating isomorph of graphite. Since it can only be synthesized as powder of millimeter size crystals [Tan07][Wat04], direct exfoliation onto hBN would not have been practically possible. With this breakthrough, the possibilities and the importance of the ability to transfer and manipulate 2d crystals became obvious, eventually giving rise to a new research field of “van-der-Waals heterostructures” [Gei13]. Mayorov et al. encapsulated graphene in hBN by transferring first graphene onto a hBN crystal, and then another hBN crystal on top of graphene. While the deposition of material onto graphene generally deteriorates its properties, hBN encapsulation was shown to not only protect the graphene from the environment, but to even further improve the mobility [May11]. The latest advancement was introduced by Wang et al., who found a way to encapsulate graphene in hBN without introducing any impurities in the process. This technique, which was employed for the sample fabrication in this thesis, works by starting the stack from the top hBN and using it to pick up the graphene and bottom hBN. Using this technique, a mean free path of up to 15 μm was found [Wan13].

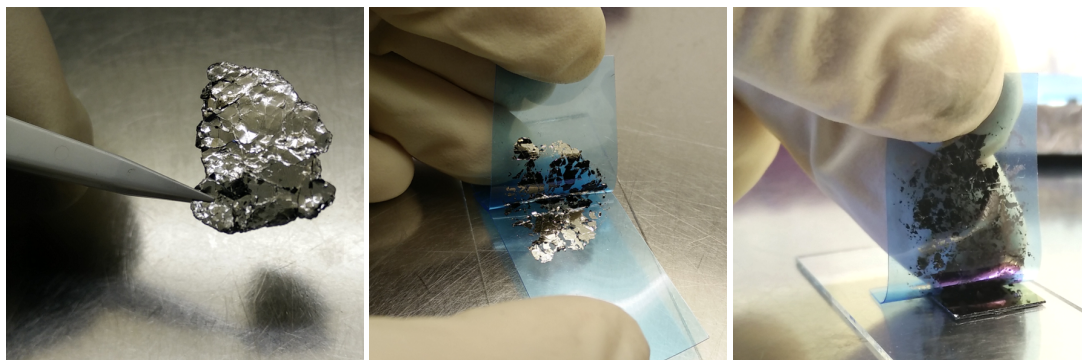


Figure 3.1: Manufacturing graphene by exfoliation of a natural graphite crystal using the “Scotch Tape Technique”

Mechanical Exfoliation

Even though more than 10 years have passed since the first isolation of graphene by André Geim and Konstantin Novoselov using the “Scotch Tape Technique” [Nov04][Zha05], this original manufacturing technique remains the source of the cleanest, highest quality graphene. In short, first, a macroscopic, single crystal of natural graphite is attached to an adhesive tape¹ (fig. 3.1 panel 1), and thinned down by repeatedly exfoliating it with further pieces of tape (panel 2). Once the graphite on the tape starts to become transparent, it is pushed against the surface of a Si wafer with 300 nm of thermally grown SiO₂. Due to the van-der-Waals interaction between the wafer surface and the graphite, parts of the graphite get stuck on the surface and are separated from the bulk crystal (panel 3). The amount of graphite that is exfoliated in this step was found to heavily depend on the humidity and the cleaning process of the wafer. The standard cleaning process using O₂ plasma renders the surface hydrophilic due to the creation of polar silanol (SiOH) groups, which reduces the adhesion of graphite. In this work, an additional cleaning step using a CO₂ snow jet [She94] was introduced to lower the hydrophilicity. Here, liquid CO₂ is released from a small nozzle and immediately solidifies into a high pressure stream of gas and tiny CO₂ crystals. This stream is directed onto the heated (about 100 °C) substrate, passivating and mechanically cleaning its surface. This turns the surface hydrophobic, reduces the dependency on humidity and drastically increases the yield of graphite and graphene. After the exfoliation, the wafer is inspected using an optical microscope, where the SiO₂ layer helps increasing the contrast through interference effects [Rod07] and makes it possible to easily distinguish crystals of one, two or more layers. The number of layers and the cleanliness of the crystal are verified using Raman spectroscopy and AFM.

The same mechanical exfoliation process was used for the fabrication of thin hBN crystals. The raw material of the presented samples was produced by Kenji Watanabe and Takashi Taniguchi at high pressure (1.5 GPa) and high temperature (1500 °C) at the National Institute for Materials Science (NIMS), Japan [Tan07][Wat04]. In other samples, commercially available hBN powder was used (produced by Momentive, product PT110) with no negative effect on the sample quality.

¹ Nitto Denko “elp bt-150E-CM”

Fabrication Process, Transfer of 2D Crystals, One Dimensional Contacts

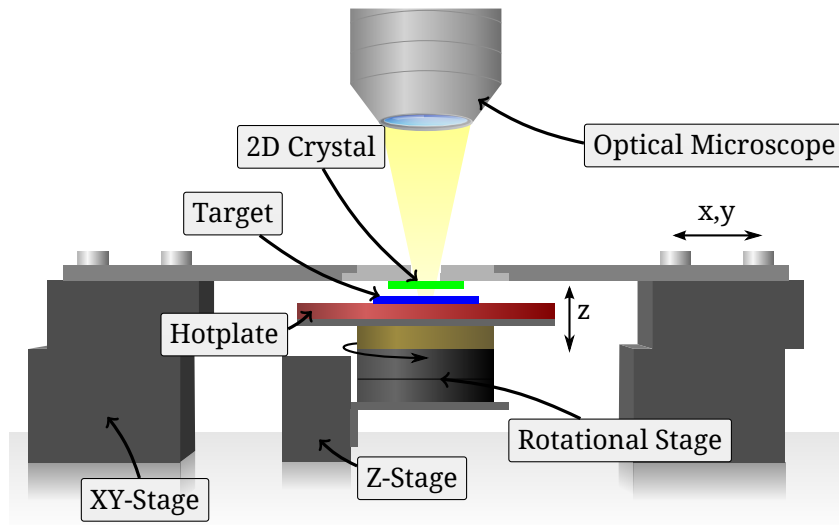
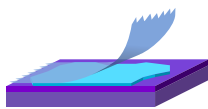


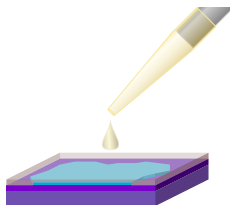
Figure 3.2: Alignment Setup [Moh11].

Before the fabrication of the van-der-Waals heterostructure started, sapphire wafers which were to be used as substrates for the final samples were prepatterned with Au back gate structures and markers using electron beam lithography and PVD of a double layer of 5 nm Cr and 30 nm Au in an electron-beam evaporation system. The back gate structures were then covered by 20 nm of Al_2O_3 grown by atomic layer deposition (ALD) (182 cycles at 200 °C) to prevent gate leakage through cracks in the lower hBN layer. The sapphire wafers and additional Si/SiO₂ wafers were cleaned by rinsing them in acetone and isopropanol, oxygen plasma cleaning and further CO₂ snow jet cleaning for the Si/SiO₂ substrates that were to be used for exfoliation.

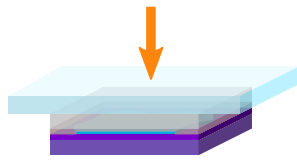
Our standard "pick-up" process for making van-der-Waals heterostructures by stacking 2d crystals [Moh11][Bor13][Du15], based on [Dea10][Wan13], follows these steps:



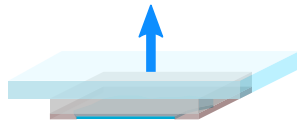
The raw material is exfoliated onto Si/SiO₂ wafers. The 300 nm SiO₂ layer enhances the contrast for single layer graphene and helps estimating the thickness of hBN. After exfoliation, suitable crystals are selected by optical inspection and AFM. To make room for the metal leads in the final sample, unwanted surrounding graphite and hBN crystals are carefully removed using a piece of paper and a toothpick.



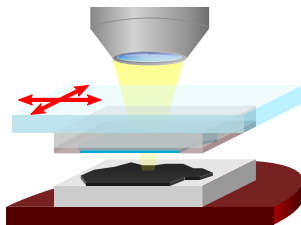
The wafer piece with the hBN crystal that was chosen as the top layer is spin coated with 7 % wt. PPC in Ethyl-Acetate at 4000 rpm and baked at 100 °C for 10 minutes to evaporate the solvent.



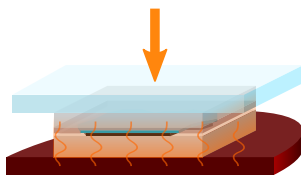
The PPC then forms a relatively rigid, thick layer. After scratching away PPC around the edges of the wafer piece to remove PPC that had flown around them, a roughly 0.5 mm thick PDMS stamp prepared in advance is pressed on the wafer piece with a glass slide.



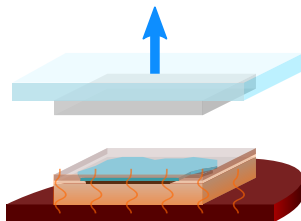
The PDMS sticks to the PPC, and the 2d crystal can be lifted from the substrate by carefully pulling away the PPC/PDMS stack.



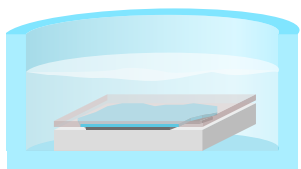
This 2d-crystal/PPC/PDMS stack is then attached to a glass slide and mounted into the transfer setup (fig. 3.2), where it can be aligned onto the target substrate, which is attached to a hotplate underneath, using a xy-stage.



The 2d crystal/PPC/PDMS stack is slowly lowered onto the target, while continuously monitoring through the optical microscope and re-aligning. Once contact is made, the hotplate is heated to 140 °C, which softens the PPC and flattens out remaining wrinkles or bubbles.



The heat also weakens the bond between PDMS and PPC and allows to detach the PDMS and glass slide.



The PPC can now be picked up again, together with the stack of 2d-crystals (back to step 3). If it shows cracks or other damage, it is dissolved in acetone and new PPC is spin-coated for the next transfer step (back to step 2).



The process is repeated with different materials until the desired heterostructure is completed. The final structure is annealed at 280 °C in air for about 3 h.

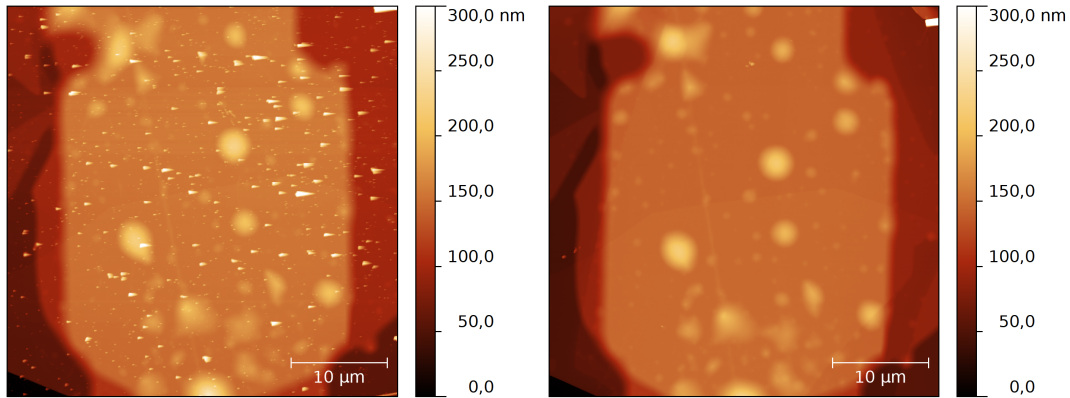


Figure 3.3: AFM images of hBN-graphene-hBN triple layer on metal back gate showing “bubbles” of accumulated impurities and the effect of annealing. The bright, square area is the Au back gate, other edges are edges of top and bottom hBN crystals. The graphene covers almost the entire back gate, the substrate is only visible in the lower left corner. **(l)** after transfer **(r)** after annealing in air at 280 °C for 3 h

The product of the stacking process is a triple-layer hBN-graphene-hBN “sandwich” on top of an Au back gate. As was shown in a study using transmission electron microscopy (TEM) by Haigh et al. [Hai12], the interfaces of hBN and graphene turn out to be surprisingly clean, thanks to a self-cleaning effect which is further enhanced by thermal annealing. Remaining residues, mostly hydrocarbons, accumulate in distinct regions that are easily visible as “bubbles” in AFM images (fig. 3.3). By simply designing the structures within the atomically flat and clean areas in between them, perfectly clean and flat samples can be made. While this process leads to the best quality substrate-supported graphene, the downside is that the random distribution and shapes of exfoliated crystals and the random appearance of wrinkles and bubbles after the transfer make every sample unique. Therefore, every sample requires individual planning and design of the metallic contact and gate structures.

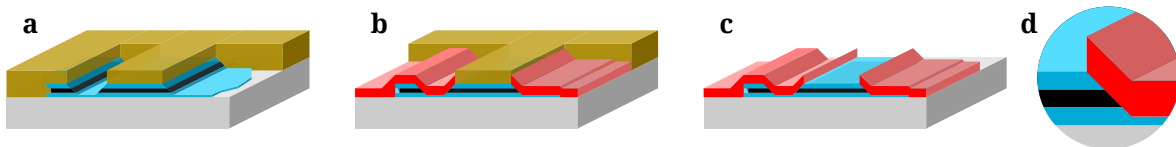


Figure 3.4: One-dimensional edge-connections. **(a)** reactive ion etching (RIE) of trenches into hBN. **(b)** Metal deposition. **(c)** Connected device. **(d)** Close up of 1-d contact

The electrical connections to the graphene layer were made through “**one-dimensional edge-contacts**” [Wan13]. Since the graphene is completely encapsulated, it cannot be connected directly. Instead, RIE was used to etch trenches or holes into the hBN-graphene-hBN triple layer, followed by physical vapor deposition (PVD) of 10 nm Ti / 80 nm Al. While [Wan13] used a separate lithography step and a hydrogen-silsesquioxane (HSQ) mask for the etching step, here etching and metal deposition were done using the same PMMA mask, and only a single lithography step. This ensures that there is no overlap of the contact metal and the active area, allowing a top gate that is effective up to the edge of the graphene. For sample B, the lithography was divided into two sub-steps in an attempt to create a sample with Corbino geometry, which

typically requires an air bridge to connect the center electrode. In the first step, only the regions where the graphene was to be connected were exposed, and holes were etched through the top hBN layer, graphene and part of the lower hBN layer using RIE (40 sccm CHF_3 , 4 sccm O_2 , 60 mTorr, 60 W, 2.5 min, etch rate 48 nm min^{-1} PMMA, 23 nm min^{-1} hBN). Then, the same PMMA mask was exposed again, this time defining the leads and bonding pads, followed by a short O_2 plasma to clean the exposed edge and finally the metal deposition. The leads defined in the second lithography step are isolated from the graphene by the top hBN layer and thus could be used instead of air-bridges to connect a center electrode.

After depositing the contacts, another electron beam lithography step and RIE was used to etch the triple layer into the desired rectangular shape. In sample B, a top gate covering half of the length of the channel was added by growing another 20 nm of Al_2O_3 using ALD, defining the pattern using electron beam lithography and depositing 10 nm Ti/80 nm Al. Due to the edge-connection and reusing the PMMA mask, the top gate can be effective up to the edge of the graphene channel, forming only a single p-n junction. The Al_2O_3 layers are separated from the graphene channel by the hBN crystals, so charge traps that typically impair the carrier mobility cannot influence the transport. Since the top gate and one of the electrodes are only separated by the Al_2O_3 layer, the thickness of this layer (20 nm) limits the maximal possible gate voltage, independent of the hBN thickness.

Figure 3.6 shows AFM images of the devices “A” and “B” whose data is presented in this thesis, table 3.2 shows the sample parameters.

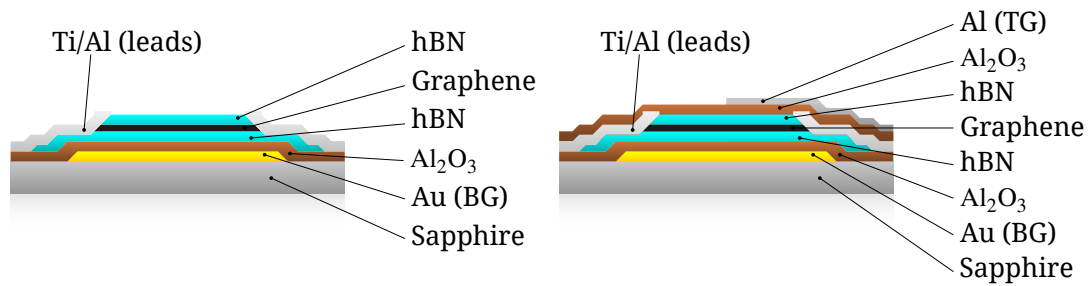


Figure 3.5: Schematic cross-sections of samples A and B

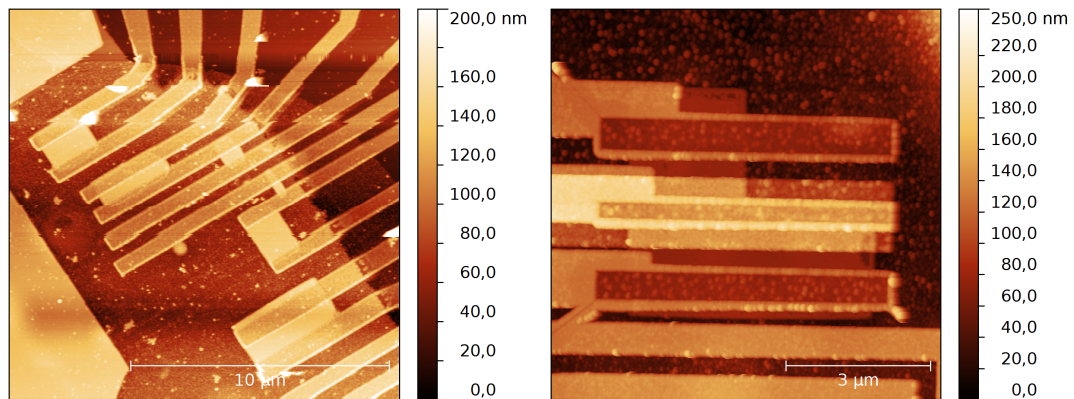


Figure 3.6: AFM images of samples A and B

Parameter	Sample A	Sample B
Width	3.0 μm	5.0 μm
Length	350 nm	1.0 μm
Top Al_2O_3	-	20 nm
Top hBN	45 nm	55 nm
Bottom hBN	35 nm	45 nm
Bottom Al_2O_3	20 nm	20 nm

Table 3.2: Geometric sample parameters

3.1.2 Tunnel Junction Fabrication

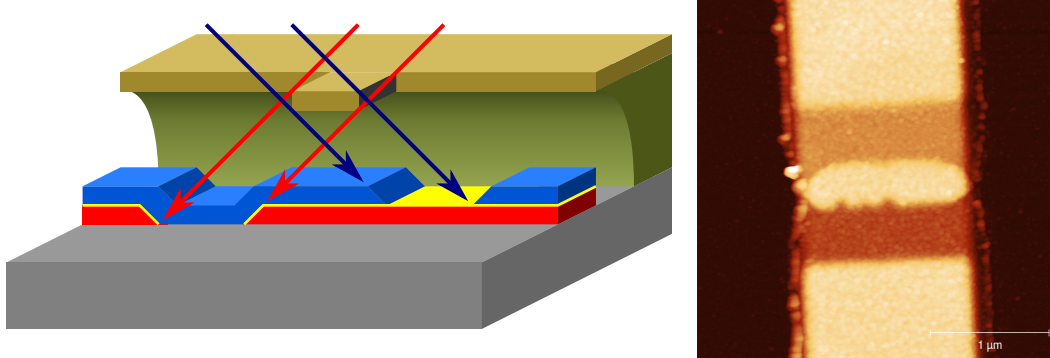


Figure 3.7: (a) Schematic cross section of Niemeyer-Dolan technique with resist double layer of MMA/MAA (green) and PMMA (brown), first metal deposition (red), oxide layer (yellow), and second metal deposition (blue). (b) AFM image of a tunnel junction

The tunnel junction reference samples for the noise measurements were made using the Niemeyer–Dolan technique [Dol77; Nie76; Nie74], i.e. a suspended resist mask and metal evaporation under two different angles as shown in fig. 3.7. First, a resist double-layer of 800 nm of MMA/MAA and 200 nm of PMMA was spin coated onto a sapphire substrate. The pattern, consisting of an array of strips of varying width, each with a gap of 300 nm to 500 nm was written into the resist using an electron beam with a dose of $440 \mu\text{A s cm}^{-2}$. For junctions with smaller area, the region of the gap was additionally exposed with a smaller dose of $130 \mu\text{A s cm}^{-2}$. Due to the higher sensitivity against electron exposure of the bottom resist layer and the proximity effect, this led to a suspended bridge of PMMA in the gap after developing the resist in IPA/MIBK. The metal deposition was performed in an UHV MBE system, where the sample can be tilted with respect to the metal source. After the first deposition of 50 nm Al, the sample was moved from the main evaporation chamber into the load lock. Here, it was exposed to 400 Pa of pure O_2 for 30 min to 60 min to create the oxide barrier, before it was moved back to the main chamber for deposition of the second layer of 80 nm Al. The two evaporations were done with the sample tilted in opposing directions, shifting the pattern by 700 nm (350 nm in either direction), and creating the overlap. The final junction area is defined by the width of the strip, the length of the gap, and the angle of the two evaporations. In the junctions used here, the shift and the parameters for oxidization were kept constant, and only the junction area was tuned to create junctions of varying resistance. The junction resistance is inversely proportional to the overlap area with $R = 1.888 \text{ k}\Omega \mu\text{m}^2 \frac{1}{A}$, as shown in fig. 3.8.

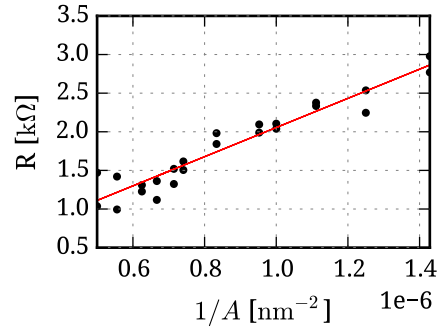


Fig. 3.8: Resistance versus inverse area of tunnel junctions

3.2 Measurement Setup

3.2.1 Cryostat

The measurements were performed in a BlueFors LD250 cryogen-free dilution refrigerator. It reaches a cooling power of $350\ \mu\text{W}$ at 100 mK, and a base temperature below 7 mK for the empty cryostat. With the additional thermal load of the multiple coaxial lines used for RF measurements, the base temperature reaches 10 mK to 20 mK. The cryogen free system makes use of two closed helium circuits and does not require any additional cryogen. Instead of a liquid helium bath, it is cooled down to about 4 K using a two stage pulse tube cooler. Since this temperature is not low enough to condense the $^3\text{He}/^4\text{He}$ mixture, a compressor has to be used during the cooldown. The two stages of the pulsetube at about 50 K and 4 K, the still at about 800 mK, a heat exchanger at about 50 mK, and the mixing chamber at base temperature define the temperatures of the plates where equipment can be installed.

The shot noise measurements were performed simultaneously with standard conductance measurements. This required using two separate cable systems for RF and DC signals. At the time of the measurements, the cryostat was equipped with 24 DC lines at the 4 K level, 48 DC lines at the mixing chamber level, and 8 coaxial RF lines. It has since been upgraded with another set of 24 DC lines, optionally ending at the 4 K or mixing chamber level. When installing cables, care has to be taken to ensure good thermalization at each temperature level, and to reduce thermal conduction in between the different plates. This reduces the heat load on the low temperature plates and thus the base temperature. For the DC cabling, thermalization can easily be achieved by winding the cables around a pin on each plate. For normal conducting metal wires, the thermal decoupling between the plates is hindered by the Wiedemann-Franz law, which states that thermal and electrical conductivity are proportional at low temperature. Thin phosphor bronze wires, whose conductivity shows little temperature and magnetic field dependence are used as a compromise down to the mixing chamber plate. Within the constant temperature domains at 4 K and at base temperature, copper wires are used.

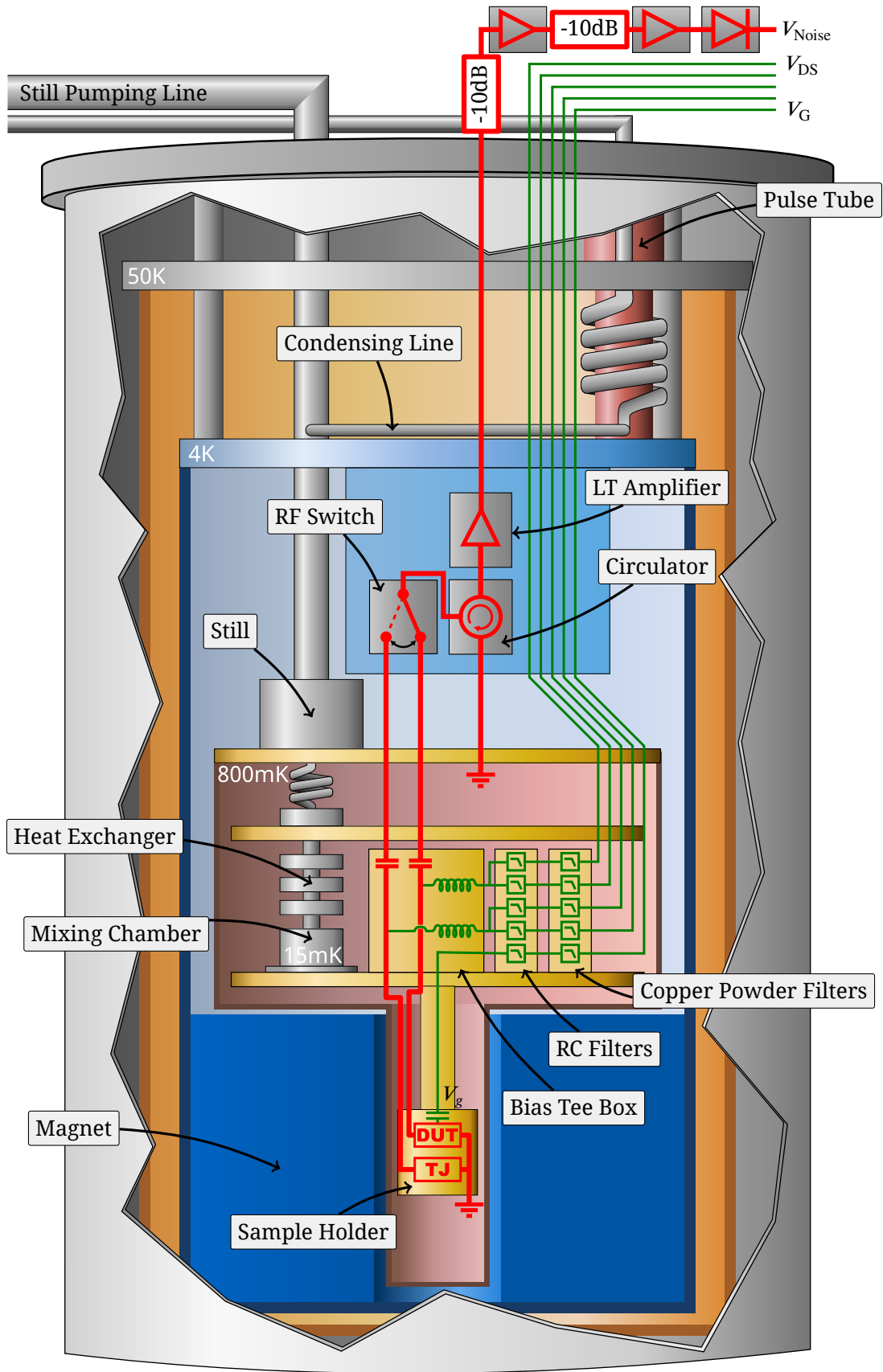
For the coaxial RF cables, the central conductor is both electrically and thermally insulated from the outer conductor by the dielectric. To thermalize it, 1 dB attenuators were added at each plate. As an additional complication, the stainless steel cables designed for low temperature use are very rigid. To make use of their low thermal conductivity while keeping flexibility when connecting and rearranging parts, we combined softer, thermally conductive cables with short segments of stainless steel cable.

3.2.2 DC Measurement

Filtering

Besides lowering the phononic temperature by thermally anchoring the cables, the electronic temperature has to be reduced using low pass filters. In our setup, we use a combination of RC filters and PCB copper powder filters which take over for frequencies above the RC filter's re-entry frequency ($> 5\ \text{GHz}$). The RC Filters consist of three resistors with $R_1 = 330\ \Omega$, $R_2 = 220\ \Omega$, and $R_3 = 100\ \Omega$, with $C = 100\ \text{nF}$ capacitors to ground before and after each resistor, leading to a

Fig. 3.9: Overview of Cryostat. Only 2/8 RF lines and 5/48 DC lines are shown. Not to scale.



transfer function given by [Bor13]

$$H = \frac{1}{1 + i\omega C Z_1 + (i\omega C)^2 Z_2 + (i\omega C)^3 R_1 R_2 R_3}, \quad (3.1)$$

with $Z_1 = 3R_1 + 2R_2 + 3R_3$ and $Z_2 = 2R_1 R_2 + 2R_3 R_1 + R_2 R_3$. The cutoff frequency was designed to be around 1 kHz. While the isolated filter shows the expected behavior, the cutoff frequency is much lower in the actual measurements. Fig. 3.10 shows the calculated real part (solid line) and phase shift (dashed line) of the RC filters. The dots show the phase shift of the AC current through the complete measurement setup (with a tunnel junction sample) versus the frequency of the AC excitation, measured using the lock-in amplifier. Compared to the expected behavior of the isolated filters, the cut-off frequency is reduced due to the additional sample resistance, capacitance, and impedance of the twisted pair wiring (using one wire, while the other one is grounded). The phase shift reaches 90° already at 50 Hz. The DC properties were measured using

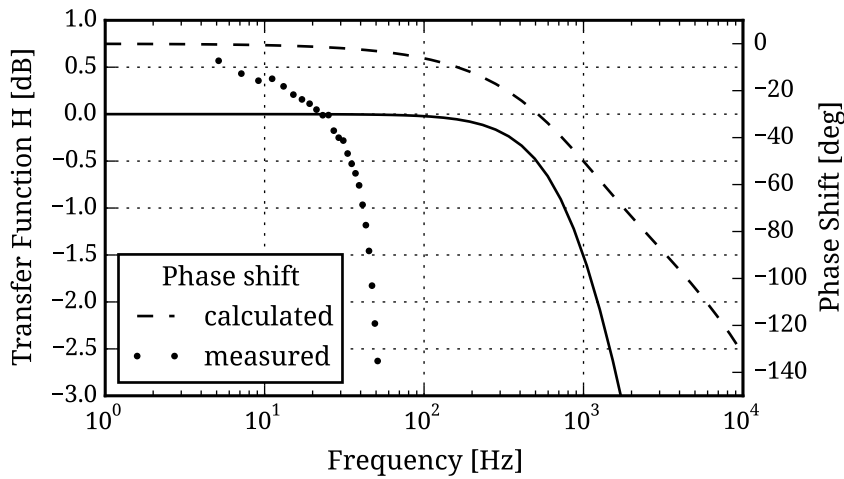


Figure 3.10: Calculated transmission function (solid line) and phase shift (dashed line) of the RC filters and measured phase shift of the full setup (dots) with a tunnel junction sample

a combination of direct measurement with multimeters (Agilent 34410) and lock-in amplifiers.

Therefore, the lock-in measurements were performed at frequencies between 10 Hz to 20 Hz.

3.2.3 Shot Noise Measurement

Practical Noise Measurement Techniques

The purpose of the RF measurement setup is finding the spectral density of the current fluctuations generated by the sample, S_I^S , which can be related to the transport mechanisms as described in section 2.3.2. At typical currents of micro amperes, $S_I^S \approx 2e\langle I \rangle$ is in the order of $1 \times 10^{-24} \text{ A}^2 \text{ Hz}^{-1}$, and the main challenge of measuring the shot noise signal is its tiny amplitude. Thus, the signal has to be heavily amplified. At the same time, the measured noise power, i.e. the integrated spectral power density, can be increased by measuring with a large bandwidth. But trying to improve these two parameters – gain and measurement bandwidth – comes at the cost of technical complications. Using standard low-noise techniques only allows measurements

up to 10 kHz due to the RC cut-off problems [Wu07]. At these low frequencies, $1/f$ noise is still prevalent. On the other hand, commercially available microwave equipment suitable for MHz to GHz frequencies is standardized to a wave impedance of $Z_0 = 50 \Omega$, which does not match mesoscopic samples with a varying resistance of up to several $k\Omega$. The mismatch leads to reflection of a part of the signal, further obstructing the measurement. Techniques that try to solve this issue include the use of resonator circuits [Gla09] and impedance matching networks. But the design of a matching network for a large bandwidth is challenging, especially considering the variable sample impedance and the limited space available on the sample holder [Thü12].

The measured noise power at the end of the amplifier chain typically is accompanied by a noise floor that is orders of magnitude higher than the pure shot noise signal. But this additional noise is not proportional to I_{DS} and can be subtracted, resulting in the *excess noise*

$$S_I^{\text{exc}} = S_I(I) - S_I(0). \quad (3.2)$$

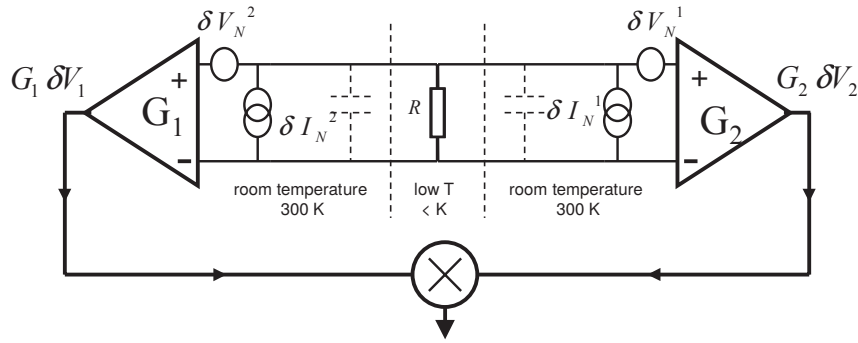


Figure 3.11: Cross correlation measurement scheme. Source: [Gla09] ©2009 EDP Sciences, Springer-Verlag

Nevertheless, because of the uncertainty of the real gain and bandwidth of the measurement setup, which may even change between cool downs, the absolute noise power generated by the sample cannot be easily recovered from the amplified signal.

One method to reduce or eliminate these spurious influences is the measurement of the cross-correlated signal of two separate amplifier chains [Gla09] as shown in figure 3.11. The noise power is retrieved using a correlator and Fast Fourier Transformation. Since the amplifier noise is uncorrelated, the amplifier voltage noise, and in special cases even the current noise, can be completely eliminated from the signal, similar to the DC four point measurement technique. On the other hand, this method effectively requires doubling the entire measurement setup, and due to the computing power needed for the correlation and FFT it limits the bandwidth to 2 GHz [Gla09].

In this work an alternative approach using a RF switch at low temperature to toggle between a reference sample with a known Fano factor and the device under test was used.

RF Measurement Setup

The RF circuit is shown in figure 3.12. The noise generated at the sample is coupled into coaxial cables with wave impedance $Z_0 = 50 \Omega$. Using bias-tees on the mixing chamber plate, the

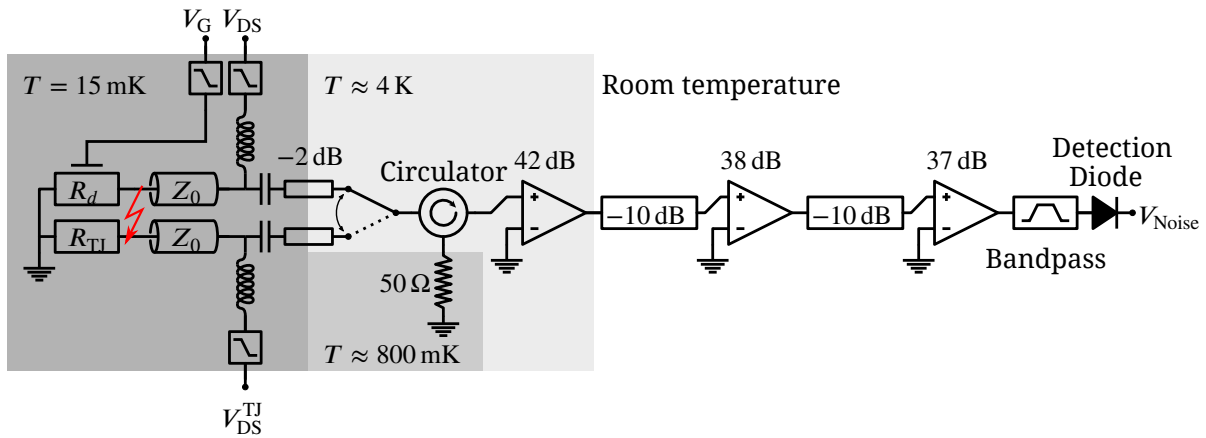


Figure 3.12: Schematic of the shot noise detection method.

RF and DC signal are separated. The RF lines are thermalized with 1 dB attenuators on the intermediate and still plates at 50 mK and 800 mK respectively. At the 4 K level, the RF switch connects either line to the amplifier chain. In between of the switch and the low temperature first stage amplifier a circulator was installed, a passive three terminal component that transmits the signal in clockwise direction from one port to the next, but suppresses the reverse direction. Thus, the back-action noise coming from the amplifier is directed to a 50 Ω shunt resistor installed on the still plate at 800 mK, where it is absorbed.

The RF setup was characterized at room temperature using a vector network analyzer (VNA) with a bandwidth of 0 GHz to 6 GHz.¹ Fig 3.13 (left) shows the transmission S_{21} from the sample to the top of the cryostat for either setting of the RF switch, labeled “Green” and “Red” and indicated by a corresponding LED on the controller box. This includes the 42 dB gain of the low temperature amplifier. The average transmission S_{21} from 4 GHz to 6 GHz is 31 dB. S_{21} and S_{12} of the first part of the setup, from the sample holder to the input of the low temperature amplifier, are shown in fig 3.14. The effect of the circulator can be seen by comparing S_{21} and S_{12} , where the transmission from the amplifier to the sample, S_{12} , is suppressed by ≈ -13 dB compared to the reversed direction. The circulator² is specified for operation at 0.1 K to 77 K, with a minimum isolation of 18 dB and a maximum loss of 0.4 dB, so the S-parameters of this section are expected to change for the operation at low temperature. The mean loss of this first stage of the measurement setup in the range of 4 GHz to 6 GHz is ≈ 2.8 dB, not including loss on the sample holder itself. 2 dB can be attributed to the attenuators used for thermalization. Fig 3.15 shows the transmission from the output of the low temperature amplifier to the top of the cryostat, where the average loss within the range of 4 GHz to 6 GHz is ≈ 4.9 dB. The gain of the room temperature amplifiers was measured as 37.6 dB for model 018B and 36 dB for model 942B. The expected gain of the complete measurement setup can then be estimated as

¹ The VNA was not calibrated for the long measurement cables that were used, but the attenuation measured separately and has been subtracted from the data, along with additional 20 dB attenuation that was installed during measurements with amplifiers.

² Pamtech CTH0408KC

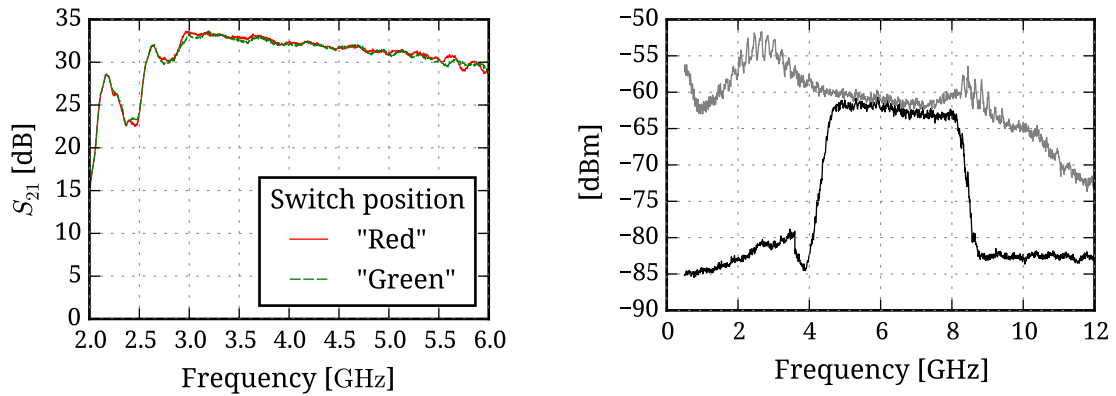


Figure 3.13: **Left:** S_{21} from the sample holder to the top of the cryostat, including the 42 dB LT LNA, for either position of the RF switch, measured at room temperature. **Right:** Spectral analysis of tunnel junction noise with and without bandpass filter at 3 MHz resolution bandwidth, measured at low temperature

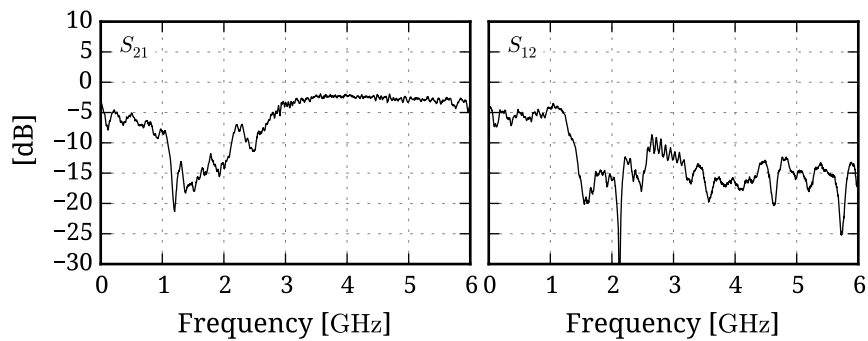


Figure 3.14: S_{21} and S_{12} from the sample holder to the input of the low temperature amplifier, showing the effect of the circulator. Measured at room temperature (outside of the operating temperature range of the circulator 0.1 K to 77 K)

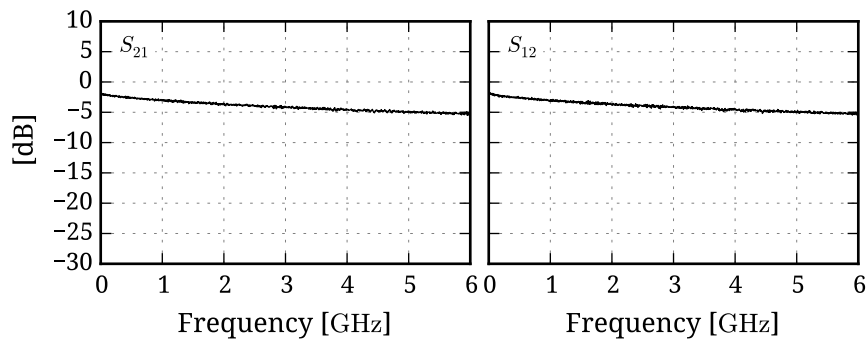


Figure 3.15: S_{21} and S_{12} from the output of the low temperature amplifier to the top of the cryostat

$g = (31 - 10 + 37.6 - 10 + 36)\text{dB} = 84.6\text{ dB}$ using all three amplifiers, and $g = 58.6\text{ dB}$ using only one room temperature amplifier. After amplification, the RF signal passes a bandpass filter. Typically, the measurements were performed at the largest possible bandwidth of 4.6 GHz to 7.2 GHz. At this bandwidth, the expected product of gain and bandwidth GBW is $7.50 \times 10^{17}\text{ Hz}$ and $1.88 \times 10^{15}\text{ Hz}$, respectively. Note however, that the measurements were performed at room temperatures, and the properties of the amplifier, the low temperature coaxial cables, and the circulator can change drastically when cooled down. The amplified signal is finally fed into a Schottky noise detector diode¹, which integrates the bandwidth selected by the bandpass filter and outputs a (negative) DC voltage with a sensitivity of $\alpha_D = 0.5\text{ mV } \mu\text{W}^{-1}$, which can be measured as a DC signal using a multimeter (V_{Noise}), or as a differential signal dV_{Noise} measured using a lock-in.

Impedance Mismatch

It is common to express the power of a noise source with constant (white) current spectral density S_I in terms of an equivalent temperature of thermal noise given by $T := \frac{R}{4k_B} S_I$. Using eq. (2.50), the sample can then be represented by a thermal noise source with

$$\begin{aligned} T_s &= \frac{R_d}{4k_B} S_I \\ &= \frac{R_d}{4k_B} \left(4k_B T_e \frac{1}{R_d} \left[(1 - \mathcal{F}) + \mathcal{F} \frac{eV}{2k_B T} \coth \left(\frac{eV}{2k_B T_e} \right) \right] \right) \\ &= T_e (1 - \mathcal{F}) + \frac{R_d}{4k_B} \mathcal{F} 2eI \coth \left(\frac{eV}{2k_B T_e} \right) \end{aligned} \quad (3.3)$$

where $R_d = \frac{dV}{dI}$ is the sample's differential resistance and T_e is the electronic temperature.

Special attention has to be paid to the coupling of this noise signal to the measurement setup. The problem of **impedance mismatch** can be understood from the simplified model shown in fig. 3.16. The sample is modeled as a noiseless resistor in parallel to an ideal current noise source δI_S , and the detector (i.e. the first amplifier) is represented as a resistor $Z_0 = 50\ \Omega$. The mean power transferred to the detector is given by $P_m = \langle \delta I_m^2 \rangle Z_0$, and with $\delta U = \left(\frac{1}{R_d} + \frac{1}{Z_0} \right)^{-1} \delta I_S$ we get

$$\begin{aligned} P_m &= \left\langle \left(\frac{\delta U}{Z_0} \right)^2 \right\rangle Z_0 = \left(\frac{R_d}{R_d + Z_0} \right)^2 \langle \delta I_S^2 \rangle Z_0 \\ &= \frac{4R_d Z_0}{(R_d + Z_0)^2} \frac{1}{4} \langle \delta I_S^2 \rangle R_d \end{aligned} \quad (3.4)$$

Maximum power transfer is achieved for $R_d = Z_0$ (more generally $Z_d = Z_0^*$), where $P_m = \frac{1}{4} P_S$. For mismatched samples $R_d \neq Z_0$, only a fraction of the available noise is coupled into the detector.

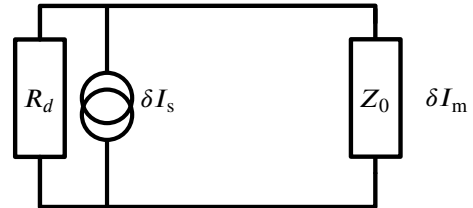


Fig. 3.16: Simple model of the coupling to the measurement setup

1 Krytar 201B

The same effect can be described in terms of transmission and reflection coefficients for the electromagnetic waves traveling between the sample and the detector, taking into account the transmission line in between. While the amplifier is matched to the wave impedance of the coaxial cable, the impedance mismatch on the sample side leads to an amplitude reflection coefficient $\Gamma(R_d) := \frac{R_d - Z_0}{R_d + Z_0}$ [Poz12]. The coefficient for the transmitted power is given by

$$1 - |\Gamma|^2 = 1 - \left(\frac{R_d - Z_0}{R_d + Z_0} \right)^2 = \frac{4R_d Z_0}{(R_d + Z_0)^2}, \quad (3.5)$$

as derived from the simple model in eq. (3.4). For a sample with conductance in the order of the conductance quantum G_0 , $(1 - |\Gamma(\frac{h}{2e})|^2) \approx 1.5\%$, while low resistance graphene samples can reach $(1 - |\Gamma(200\ \Omega)|^2) \approx 64\%$. For shot noise, this reduction of transmission gets partly compensated by increased noise power, since the spectral power density $S_I R_d$ scales with R_d . Thus, despite the mismatch, more power is delivered to the amplifier for increased sample impedance at a fixed current. The noise power originating from the sample that is coupled into the detector is given by

$$\begin{aligned} T_{m,s} &= (1 - |\Gamma|^2) T_s \\ &= \frac{4R_d Z_0}{(R_d + Z_0)^2} \left(T_e (1 - \mathcal{F}) + \frac{R_d}{4k_B} \mathcal{F} 2eI \coth \left(\frac{eV}{2k_B T} \right) \right) \\ &= (1 - |\Gamma|^2) T_e (1 - \mathcal{F}) + \frac{1}{k_B} \left(\frac{R_d}{R_d + Z_0} \right)^2 \mathcal{F} 2eI \coth \left(\frac{eV}{2k_B T} \right) Z_0 \end{aligned} \quad (3.6)$$

A more realistic model of the setup, including spurious noise sources, is shown in figure 3.17. To understand the final measurable signal (V_{Noise}) at the output of the amplifier chain, the role of this additional noise has to be understood. Assuming an ideal circulator and lossless (and therefore noiseless) transmission lines in between the components, three main sources of noise remain: the sample itself (T_S), the shunt resistor (T_N), and the first amplifier (T_0). The sample noise T_S is coupled to the amplifier through the transmission coefficient $(1 - |\Gamma|^2)$ as describes above. But besides reducing the transmitted signal, the mismatch also causes back-reflection of noise at the sample which is coming from the direction of the detection setup, mostly the thermal noise generated at the shunt resistor T_N , with a coefficient $|\Gamma|^2$. Lastly, the amplifier noise T_0 is coupled to the matched shunt resistor, adding a constant offset T_0 . The total noise sensed by the detector then reads

$$T_m = (1 - |\Gamma|^2) T_s + |\Gamma|^2 T_N + T_0. \quad (3.7)$$

While the incident noise power T_N is constant, a variation of the sample resistance changes the reflection coefficient $|\Gamma(R_d)|^2$ and can distort the measured signal. The third term, T_0 , also includes additional amplifier noise, i.e. noise that is added after the first amplification stage. It accounts for the biggest part of the absolute measured signal, yet being constant (except for some drift on longer timescale) it can easily be subtracted.

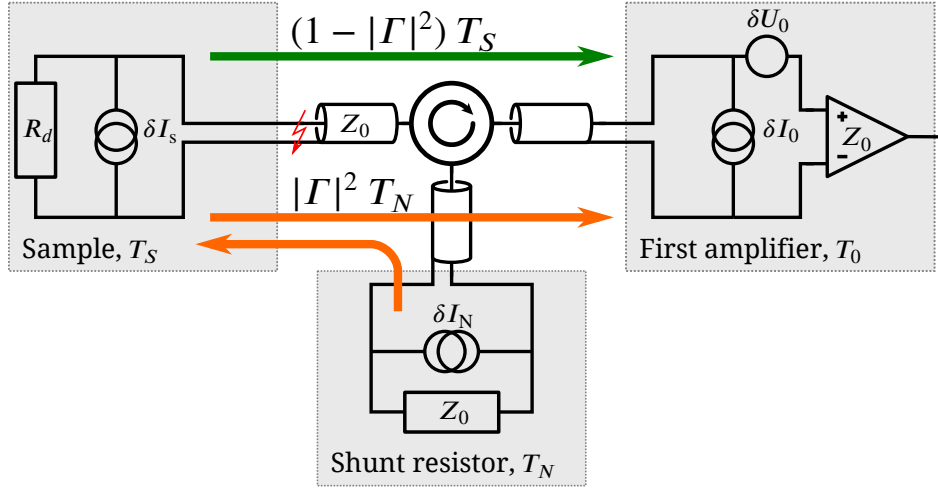


Figure 3.17: Noise sources in the measurement setup.

The output voltage of the noise detector diode then is given by

$$\begin{aligned} V_{\text{Noise}} &= \alpha_D \times \text{GBW} \times k_B T_m \\ &= \alpha_D \times \text{GBW} \left((1 - |\Gamma|^2) \frac{1}{4} S_{I,s} R_d + |\Gamma|^2 k_B T_N + k_B T_0 \right) \end{aligned} \quad (3.8)$$

where α_D is the sensitivity of the diode ($\alpha_D = 0.5 \text{ mV } \mu\text{W}^{-1}$) and GBW is the product of gain g and bandwidth BW. The spectral density of current fluctuations was given by (2.50) as

$$S_{I,s} = 4k_B T \frac{1}{R} \left[(1 - \mathcal{F}) + \mathcal{F} \frac{eV}{2k_B T_e} \coth \left(\frac{eV}{2k_B T_e} \right) \right] \quad (2.50)$$

$$= \frac{4k_B T_e}{R_d} + \mathcal{F} \frac{4k_B T_e}{R_d} (x \coth(x) - 1) \quad \text{with } x := \frac{eV}{2k_B T_e} \quad (3.9)$$

$$=: S_{I,s}^{\text{Th}} + S_{I,s}^{\text{Shot}}. \quad (3.10)$$

The aim of the next sections is recovering $S_{I,s}$ and \mathcal{F} , theoretically given by (2.50), from the experimentally measured signal V_{Noise} .

Samples with Linear IV Characteristic

For linear samples with $R_d(I) = R_d(0) = \text{const}$ (i.e. normal conducting graphene or a tunnel junction), Γ is constant, the only bias dependence is caused by $S_{I,s}$, and all of the additional noise can be subtracted by subtracting the noise at zero bias (in graphene, R_d may still depend

on the gate voltage, which stays constant during bias sweeps).

$$\begin{aligned}
V_{\text{Noise}}(I) - V_{\text{Noise}}(0) &= \alpha_D \text{ GBW} (1 - |\Gamma|^2) \frac{1}{4} R_d (S_{I,s}(I) - S_{I,s}(0)) \\
&= \alpha_D \text{ GBW} (1 - |\Gamma|^2) \frac{1}{4} R_d \mathcal{F} \left(2eI \coth \left(\frac{eV}{2k_B T_e} \right) - \frac{4k_B T_e}{R_d} \right) \\
&= \alpha_D \text{ GBW} (1 - |\Gamma|^2) \frac{1}{4} R_d \underbrace{2eI \mathcal{F} \left(\coth \left(\frac{eV}{2k_B T_e} \right) - \frac{4k_B T_e}{2eV} \right)}_{=F} \\
&= \alpha_D \text{ GBW} (1 - |\Gamma|^2) \frac{1}{4} R_d S_{I,s}^{\text{exc}}, \tag{3.11}
\end{aligned}$$

with excess noise

$$S_{I,s}^{\text{exc}} = (S_{I,s}(I) - S_{I,s}(0)). \tag{3.12}$$

A bias dependent “full” Fano factor F that includes the effects of thermal noise at low bias can be defined as [Wu07]

$$F(I) := \frac{1}{2eI} S_{I,s}^{\text{exc}}. \quad \text{Full Fano factor} \tag{3.13}$$

For $eV \gg k_B T$, it is equal to \mathcal{F} . Since R_d , Γ and I are known from simultaneous DC conductance measurement, only the proportionality constant given by the diode sensitivity $\alpha_D = 0.5 \text{ mV } \mu\text{W}^{-1}$ and the gain bandwidth product GBW are needed to recover F . This calibration constant is the main parameter that has to be measured on the reference tunnel junction sample with known Fano factor.

Using the Lock-In measurement, the differential noise output voltage can be measured directly. With $dR_d = 0$, the measured signal is given by

$$dV_{\text{Noise}} = \alpha_D \times \text{GBW} (1 - |\Gamma|^2) \frac{1}{4} R_d dS_{I,s}. \tag{3.14}$$

By defining the “differential” Fano factor F_d as [Wu07]

$$F_d := \frac{1}{2e} \frac{dS_{I,s}}{dI} \Rightarrow dS_{I,s} = 2eF_d dI, \tag{3.15}$$

we get

$$\frac{dV_{\text{Noise}}}{dI} = \alpha_D \times \text{GBW} (1 - |\Gamma|^2) \frac{1}{4} R_d 2eF_d, \tag{3.16}$$

where again $F_d = F = \mathcal{F}$ for $eV \gg k_B T$. The full Fano factor can be found by integration of the differential Fano factor as

$$F = \frac{1}{I} \int_0^I F_d dI = \frac{1}{2eI} (S_I(I) - S_I(0)), \tag{3.17}$$

and the spectral current density is given by

$$S_{I,s}^{\text{AC}} = \left(\alpha_D \text{GBW} (1 - |\Gamma|^2) \frac{1}{4} R_d \right)^{-1} \int_0^I \frac{dV_{\text{Noise}}}{dI} dI + S_{I,s}(0). \quad (3.18)$$

The integration constant $S_{I,s}(0)$ has to be taken from the DC V_{Noise} data.

Samples with Non-Linear IV Characteristic

For the measurements at high magnetic fields in section 4.3.2 and with proximity induced superconductivity in section 4.4.3, R_d is bias dependent and can no longer be considered constant. This leads to changes of the measured signal due to the changing transmission and reflection coefficients, and we have to take another look at the equation for the measured voltage,

$$V_{\text{Noise}} = \alpha_D \times \text{GBW} \left((1 - |\Gamma|^2) \frac{1}{4} S_{I,s} R_d + |\Gamma|^2 k_B T_N + k_B T_0 \right). \quad (3.8)$$

The nonlinearity in $R_d(I)$ influences the signal in a complicated way, depending on the impedance mismatch Γ , the magnitudes of sample noise T_S and thermal noise T_N , and the strength of the nonlinearity itself. Additionally to the effect of changing Γ , the spectral power density of thermal noise generated by the sample $S_{I,s}^{\text{Th}}$ also depends on R_d . Finding a completely accurate model is a difficult task, since the exact values of these parameters may depend on details that have not been considered so far and may even be hard to determine, for example the effect of additional loss (and noise) in the bias tees, switch and transmission lines, and the actual behavior of the circulator in mismatched condition. Anyhow, a rough estimation shall be made.

The measured voltage (3.8) can be written as a function of sample noise and sample impedance, with a differential

$$\begin{aligned} dV_{\text{Noise}}(S_{I,s}, R_d) &= \alpha_D \text{GBW} \left[\underbrace{(1 - |\Gamma|^2) R_d \frac{1}{4} dS_{I,s}}_{\textcircled{1}} + \underbrace{d((1 - |\Gamma|^2) R_d) \frac{1}{4} S_{I,s}}_{\textcircled{2}} + \underbrace{d(|\Gamma|^2) k_B T_N}_{\textcircled{3}} \right] \\ &= \alpha_D \text{GBW} \left[(1 - |\Gamma|^2) R_d \frac{1}{4} dS_{I,s} + \frac{2Z_0}{(R_d + Z_0)^3} (R_d Z_0 S_{I,s} + 2(R_d - Z_0) k_B T_N) dR_d \right] \end{aligned} \quad (3.19)$$

Term $\textcircled{1}$ is equal to (3.14) and describes change due to actual variation of the sample noise $S_{I,s}$. Term $\textcircled{2}$ describes the variation of transmission from the sample, term $\textcircled{3}$ is the variation of the reflection of noise incident on the sample. We can now recover $S_{I,s}$ by integration of dV_{Noise} . To calculate the compensation term, $S_{I,s}$ in term $\textcircled{2}$ can be taken from the DC measurement and T_N can be taken as the temperature of the shunt resistor connected to the circulator.

Another small distortion caused by nonlinear R_d could come from the thermal noise baseline

of the sample noise, $S_{I,s}^{\text{Th}}$. From (3.10) we get

$$S_{I,s} = S_{I,s}^{\text{Shot}} + S_{I,s}^{\text{Th}} = S_{I,s}^{\text{Shot}} + \frac{4kBT_e}{R_d} \quad (3.20)$$

$$dS_{I,s} = dS_{I,s}^{\text{Shot}} - \frac{4kBT_e}{R_d^2} dR_d, \quad (3.21)$$

and for the differentially measured noise voltage

$$dV_{\text{Noise}}(S_{I,s}, R_d) = \alpha_D \text{GBW} \left[(1 - |\Gamma|^2) R_d \frac{1}{4} \left(dS_{I,s}^{\text{Shot}} - \frac{4kBT_e}{R_d^2} dR_d \right) + \frac{2Z_0}{(R_d + Z_0)^3} (R_d Z_0 S_{I,s} + 2(R_d - Z_0)k_B T_N) dR_d \right]. \quad (3.22)$$

We finally reach the formula to recover the shot noise of the sample, compensated for the distortion caused by nonlinear R_d :

$$dS_{I,s}^{\text{Shot}} = \frac{4}{(1 - |\Gamma|^2)R_d} \left\{ \frac{1}{\alpha_D \text{GBW}} dV_{\text{Noise}} - \left[\underbrace{\frac{2R_d Z_0^2}{(R_d + Z_0)^3} S_{I,s}^{\text{DC}}}_{\textcircled{1}} + \underbrace{\frac{4Z_0(R_d - Z_0)k_B T_N}{(R_d + Z_0)^3}}_{\textcircled{2}} - \underbrace{(1 - |\Gamma|^2) \frac{k_B T_e}{R_d}}_{\textcircled{3}} \right] dR_d \right\}, \quad (3.23)$$

where the corrections consists of a term $\textcircled{1}$ proportional to the noise itself, term $\textcircled{2}$ corresponding to noise from the shunt resistor that is reflected at the sample, and term $\textcircled{3}$ corresponding to the transmission of thermal noise from the sample. Ideally, term 2 and 3 should be as small as possible, or cancel each other. From (3.9), a compensated Fano factor can be defined as

$$F_C := \frac{1}{2eI} S_{I,s}^{\text{Shot}} \quad (3.24)$$

3.2.4 Tunnel Junction Reference Measurements

To find the gain bandwidth product (GBW) of the measurement setup, the shot noise of tunnel junction reference samples was measured. In the normal state, the Fano factor of a tunnel junction is $\mathcal{F} = 1$. With constant R_d , the noise voltage is given by (3.8), and using (3.9) we get

$$V_{\text{Noise}} = \alpha_D \text{GBW} \left\{ (1 - |\Gamma|^2) R_d \left[\frac{4k_B T}{R_d} + \mathcal{F} \frac{4k_B T}{R_d} \left[\frac{2e|V-V_0|}{4k_B T} \coth \left(\frac{2e|V-V_0|}{4k_B T} \right) - 1 \right] \right] + k_B T_{\text{Noise}} \right\}. \quad (3.25)$$

Since the tunnel junction has a constant resistance, the noise components of the shunt resistor T_N and the amplifier T_0 can't be distinguished and have been combined to a total noise background T_{Noise} .

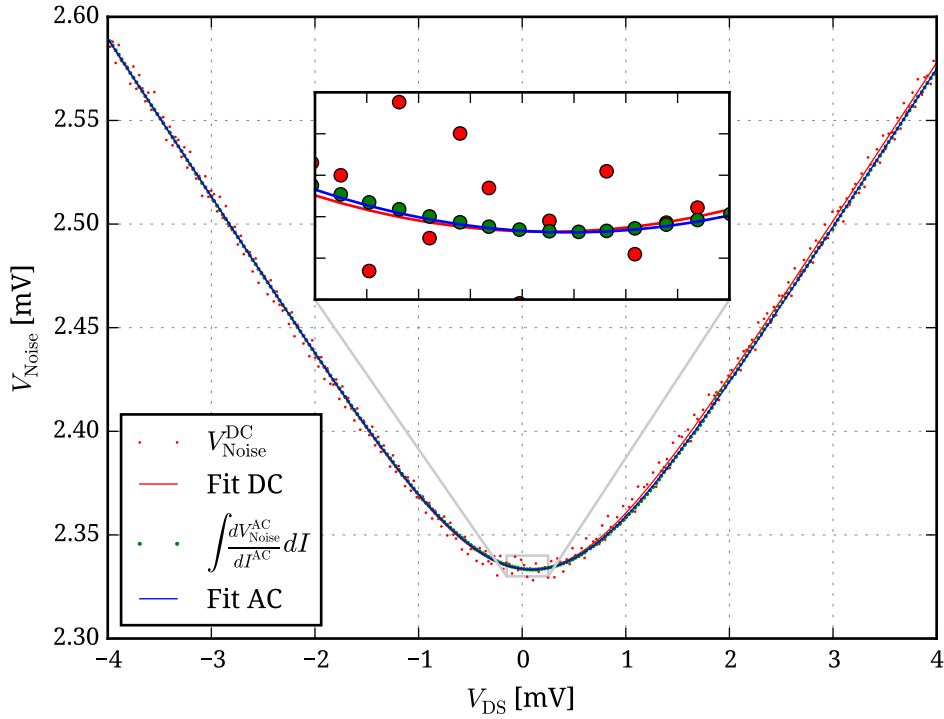


Figure 3.18: Calibration measurement of a tunnel junction at 4 K, showing the direct measurement of the noise detection diode (red dots), the differentially measured and integrated values (green dots) and fitted curves according to equation (3.25)

Figure 3.18 shows example data of a tunnel junction that was measured together with sample A in normal state at 4 K (corresponding to the first line in table 3.3). The red dots show the voltage output of the noise detection diode, measured using the multimeter ($V_{\text{Noise}}^{\text{DC}}$). The differential of this output voltage $dV_{\text{Noise}}^{\text{AC}}$ was measured at the same time using a lock-in amplifier and a small AC excitation of $dV = 37 \mu\text{V}$. The green dots show $dV_{\text{Noise}}^{\text{AC}}$ divided by the simultaneously measured differential current change dI^{AC} and integrated¹ over the current step between two

¹ Cumulative trapezoidal numerical integration

data points $\int \frac{dV_{\text{Noise}}^{\text{AC}}}{dI^{\text{AC}}} dI$, where the integration constant was set such that the minimum of the integrated data aligns with the minimum of the fit to the DC data. As shown in the inset of fig. 3.18, the lock-in measurement drastically improves the measurement accuracy. The red and blue lines show the fit of the DC and lock-in measured data to 3.25. Each of the fit parameters is responsible for a characteristic feature: V_0 is equivalent to adjusting the zero offset on the voltage amplifier for V_{DS} , it shifts the entire curve along the abscissa. GBW determines the slope at higher bias, and GBW and T_{Noise} determine the overall V_{Noise} floor. The electronic temperature T_e defines the shape at low bias and is independent of the other variables, so it can be extracted even if there is uncertainty about GBW and \mathcal{F} .

	\mathcal{F}	T_{MC} [K]	T_{Still} [K]	T_4 [K]	BW [GHz]	g [dB]	GBW [Hz]	$V_{\text{Noise}}^{\text{min}}$ [mV]	T_{Noise} [K]	T_e [K]
#17										
TJ-C4	1	4,182	4,325	3,8	2,6	79,86	2,49E+17	2,3	1,33	4,154
#19										
TJ-C4	1	0,015	0,835	3,008	2,6	75,75	8,88E+16	1,2	2,03	0,246
TJ-C4	1	0,014	0,834	3,008	0,9	94,97	2,58E+18	28,8	1,44	0,254
TJ-C4	1	0,014	0,83	3,027	2,6	91,37	3,16E+18	56,4	2,58	0,261
TJ-C4	1	0,015	0,831	3,024	2,6	91,13	3,22E+18	58,1	2,61	0,333
#22										
TJ-B7b	1	4,172	4,366	3,86	2,6	78,49	1,85E+17	51,7	40,28	9,054
TJ-B7b	1	0,013	0,832	3,119	2,6	79,57	2,35E+17	34,3	21,19	0,301
TJ-B7b	1	0,931	1,291	3,151	2,6	78,95	2,21E+17	37,0	24,20	2,0167
TJ-B7b	1	0,02	0,833	3,155	2,6	79,96	2,65E+17	34,3	18,73	0,296

Table 3.3: Fit parameters for tunnel junction reference measurements, assuming $\mathcal{F} = 1$. The blocks correspond to cool downs #17,#19,#22 (see text)

The data presented in this thesis was mostly recorded during two cool downs¹. During the first cool down, the setup was modified by adding a second room temperature amplifier (increasing the expected gain at room temperature from ≈ 59 dB to ≈ 85 dB), and before the second cool down the shunt resistor at the circulator was moved from the "4 K stage" (the actual temperature is closer to 3 K) to the still stage at 800 mK. Table 3.3 shows fit results of calibration measurements, naïvely assuming $\mathcal{F} = 1$.

The number that is given for the gain in table 3.3 was calculated by dividing the GBW by the given bandwidth. This does not take into account the slight "pink" filter, as higher frequencies feel more attenuation in the coaxial cables due to the skin effect, which can already be seen in the measurement up to 6 GHz in figure 3.13. This reduces transmitted power at higher frequencies, so the gain will be underestimated by this calculation. Furthermore, during the measurement of the attenuation the cryostat was done at room temperature, so the actual gain at low temperature can be higher than the estimated value, and in conclusion, the values of GBW for the calibration using TJ-C4 are reasonable.

¹ cooldown serial numbers 19 and 22

The noise temperature of the amplifier¹ is specified to be ≈ 2 K at $T = 12$ K, which would roughly translate into ≈ 0.5 K at $T_{\text{LNA}} = 3$ K during the measurement. Additionally, the shunt resistor at the circulator, whose noise is almost entirely reflected at the sample due to $|\Gamma|^2 \approx 1$, was at 3 K, but its contribution is reduced by cold attenuators.

On the other hand, the second tunnel junction "B7b" which was used during the measurement of the pn-junction sample, shows very different behavior. Besides moving the shunt resistor to 800 mK, the setup was not changed, so the fit parameters seem unrealistic. While the calculated GBW is smaller than expected, T_{Noise} is much higher. The noise temperature is calculated from the measured noise voltage as $T_{\text{Noise}} = \frac{V_{\text{Noise}}^{\text{min}}}{\alpha_D \text{GBW}}$, so both discrepancies can be explained by a reduced noise source power. To understand this behavior, IV curves were recorded at low temperature,

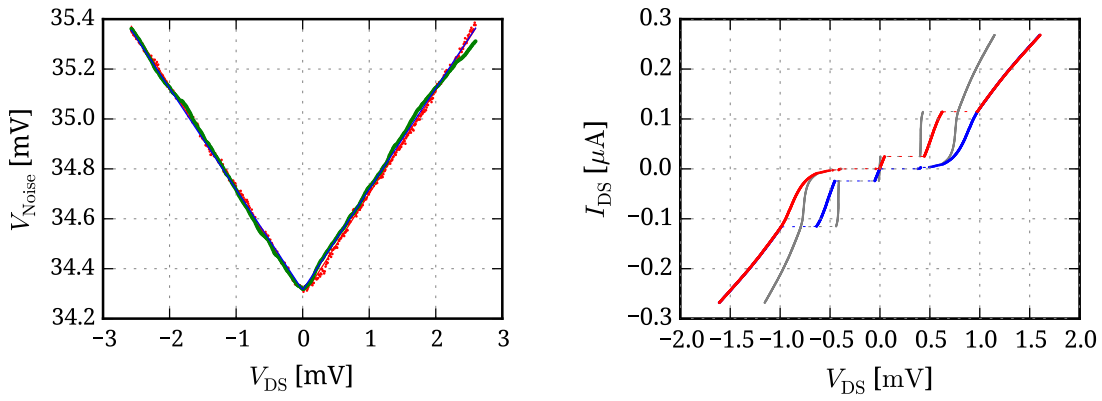


Figure 3.19: Left: Calibration measurement of tunnel junction TJ-B7b at 15 mK, with a magnetic field of 30 mT. **Right:** IV characteristic of the tunnel junction at 15 mK in a constant current measurement without magnetic field. Red and blue curves correspond to up and down sweeps. In the gray curve, a constant series resistance of 1.7 k Ω was subtracted.

where it behaves as a Josephson junction. Figure 3.19 shows the IV characteristic, measured at 15 mK in constant current configuration. The junction has a very strong hysteresis where the zero voltage state is only entered at zero bias, so it is highly underdamped due to the large junction area 2.2. But it shows several features which indicate that the assumption of $\mathcal{F} = 1$ cannot be correct. In the superconducting state, a residual series resistance of ≈ 1.7 k Ω remains, and it shows two different critical currents. Furthermore, the differential resistance should be reduced at the peaks in the density of states at $2\Delta_{\text{Al}} = 360$ μeV , while twice of this value is found in the IV. This behavior could be explained by assuming two or more junctions in series, so that the bias voltage is divided. The shot noise of two identical junctions in series would be half, additional series resistance further reduces \mathcal{F} , and the actual Fano factor is unknown.

In conclusion, the calibration data unfortunately is not reliable, at least for cool down #22, i.e. the data of sample B. At the time of the measurement, exchanging the reference sample was no option, since this would have put the graphene sample at risk. In the following, noise data will be presented using GBW from the earlier calibration, but the resulting values for the Fano factor and the current spectral density can only be seen as a rough estimation.

¹ Model: LNF-LNC4_8A s/n 083

CHAPTER 4

Results and Discussion

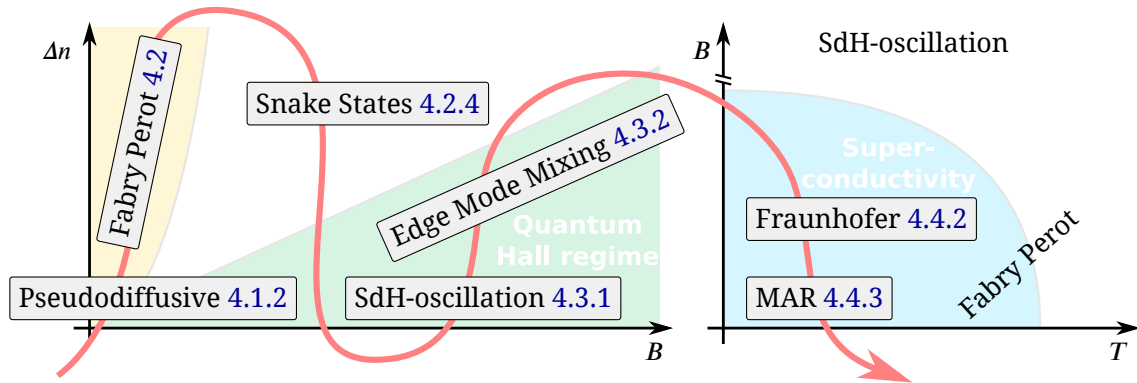


Figure 4.1: Overview of the data presented in this chapter, schematically arranged by measurement conditions. Left: with respect to charge carrier density imbalance Δn and field B , right: with respect to B and temperature T .

Despite the simple geometry of samples presented in the last chapter, a rich variety of physics can be accessed by varying the measurement conditions. The adjustable parameters are

V_{DS}	source drain bias,
V_{BG}	back gate voltage,
V_{TG}	top gate voltage,
$T = T_{MC}$	mixing chamber temperature,
$B = B_{\perp}$	perpendicular magnetic field.

The back gate potential adjusts the global Fermi level E_F , along with the Fermi wavelength λ_F , charge carrier density n and other associated values. The top gate potential V_{TG} only acts on half of the sample where E_F can be controlled independently, allowing to introduce a p-n junction by increasing $\Delta n = n_{BG} - n_{TG}$. By lowering the temperature T , the Ti/Al contact leads can turn superconducting and effects of proximity induced superconductivity in graphene can be investigated.

Finally, the magnetic field B allows bending the semi classical trajectories of the charge carriers, and by increasing it further, entering the Quantum Hall regime.

4.1 Ballistic Graphene

4.1.1 Basic Characterization

An instructive and typical initial measurement on any graphene device consists of sweeping the gate voltage V_G while measuring the resistance across the graphene channel. The electrostatic field tunes the charge carrier density $n = \frac{\epsilon_0 \epsilon_r}{|e|d} V_G = \alpha_G V_G$ and the Fermi level $E_F = \hbar v_F \sqrt{n\pi}$ in the graphene as described in section 2.1.2.

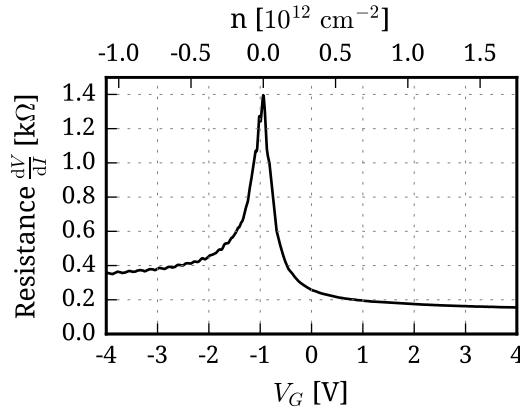


Figure 4.2: Gate sweep of sample A at $T_{MC} = 18$ mK, $B = 20$ mT to suppress superconductivity.

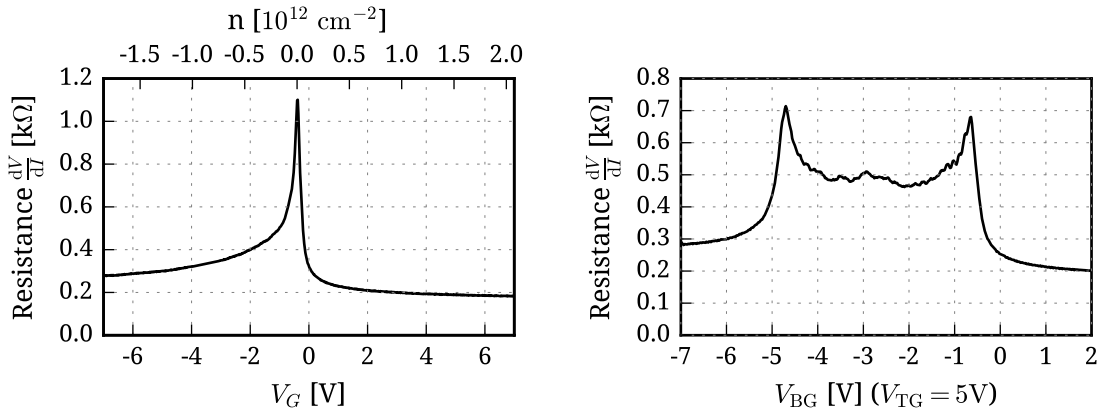


Figure 4.3: Gate sweeps of sample B at $V_{TG} = 0$ and $V_{TG} = 5$ V, $T_{MC} = 4.2$ K

The resulting plots of gate voltage and resistance of sample A and sample B are shown in figure 4.2 and 4.3. The upper x-axis shows the charge carrier density, calculated using α_G extracted from Shubnikov-de Haas measurements as will be described in detail in section 4.3.1. Evidently, the resistance is asymmetric with respect to electron ($V_G > 0$) and hole conduction ($V_G < 0$). This can be explained by the influence of the TI/Al contact leads. Due to a difference of the work

functions of the metal and graphene, the contact leads cause local n-doping. At negative gate voltages, the graphene channel is p-doped and pn-junctions emerge at the contacts, increasing the sample resistance. This charge transfer also affects the overall doping, as can be seen from the shift of the charge neutrality point (“**Dirac point**”) towards negative gate voltages. In both samples, a small negative gate voltage is required to compensate the p-doping. The charge neutrality point of sample A is at $V_D^A = -1.05$ V, corresponding to a residual charge carrier density of $n_0^A = 3.73 \times 10^{11} \text{ cm}^{-2}$ at $V_G = 0$. For sample B we find $V_D^B = -0.4$ V, corresponding to $n_0^B = 1.13 \times 10^{11} \text{ cm}^{-2}$.

The **contact resistance** R_C can be estimated from the lowest resistance at high positive charge carrier densities. Sample A was measured up to $n = 1 \times 10^{12} \text{ cm}^{-2}$, where the resistance tends to $R = 150 \Omega$. To calculate the extrinsic contact resistance, we can subtract the quantum resistance $R_Q = \frac{h}{4e^2} \frac{1}{M}$, with $M = \left\lceil \frac{2W}{\lambda_F(n)} \right\rceil$ the number of conduction modes, to get $R_C^A = \frac{1}{2}(R_{\min} - R_Q)W = \frac{1}{2}(150 - 38) * 3 \Omega \mu\text{m} \approx 168 \Omega \mu\text{m}$ for sample A and $R_C^B = \frac{1}{2}(175 - 16) * 5 \Omega \mu\text{m} \approx 397 \Omega \mu\text{m}$ for sample B.

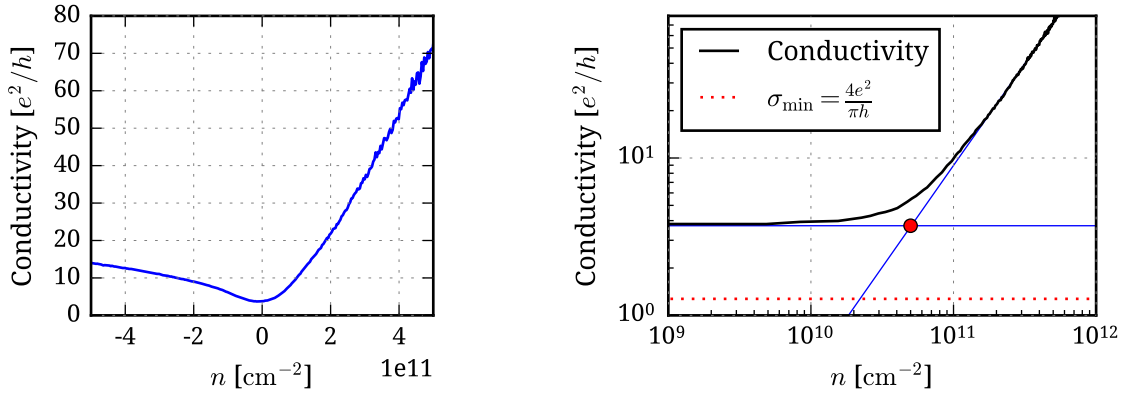


Figure 4.4: **Left:** Conductivity σ in sample A. **Right:** Saturation density in log-log plot of conductivity, the red dashed line shows the theoretical minimal conductivity at $\frac{4e^2}{\pi h}$

An often mentioned figure of merit for the “quality” of graphene in the diffusive regime is the mobility of charge carriers μ . Within the Drude-Boltzmann model, it is related to the conductivity and charge carrier density via $\sigma = \mu ne$. Using this formula leads to a mobility of $\mu \approx 26 \times 10^3 \text{ cm}^2 \text{ V}^{-1} \text{ s}^{-1}$ at the saturation density $5 \times 10^{10} \text{ cm}^{-2}$ on the electron side (using $\sigma = (R - R_C)^{-1} \frac{L}{W}$ excluding 150Ω contact resistance). Below this saturation density, the gate is no longer effective as transport is determined by residual disorder, as shown in fig. 4.4 [Du08]. In the top gated sample B, a mobility of $\mu \approx 120 \times 10^3 \text{ cm}^2 \text{ V}^{-1} \text{ s}^{-1}$ at saturation density of $1.2 \times 10^{10} \text{ cm}^{-2}$ is found by the same analysis. Compared to sample B and reports in the literature, where $\mu_C \approx 7 \times 10^4 \text{ cm}^2 \text{ V}^{-1} \text{ s}^{-1}$ for un-encapsulated graphene on hBN [Dea10] and $\mu \gtrsim 1 \times 10^6 \text{ cm}^2 \text{ V}^{-1} \text{ s}^{-1}$ for encapsulated graphene [Wan13] have been reported, the mobility of sample A seems relatively low. However, both devices show clear Fabry-Pérot interference patterns for hole doping (sample A) or in the bipolar regime (sample B) which indicates ballistic transport and questions the full applicability of the Drude-Boltzmann model.

At the charge neutrality point, a residual conductivity of $\sigma_{\min}^A = 3.71 \frac{e^2}{h}$ remains in sample A, and $\sigma_{\min}^B = 5.58 \frac{e^2}{h}$ in sample B.

4.1.2 Shot Noise

In section 2.3.2, ballistic transport was associated with noiseless conduction because transmission channels with $T_n \in \{0, 1\}$ don't contribute to the shot noise signal. Therefore, a clean, short and wide graphene strip in the ballistic regime should show noiseless transport as well. But due to the relativistic nature of the charge carriers in graphene, at vanishing charge carrier density around the Dirac point, transport occurs via evanescent modes. This leads to a universal finite minimum conductivity [Kat11; Kat06a] and sub-poissonian shot noise with Fano factor $\mathcal{F} = \frac{1}{3}$, equal to the one of a disordered metal [Two06]. Due to this analogy, where the transport properties of ballistic graphene become identical to a diffusive system, this novel transport regime is also called "pseudo-diffusive". Figure 4.5 shows the theoretically expected dependence of the minimum conductivity σ_{\min} and the Fano factor \mathcal{F} on the width over length ratio (a,b) and Fermi level (c,d) of a graphene strip. For wide and short samples, the noise is predicted to be gate dependent with a maximum of $\mathcal{F} = \frac{1}{3}$ at the charge neutrality point and $\mathcal{F} \approx 0.12$ at higher density. The theoretical predictions were investigated experimentally by Danneau

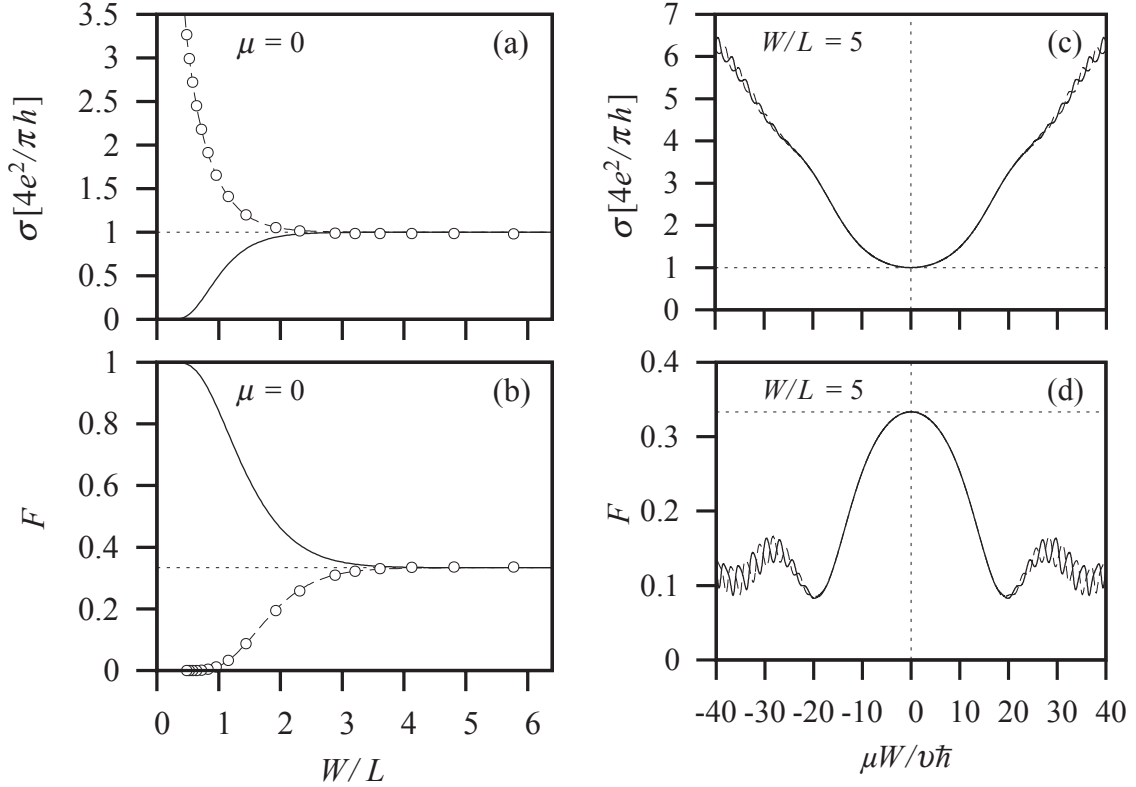


Figure 4.5: **a** Minimum conductivity and **b** Fano factor of a ballistic graphene strip with respect to width over length ratio and **c,d** Fermi level. Solid lines are for smooth edges, dashed lines for armchair edges. Source: Adapted from [Two06] ©2006 American Physical Society

et al. [Dan08] and DiCarlo et al. [DiC08] in 2008, and more recently by Mostovov [Mos14]. All of these previous studies used graphene supported by thermally grown SiO_2 on Si. Until now, the theoretical predication of gate dependent $F=1/3$ has only been observed in one sample by Danneau et al. [Dan08], where the width of the peak in the shot noise was much larger than

theoretically expected [Lew08]. DiCarlo et al. [DiC08] didn't observe any gate voltage dependence and Mostovov [Mos14] didn't reach the ballistic regime.

In this thesis, the graphene is encapsulated in hBN, which ensures ballistic transport, proven by the observation of a clear Fabry-Pérot pattern, as shown in figure 4.2 and in section 4.2.1. The measurement was performed at a higher frequency range and larger bandwidth, which improves the signal level and makes faster and more sensitive measurements possible. The following data for sample A was analyzed using the calibration data of a tunnel junction with $\mathcal{F} = 1$, the bandwidth was 4.6 GHz to 7.2 GHz, and the gain bandwidth product $\text{GBW} = 3.17 \times 10^{18}$ Hz.

At $\frac{W}{L} = 8.6$ for sample A, it can be considered "wide and short", and thus should show $\mathcal{F}_{\text{max}}^{\text{Th}} = \frac{1}{3}$ and $\sigma_{\text{min}}^{\text{Th}} = \frac{4e^2}{\pi h}$ according to the theory. Figure 4.6 shows data of a V_G and V_{DS} double sweep, where for each gate value a bias curve was recorded. The left panel shows the raw data of $|V_{\text{Noise}}|$ for a selection of these bias sweeps. The slope $\Delta V_{\text{Noise}}/\Delta I_{\text{DS}}$ is related to the Fano factor by (3.16) and a clear gate dependence is visible. For every bias sweep, the bias dependent Fano factor $F(I)$ was calculated by integration of the differentially measured noise voltage dV_{Noise} according to (3.17). The red curve in the right panel shows the average of $F(I)$ at high bias.

Opposed to [DiC08], and qualitatively in agreement with [Dan08], the shot noise signal does show a gate dependence, but the peak in the noise at the Dirac point is less sharp than expected. The asymmetry of the electron and hole side could be explained by the p-n junctions that appear due to doping from the contacts for a hole doped channel. However, with only $\mathcal{F}_{\text{max}} = 0.016$, the maximal Fano factor at the Dirac point is much lower than expected for pseudo-diffusive transport. It is reduced by 80 % at high charge carrier density on the electron side, which is more than the theoretically expected relative change of about 64 % from $\mathcal{F}_{\text{Dirac}}^{\text{Th}} = 0.33$ to $\mathcal{F} = 0.12$ [Two06], but in agreement with [Dan08], who also observed vanishing \mathcal{F} at high density, as expected for ballistic transport with propagating states. The minimum conductivity is given by $\sigma_{\text{min}} = 3.71 \frac{e^2}{h} \approx 2.9 \sigma_{\text{min}}^{\text{Th}}$.

Figure 4.7 shows data of another sample made from the same graphene sheet as sample A, but with square geometry $W = L = 1.5 \mu\text{m}$. This measurement was performed in a separate cool-down at $T = 4$ K, with only one room temperature amplifier (hence the reduced level of V_{Noise}), and using the same reference tunnel junction as for the measurement of sample A. The sample and the tunnel junction remained on the sample holder in between the two cool downs, only the connection of the sample holder to the cryostat was changed. Despite the different geometry, the Fano factor is very similar to the data of the short and wide sample, with a maximum of $\mathcal{F} \approx 0.015$ at the Dirac point. The minimum conductivity is given by $\sigma_{\text{min}} = 11.37 \frac{e^2}{h} \approx 8.9 \sigma_{\text{min}}^{\text{Th}}$.

The increased σ_{min} compared to the theoretical value can be attributed to charge puddles [Das11b], i.e. inhomogeneous areas of p and n doping at the overall charge neutrality point. These puddles are strongly suppressed in hBN-supported samples compared to samples supported by SiO_2 , as proven in STM measurements [Dec11]. However, even in very clean hBN-supported or encapsulated samples, the minimum conductivity is regularly larger than the theoretical value. For example in the data of [Cal15], who observe ballistic transport as proven by the observation of Fabry-Pérot interference, the minimum conductivity is $\sigma_{\text{min}} \approx 6.68 \frac{e^2}{h}$,

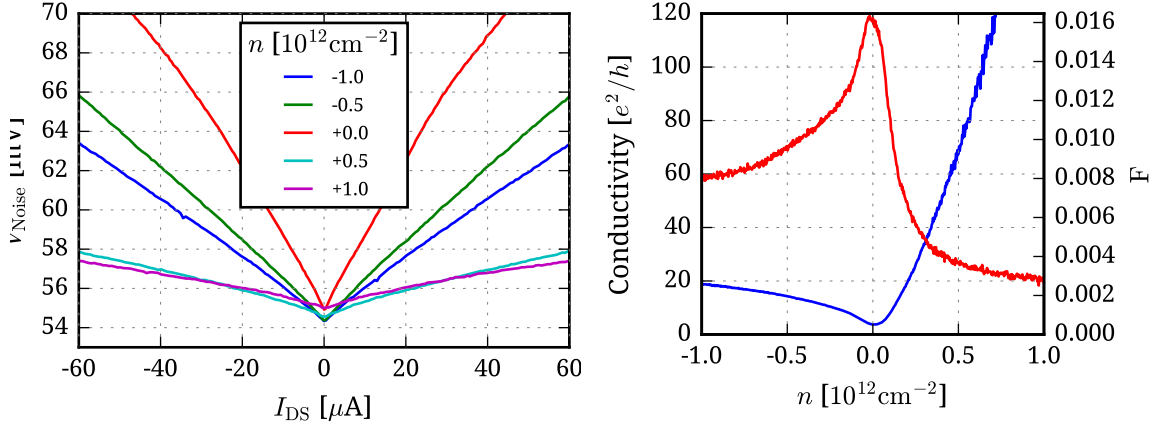


Figure 4.6: Shot noise of sample A at $T_{\text{MC}} = 15 \text{ mK}$ and $B = 20 \text{ mT}$ to suppress superconductivity. **Left:** Raw data of noise voltage V_{Noise} for various gate voltages. **Right:** Conductivity (blue) and Fano factor (red), $F_{\text{max}} = 0.069$ (see text)

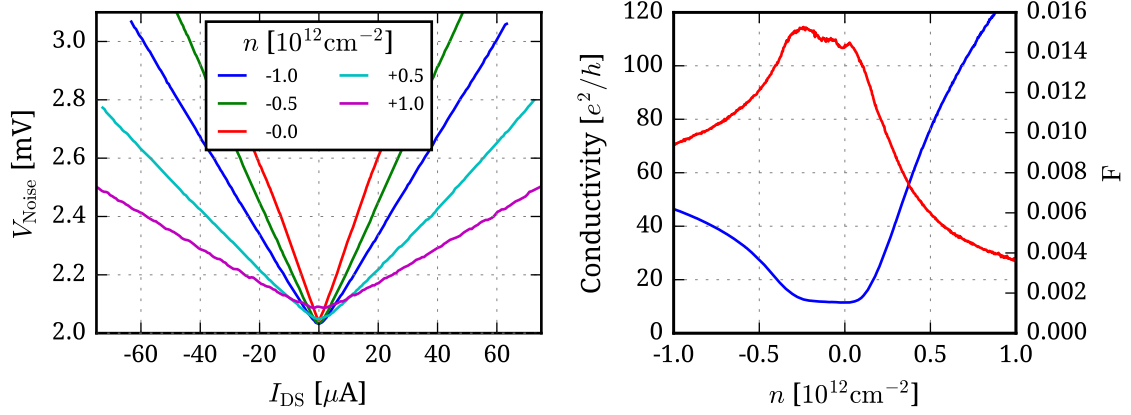


Figure 4.7: Shot noise of a $1.5 \mu\text{m} \times 1.5 \mu\text{m}$ square sample, otherwise similar to sample A, at $T_{\text{MC}} = 4 \text{ K}$. **Left:** Raw data of noise voltage V_{Noise} for various charge carrier densities. **Right:** Conductivity (blue) and Fano factor (red), $F_{\text{max}} = 0.016$ (see text)

i.e. 5.24 times the theoretical minimum¹, and [Kre14] find $\rho_{\text{max}} \approx 3.7 \text{ k}\Omega^2$, corresponding to $\sigma_{\text{min}} = 6.98 \frac{e^2}{h} \approx 5.5 \sigma_{\text{min}}^{\text{Th}}$, while reporting a mean free path of $l_{\text{mfp}} \approx 4 \mu\text{m}$. Thus, the minimum conductivity measured in our samples does not contradict ballistic transport.

In the shot noise data, a very small Fano factor, a stronger-than-expected gate dependence, and no change in \mathcal{F}_{max} for the square sample compared to the short and wide sample were found. While the reduced \mathcal{F} could potentially be explained from an unidentified, spurious attenuation in the measurement setup, the qualitative disagreement might indicate that transport does indeed not occur via evanescent states in these samples at the investigated densities. However, in the diffusive regime, one would expect an even larger, density independent Fano factor $\mathcal{F} > 1/3$ [Lew08].

¹ calculated from the data shown in fig. 1 d) in [Cal15]

² calculated from the data shown in fig. 1 d) in [Kre14]

4.2 Dirac Fermion Optics

Many devices that take advantage of Dirac electron dynamics have been proposed, including a Veselago lens with negative refraction index [Che07] (recently observed in encapsulated graphene [Lee15]), electronic wave guides (observed in suspended graphene [Ric15a]), and transformation optical devices [Vak11]. These Dirac fermion optical experiments are only possible when the elastic mean free path l_{mfp} , or at least the phase coherence length L_φ , is of the order of the geometric sample structure size. In early Fabry-Pérot interference experiments with graphene on SiO_2 , where $l_{\text{mfp}} < L$, only weak oscillations were found [Cho11; Mia07]. A clearer pattern was observed by Young et al. [You09] by using extremely short gate-defined cavities with length $l \approx 20 \text{ nm}$, where $l_{\text{mfp}} \gtrsim 100 \text{ nm}$. For more advanced devices, l_{mfp} in SiO_2 -supported graphene is not long enough. By using suspended, current-annealed graphene, the mean free path could be increased to micrometer scale [Bol08; Du08]. But although promising results have been shown in suspended graphene samples [Gru13; Ric15a; Ric15b; Ric13], sample fabrication is challenging and mechanical stability of the graphene membrane puts tight restrictions on possible device layouts. In substrate-supported graphene, only the improvements of sample quality within the last years, using hBN supported or encapsulated graphene, have made it possible to create complex structures on the length scale of the mean free path. These devices are much more robust and easier to structure than suspended samples, opening up possibilities of making use of Dirac fermion dynamics in technological applications.

4.2.1 Fabry-Pérot Interference

While the shot noise measurements are a proof of charge transmission by discrete “particles”, this chapter will stress the wave nature of ballistic charge carriers in graphene by demonstrating Fabry-Pérot interference effects. This simplest realization of electron optics is based on interference in between two partially reflecting mirrors as shown in 4.8. The phase shift of two neighboring rays is given by $\Delta\varphi = 2\pi \frac{2L \cos \theta}{\lambda}$. Constructive interference occurs at $\Delta\varphi = N2\pi$, resulting in the resonance condition

$$\frac{2L \cos \theta}{\lambda} = N \quad N \in \mathbb{N}. \quad (4.1)$$

In our case, the relevant wavelength is the Fermi wavelength $\lambda_F = \frac{2\pi}{k_F}$, which is related to the Fermi energy through the relativistic dispersion relation $E_F = \hbar v_F k_F$ (2.9). By tuning the gate voltage, the Fermi level is shifted and the Fermi wavelength changes. From (2.14)

$$k_F = \sqrt{\pi n} \Rightarrow \lambda_F = \frac{2\pi}{k_F} = \frac{2\pi}{\sqrt{\pi n}} = \frac{2\pi}{\sqrt{\pi \alpha (V_G - V_{\text{Dirac}})}} \quad (4.2)$$

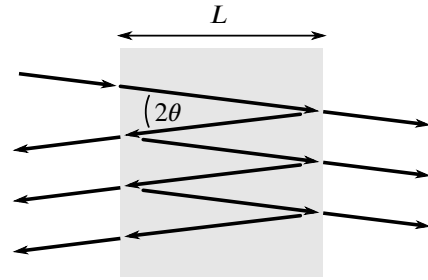


Fig. 4.8: Classical Fabry-Pérot interference in an optical cavity.

The wavelength also depends on the source-drain bias V_{DS} , which can be taken into account through a change of the potential at each contact by $\pm \frac{V_{\text{DS}}}{2}$. This directly alters the charge carrier energy by $\Delta E = \frac{eV_{\text{DS}}}{2}$ [Cho11] and the wave number by $\delta k = \frac{eV_{\text{DS}}}{2\hbar v_{\text{F}}}$. Considering both charge carrier density n and source drain bias V_{DS} , the resonance condition (4.1) at perpendicular incidence ($\theta = 0$) then takes the form

$$N = \frac{2L}{\lambda} = \frac{2L}{2\pi}(k_{\text{F}} + \delta k) = \frac{2L}{2\pi} \left(\sqrt{\pi n} + \frac{eV_{\text{DS}}}{2\hbar v_{\text{F}}} \right) = \frac{L}{\sqrt{\pi}} \sqrt{n} + \frac{L}{2\pi\hbar v_{\text{F}}} V_{\text{DS}} \quad (4.3)$$

$$= L \sqrt{\frac{\alpha_{\text{BG}}}{\pi}} \sqrt{|V_{\text{BG}} - V_{\text{Dirac}}|} + \frac{L}{2\pi\hbar v_{\text{F}}} V_{\text{DS}} \quad (4.4)$$

At first, sample A is considered, where no top gate is present. In this situation, charge carriers propagate freely within the graphene sheet, and are only reflected at the edges and contacts, which is referred to as “massless Dirac fermion billiard” [Mia07]. In the sample presented here, this reflection only occurs for hole doping, at negative gate voltages. The reason lies in the work function difference of graphene and the Ti/Al contact leads [Gio08], which creates a thin electron doped area. When the back gate is tuned to negative voltages, the bulk of the graphene sheet is hole doped, and p-n junctions form at the contacts. These p-n junctions act as mirrors in the Fabry-Pérot interferometer. For positive gate voltages, the junctions are absent, and no oscillations can be observed.

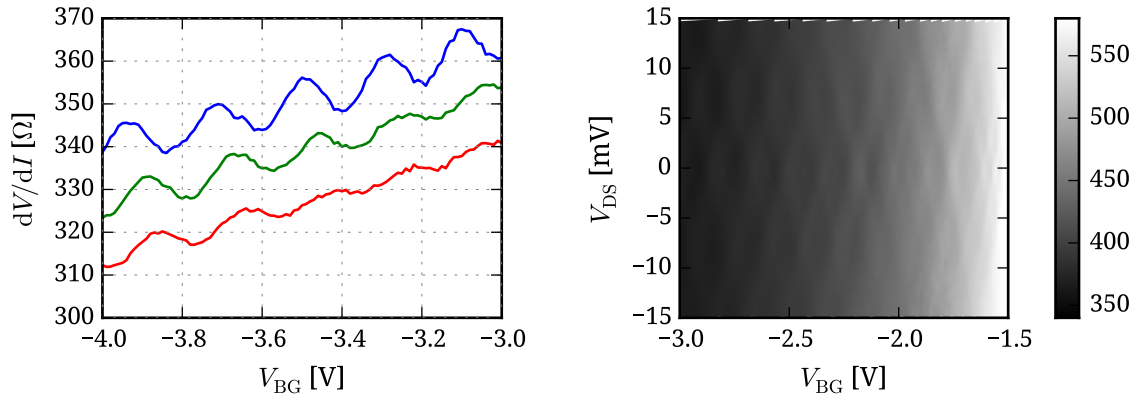


Figure 4.9: (a) Fabry-Pérot oscillations for $B = 200$ mT, 150 mT, 100 mT (top to bottom) at zero bias. (b) The interference pattern is clearly visible in the differential resistance dV/dI vs. back gate V_{BG} and bias V_{DS} at 200 mT.

In the sample without top gate, without magnetic field (20 mT were applied to suppress superconductivity) only very small oscillations are visible, and the interference pattern only showed after applying 100 mT to 200 mT as shown in figure 4.9 (a). This effect might be related to Klein tunneling. The contact induced p-n junctions are more transmissive for charge carriers at perpendicular incidence. Without field, the collimated charge carriers can pass through the junction at the opposing contact with $T = 1$, and without reflection the Fabry-Pérot pattern doesn’t appear. A small field bends the trajectories, where $r_{\text{C}} \approx 500$ nm to 150 nm for the gate range shown in 4.10 at 200 mT. Besides the increasing oscillation amplitude, the oscillations

show a phase shift with increasing field. [You09]

The units in figure 4.10 (bottom) were chosen in such a way that the main interference pattern can be directly related to (4.4). In these units, the resonance condition describes lines

$$V_{\text{DS}} = \pm (2\hbar v_{\text{F}} \sqrt{\pi \alpha_{\text{BG}}}/e) \sqrt{|V_{\text{BG}} - V_{\text{Dirac}}|} + N \frac{2\pi \hbar v_{\text{F}}}{eL} \quad N \in \mathbb{N}. \quad (4.5)$$

The y-intercept only depends on the cavity size L and constants, and the slope only on the gate efficiency α_{BG} and constants, so we can use the Fabry-Pérot interference pattern to extract these values. The white lines (larger pattern) in 4.10 (bottom) are plotted with parameters

$$\alpha_{\text{BG}}^{\text{A}} = 6.75 \times 10^{11} \text{ V}^{-1} \text{ cm}^{-2} \quad \text{and} \quad L = 300 \text{ nm} \quad (4.6)$$

and capture the main pattern quite well. Despite the increasing cyclotron radius r_{C} for decreasing charge carrier density, it remains very regular. r_{C} reaches $\frac{L}{2}$ at $\sqrt{|V_{\text{BG}} - V_{\text{Dirac}}|} \approx -0.5 \sqrt{V}$. At low charge carrier densities and low bias, a second pattern with smaller periodicity emerges which can be described by a cavity with $L \approx 690 \text{ nm}$ (white lines at lower charge carrier density). The geometric dimensions of the sample measured by AFM are $L \approx 350 \text{ nm}$ and $W \approx 3 \mu\text{m}$.

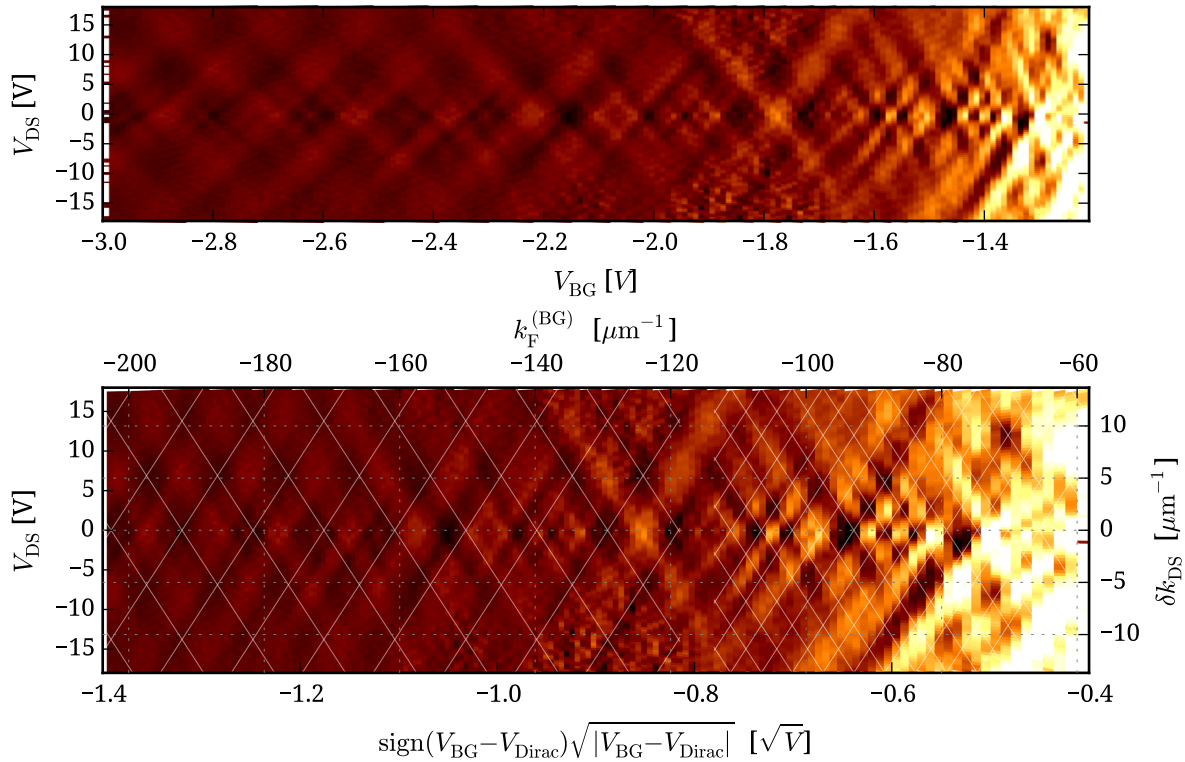


Figure 4.10: Fabry-Pérot interference pattern at 200 mT. The plot shows the differential resistance dV/dI , differentiated vs back gate to enhance the visibility (a.u.). **Top:** distorted pattern with respect to back gate voltage. **Bottom:** regular pattern with respect to square root of gate voltage offset and in k -space. k_{BG} was calculated from the gate efficiency found in (4.6)

4.2.2 Fabry-Pérot Interference in a p-n Junction

In sample B, an additional p-n junction can be introduced in the center between the contacts when the gates are tuned to opposing polarities, with the top gate overcompensating the charge carrier density that is introduced from the back gate. Figure 4.11 shows a map of the differential resistance with respect to top gate and back gate potentials at zero field and zero bias at $T = 4$ K. The map is divided into four regions. The vertical line at $V_{\text{BG}} = 0$ corresponds to charge neutrality in half of the sample, where the top gate has no influence. The second, diagonal line of high resistance corresponds to charge neutrality in the top-gated region, where both the back gate and the top gate control the charge carrier density. In the lower left area, both regions are p-doped, and in the upper right area both regions are n-doped. The remaining regions in between of the two resistance peaks correspond to n-p and p-n doping.

The situation becomes clearer when the gate potentials are converted to charge carrier densities using

$$n_{\text{BG}} = \alpha_{\text{BG}}(V_{\text{BG}} - V_{\text{Dirac}}) + \alpha'_{\text{TG}}V_{\text{TG}} \quad (4.7)$$

$$n_{\text{TG}} = \alpha_{\text{BG}}(V_{\text{BG}} - V_{\text{Dirac}}) + \alpha_{\text{TG}}V_{\text{TG}}, \quad (4.8)$$

where n_{BG} refers to the area that is only affected by the back gate (a small effect shows as a slight slope in the gate map, and is described by α'_{TG}), and n_{TG} refers to the area that is affected by both top gate and back gate. The exact gate efficiencies $\alpha_{\text{BG}}^{\text{B}}$ and α_{TG} were extracted from Shubnikov-de Haas measurements, which will be presented in detail in section 4.3.1.

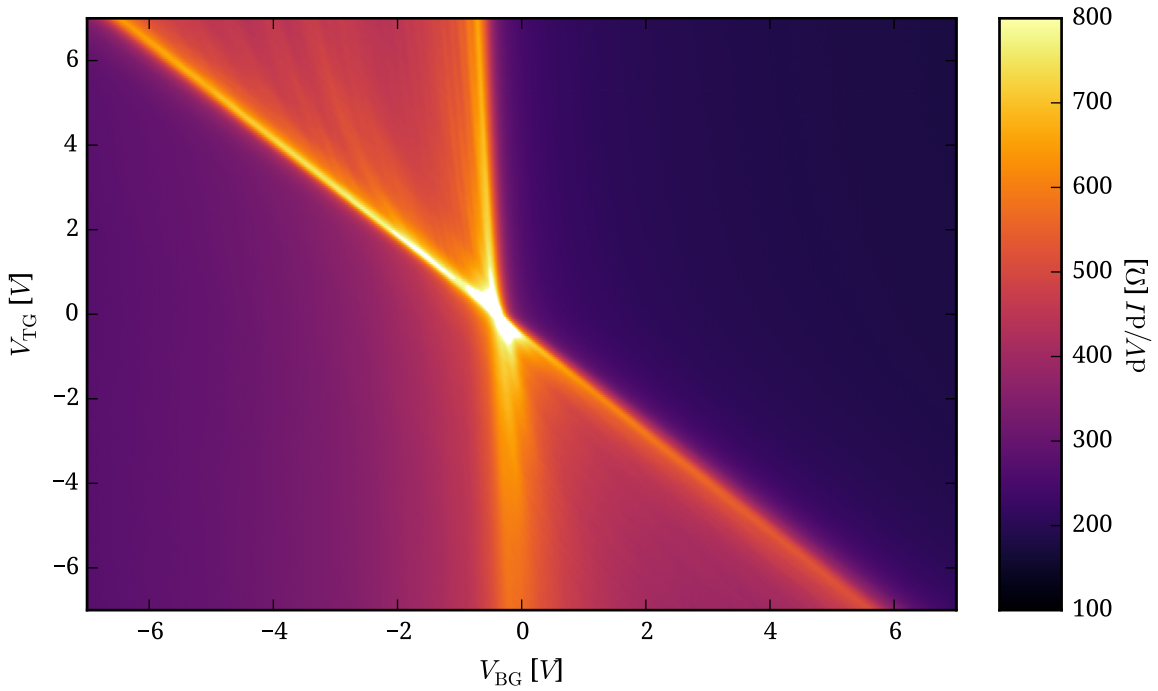


Figure 4.11: Differential resistance dV/dI versus top gate and back gate.

In this representation, shown in figure 4.12, the four different regions are mapped to the plot quadrants. The plot shows the differential resistance, numerically differentiated with respect to the back gate voltage (i.e. the sweep parameter) to enhance the visibility of the Fabry-Pérot oscillation pattern. Oscillations can be observed in the p-n (top left) and n-p (lower right) regions, but are absent in both n-n (top right) and p-p (lower left) doping. In the p-n and n-p regions, the potential on the top gate has to be twice as strong as the potential on the back gate. This restricts the measurement parameter space, and the missing data is shown as white areas.

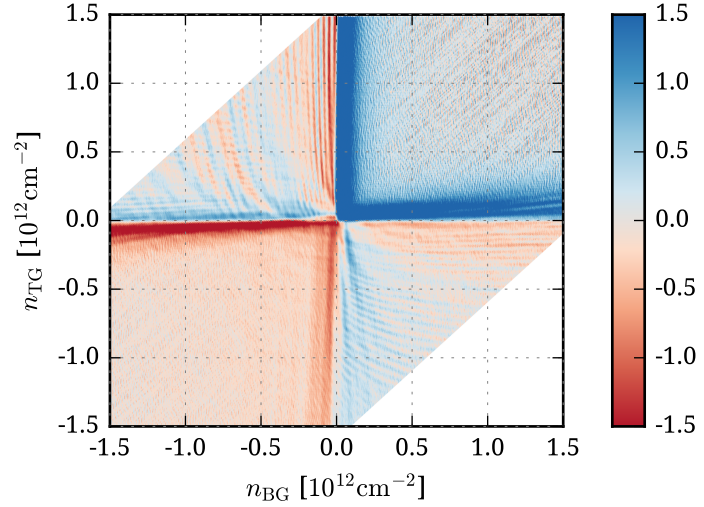


Fig. 4.12: Gate map of $d(dV/dI)/dV_{BG}$ (a.u.) plotted versus charge carrier density

Analogous to the examination of the Fabry-Pérot pattern in section 4.2.1, we can transform the data to account for the physical background. With $V_{DS} = 0$, the resonance condition 4.5 is simplified to

$$N = \frac{2L}{\lambda_F} = \frac{L}{\pi} \sqrt{\pi n} = \frac{L}{\pi} k_F \quad (4.9)$$

for each half of the sample, so the oscillation pattern is periodic in $k_F = \sqrt{\pi n}$. The plots in figure

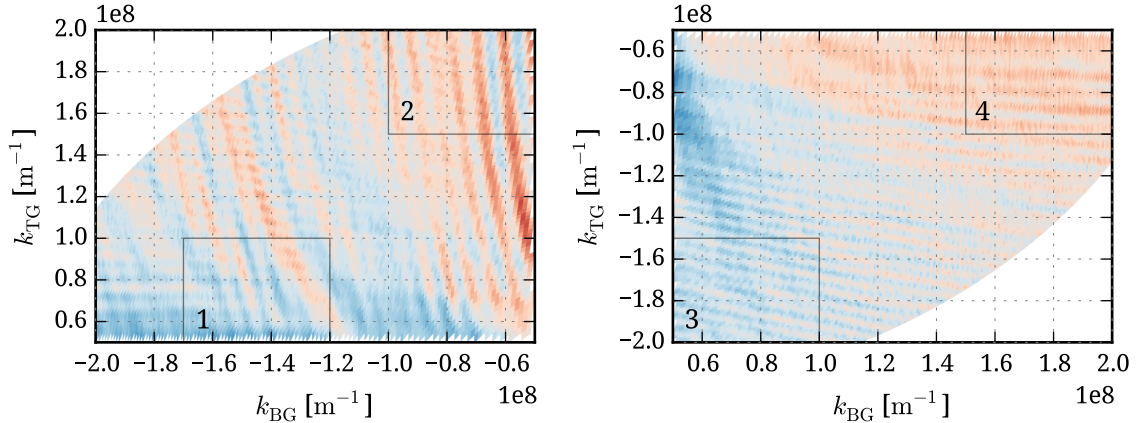


Figure 4.13: Fabry-Pérot pattern in p-n and n-p regions, plotted versus wave number. Color scale is identical to 4.12.

4.13 show the Fabry-Pérot pattern in the p-n and n-p regions in k -space. Since the measured data points are equally spaced in terms of the gate voltages, few points were recorded at very small k_F . In each regions, one can find oscillation versus both k_{BG} and k_{TG} . The vertical lines correspond

to oscillations that are independent of k_{TG} , so they can be attributed to the non-top gated cavity, and horizontal lines accordingly originate from interference below the top gate. In some regions, for example region 1, both vertical and horizontal lines are visible. Opposed to the situation in 4.2.1, these oscillations don't originate from the same cavity. The interference pattern is again regular, but the periodicity is not entirely constant, as can be seen by comparing the horizontal lines in regions 3 and 4.

To investigate the oscillations further, the periodic pattern can be Fourier transformed. The resonance condition 4.9 leads to a periodicity of $\Delta k = \frac{\pi}{L_{\text{Cavity}}}$ in k -space. Fourier transformation results in a plot with units of $k^{-1} = \frac{\lambda}{2\pi}$, so the resonance condition is fulfilled at $\frac{L_{\text{Cavity}}}{\pi}$. Thus, by scaling the axes of the Fourier transformed plot by π , the cavity size corresponding to an interference pattern can be directly found from the coordinates of a peak in the plot.

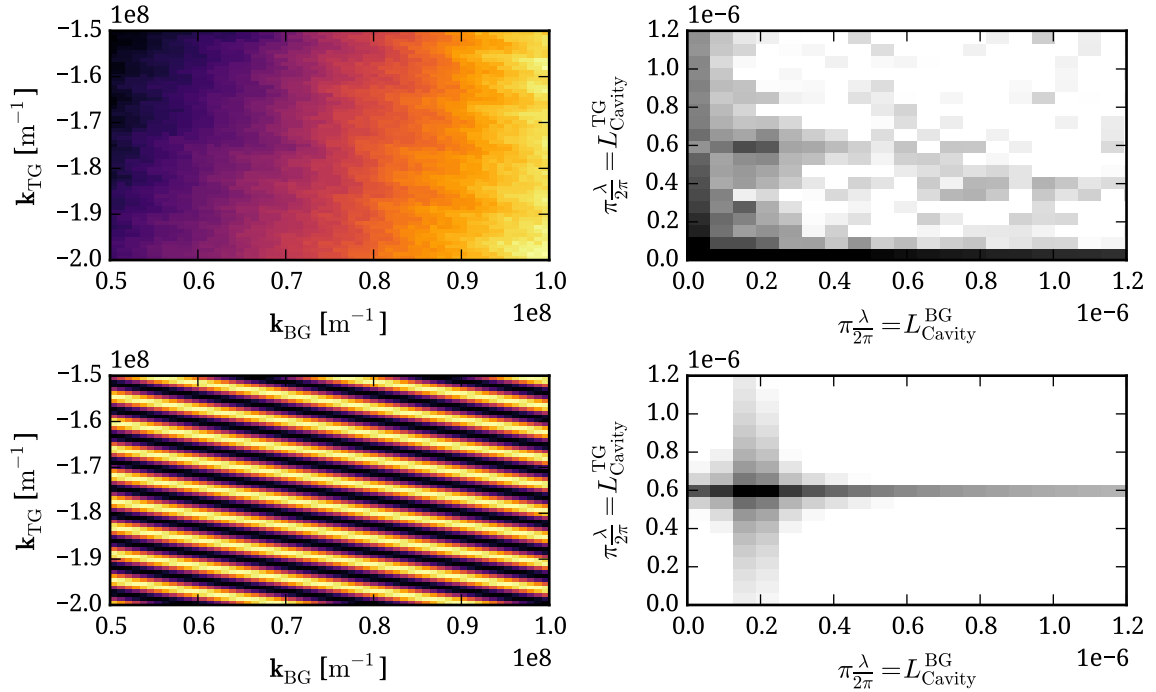


Figure 4.14: **TL:** Measured differential conductance dI/dV in region 3. **TR:** Two dimensional Fourier transform, scaled with π to show cavity size $\pi \frac{\lambda}{2\pi}$. **BL:** Simulated pattern for the peak at $L_{\text{TG}} = 0.55 \mu\text{m}$ (and $L_{\text{BG}}^* = 0.15 \mu\text{m}$). **BR:** Fourier transform of the simulated pattern

Figure 4.14 shows the process for region 3 of figure 4.13. The measured differential conductance dI/dV was Fourier transformed, leading to the top right plot. A peak can be found at coordinated $L_{\text{TG}} \approx 0.55 \mu\text{m}$ and $L_{\text{BG}}^* \approx 0.15 \mu\text{m}$. Here, the component in the direction of L_{BG} is responsible for the slope of the oscillation pattern, which could be caused by stray fields and inhomogeneous charge carrier density in the channel, which is not taken into account in the calculation of k . Since the identification of the peak in the Fourier transformed data is a little ambiguous, an oscillation pattern using the extracted cavity size was simulated. It is shown together with its Fourier transform in the lower row of figure 4.14, and evidently reproduces the observed oscillation pattern. The procedure was repeated for each of the four regions shown in

figure 4.13. In region 1 and 2, oscillations in both cavities can be found, while region 3 and 4 only show oscillation below the top gate.

The sizes of the Fabry-Pérot cavities are shown in 4.1. Comparing the cavity size of the interference pattern in the top gated part, one can find an increase in L_{TG} with increasing top gate potential, i.e. from region 1 to 2 or from region 4 to 3. This effect can be attributed to electrostatic effects that shift the p-n junction within the channel depending on the top gate and back gate potentials, as the hBN and Al_2O_3 double layer dielectric that separates the graphene from the top gate has a total thickness of 75 nm, and the back gate dielectric 65 nm (see table 3.2).

Region	L_{BG}	L_{TG}
1	350 nm	510 nm
2	450 nm	350 nm
3	550 nm	-
4	380 nm	-

Table 4.1: Fabry-Pérot cavity sizes

4.2.3 Shot Noise of a p-n Junction

A smooth graphene pn-junction acts as an angle dependent filter for Dirac electrons, with a transmission probability [Che06]

$$w(\theta) = e^{-\pi(k_F d) \sin^2 \theta}, \quad (4.10)$$

where d is the length of the potential step and θ the angle of incidence. For perpendicular incidence, charge carriers can pass through the barrier with $T = 1$ due to Klein tunneling [Kat06b]. This selection of charge carriers was predicted to result in an universal Fano factor of $\mathcal{F} = 1 - \sqrt{\frac{1}{2}} \approx 0.29$, close to the one of graphene at the Dirac point, yet without the gate dependence [Che06]. Due to the failed calibration for the measurement of sample B, the following noise data will be presented using calibration data of a previous cool down with $\text{GBW} = 3.16 \times 10^{18}$ Hz at a bandwidth of $\text{BW} = 4.6$ GHz to 7.2 GHz. Figure 4.15 shows the differential resistance of sample

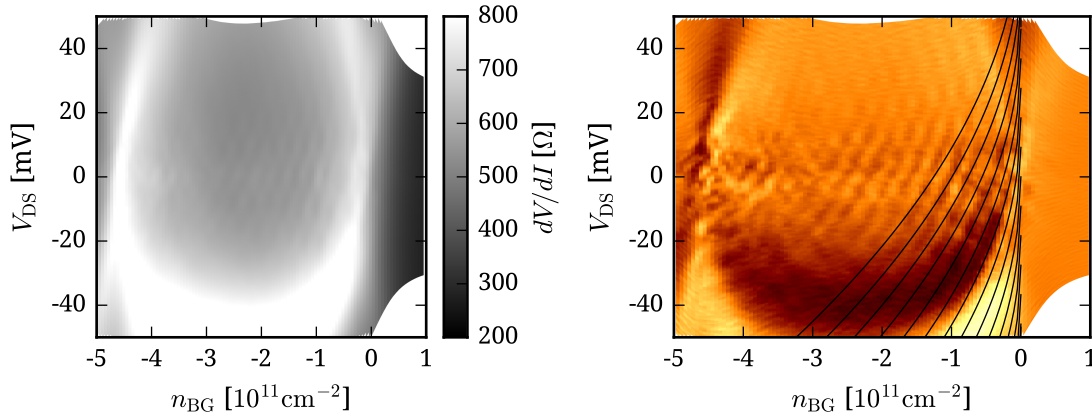


Figure 4.15: Fabry-Pérot resonances in the pn-junction vs. charge carrier density and bias. Left panel shows resistance, right panel is differentiated to enhance the visibility. The black lines follow constant λ_F

B at $V_{TG} = 2$ V at 4 K. The back gate was swept from -2.5 V to 0 V, and for each back gate value a bias sweep was performed, so that a horizontal slice at $V_{DS} = 0$ is equivalent to a horizontal slice at $V_{TG} = 2$ V in figure 4.11. The black lines correspond to constant Fermi wavelengths λ_F

according to 4.5 with $L = 450$ nm from the previous section (region 2). Most interestingly, the sample shows asymmetric behavior with respect to the applied bias. At higher negative bias, a resistance peak connects the two Dirac points. The interference pattern helps understanding the reason for the resistance peak. Since the top gated contact is grounded, decreasing the applied bias to negative voltages means injecting electrons in the back gated region. By decreasing the back gate voltage, the additional charge can be compensated and the Fermi level and Fermi wavelength stay constant, which shows as resonance line in the plot. In this sense, the x-axis label is misleading, it only shows the actual charge carrier density at zero bias. Since the lines show lines of constant charge carrier density, there is a density gradient when crossing them in the vertical direction. The Dirac point with respect to the applied bias is the overall resistance maximum. It is defined by both the top gated and the back gated parts of the sample. When tuning the junction from pn to np, the resistance peak moves to positive bias.

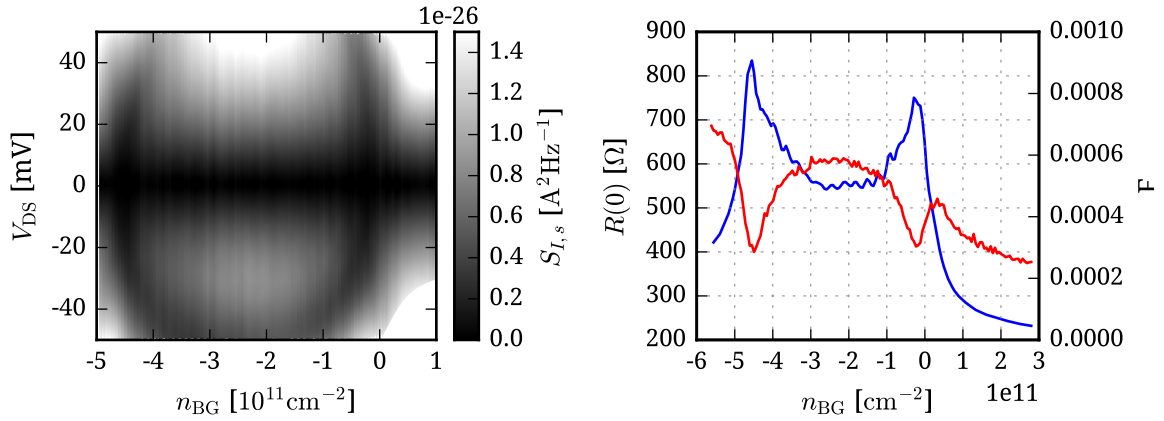


Figure 4.16: Spectral current noise at the sample $S_{I,s}$, **left:** calculated from 3.18, assuming constant R_d , **right:** Resistance at zero bias (blue) and Fano factor as defined in (3.17), averaged from $V_{DS} = 10$ mV to 20 mV.

The overall noise level is again much lower than expected, yet due to the missing calibration data, it can't be excluded that the attenuation of the system was changed in between the cool downs, especially since the calibration measurement and the sample measurement were separated by 2 months. Yet, even qualitatively, the shot noise of the p-n junction shows the opposite of the expected behavior, where the Fano factor has minima at the Dirac points of each half of the sample. This is already visible in the V_{Noise} raw data, as shown in figure 4.17.

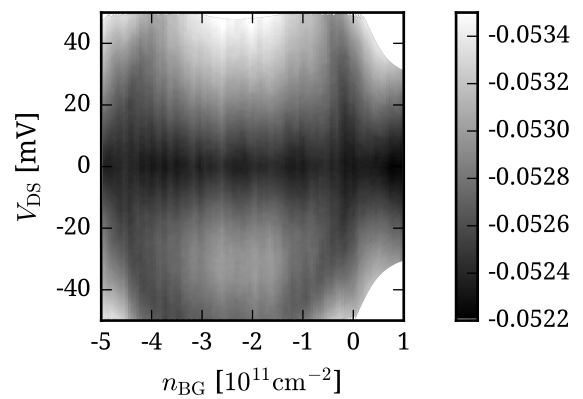


Fig. 4.17: V_{Noise} raw data

4.2.4 Snake States

While the Fabry-Pérot interference presented in the previous chapter has a direct analogy in light optics, the experiment presented in this chapter makes direct use of the unique properties of Dirac fermions. Opposed to photons, the trajectories of Dirac fermions can be manipulated using magnetic fields, where a (moderate) field B perpendicular to the graphene plane forces the charge carriers onto circular trajectories with cyclotron radius (2.17)

$$r_C = \frac{\hbar k}{eB}. \quad (4.11)$$

The key advantage of Dirac fermion optics compared to normal electron optics is the possibility to seamlessly tune the Fermi level from conduction to valence band, switching the sign of the carrier charge and thus inverting the direction of the Lorentz force. In normal 2DEG, this would require manipulation of the local magnetic field on the scale of the mean free path, which is extraordinarily more difficult than local electrostatic gating [Ye95]. Furthermore, the missing gap in the band structure, minimal conductivity, and Klein tunneling make the interface between n and p regions transparent. With the recent advances in sample quality, the mean free path increased far into the micrometer range. This enables designing electrostatic gate structures which guide Dirac fermions from one region to the other with little loss.

The simplest geometry showing this effect is realized in the p-n junction in sample B. In a magnetic field, and for opposite doping in the two halves of the sample, the charge carriers follow circular trajectories in opposite directions. When they get transmitted through the p-n interface, the direction of the curvature is inverted. This directs the trajectories back to the p-n interface, where the process is repeated (fig 4.18). In this way, the p-n interface guides the charge carriers, creating current carrying states called “Snake States” [Ric15b; Tay15; Wil11]. In the two lead sample, the p-n junction ends at the sample edge. Here, depending on the value of r_C , the states end either within the P or the N region, where they continue as skipping orbits into the contact leads. This process causes oscillations in the conductance when changing the cyclotron radius r_C , or constant conductance along lines of constant r_C .

With $r_C = \frac{\hbar k}{eB} = \frac{\hbar\sqrt{\pi n}}{eB}$ and hence $n = \frac{1}{\pi} \left(\frac{r_C e}{\hbar} \right)^2 B^2$, lines of constant r_C are parabolas in a plot versus charge carrier density n and perpendicular magnetic field B . Figure 4.19 shows a measurement where these two parameters were tuned, analogous to recent measurements in suspended graphene [Ric15b] and encapsulated graphene [Tay15]. The absolute charge carrier density was kept equal in the p and n regions during the measurements by adjusting the gate voltages according to $V_{TG} = 2.33(V_{BG} - V_{Dirac})$ (measuring along the dashed line in figure 4.23). The top half of the plot has been overlaid with lines of constant r_C . The dashed green and blue lines define the parameter space where snake states can exist. The dashed green line indicates a cyclotron radius that is equal to half of the sample length. For larger r_C , the trajectories collide

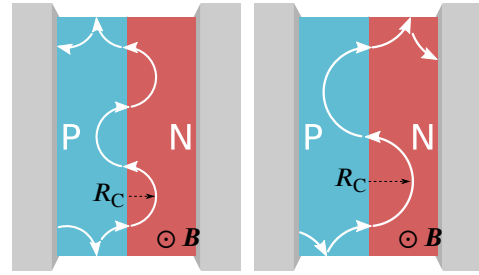


Fig. 4.18: Snake States at a p-n interface cause oscillations in the conductance when r_C is varied.

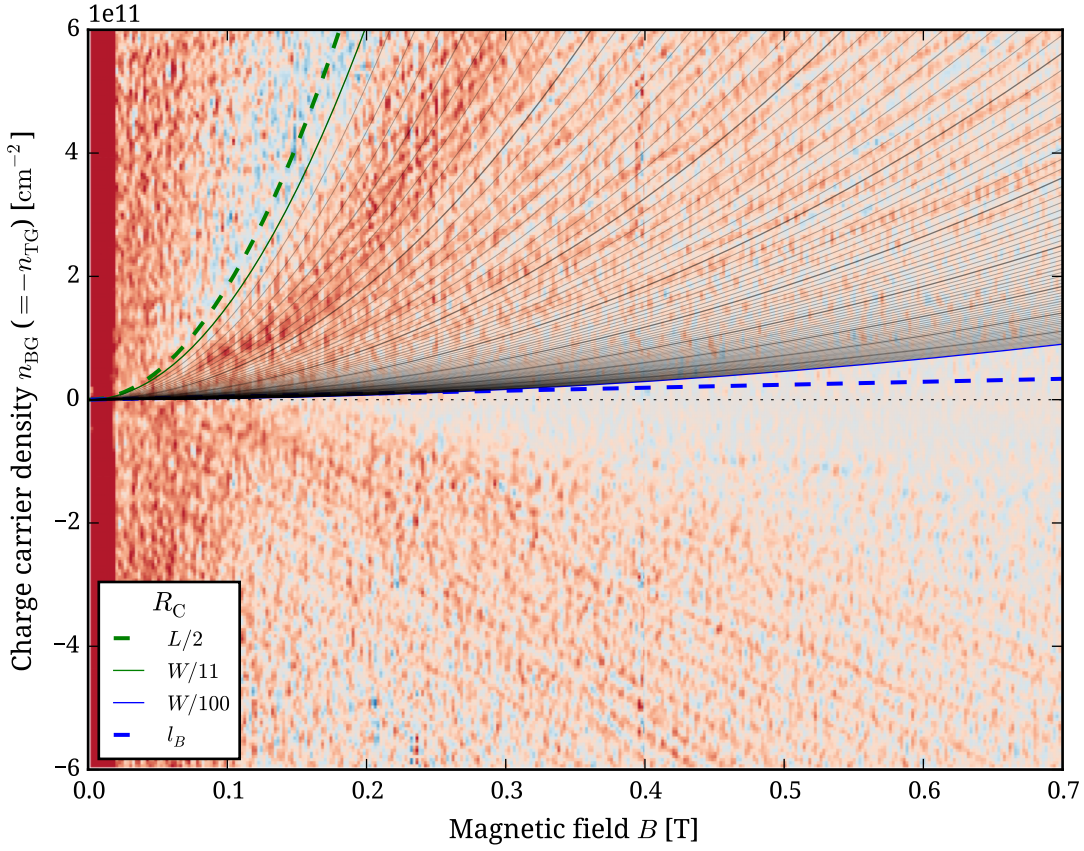


Figure 4.19: Differential conductance, differentiated vs V_{TG} . The dashed green line shows $r_C = L/2$. The solid blue and green lines, and the grey lines in between, show lines of constant r_C , where the lightest lines are located at integer divisions of the sample width, $r_C = W/N$, $N \in \mathbb{N}$. The dashed red line marks the magnetic length $r_C = l_B$, the border to the quantum Hall regime. The plot was combined from three measurements, with seams at 250 mT and 400 mT

with the contact leads, where they are either absorbed or reflected, leading to Fabry-Pérot interference (see section 4.2). When r_C gets into the order of the magnetic length $l_B := \sqrt{\frac{\hbar}{eB}}$, the sample enters the Quantum Hall regime.

These two bordering lines can easily be identified in the measured data. In the intermediate region, the gray lines indicate constant r_C at integer fractions of the sample width, i.e. the expected periodicity of the snake state pattern. Here, oscillations can be found in the data that roughly follow the expected parabolas, with similar periodicity, albeit at a slightly smaller slope.

In figure 4.20 (top left), the upper half of the data shown in 4.19 is plotted again, but versus the wave number $k = \sqrt{\pi n}$ instead of the charge carrier density, so that the lines of constant r_C show as straight lines $k = \frac{r_C e}{\hbar} B$. The color map shows the differential conductance, differentiated versus back gate voltage instead of top gate voltage. This enhances the visibility of the Fabry-Pérot interference pattern that is clearly visible for $r_C < \frac{L}{2}$ and abruptly ends at the expected line. The bottom figure shows an extension of the measurement up to 3 T. Clear lines are

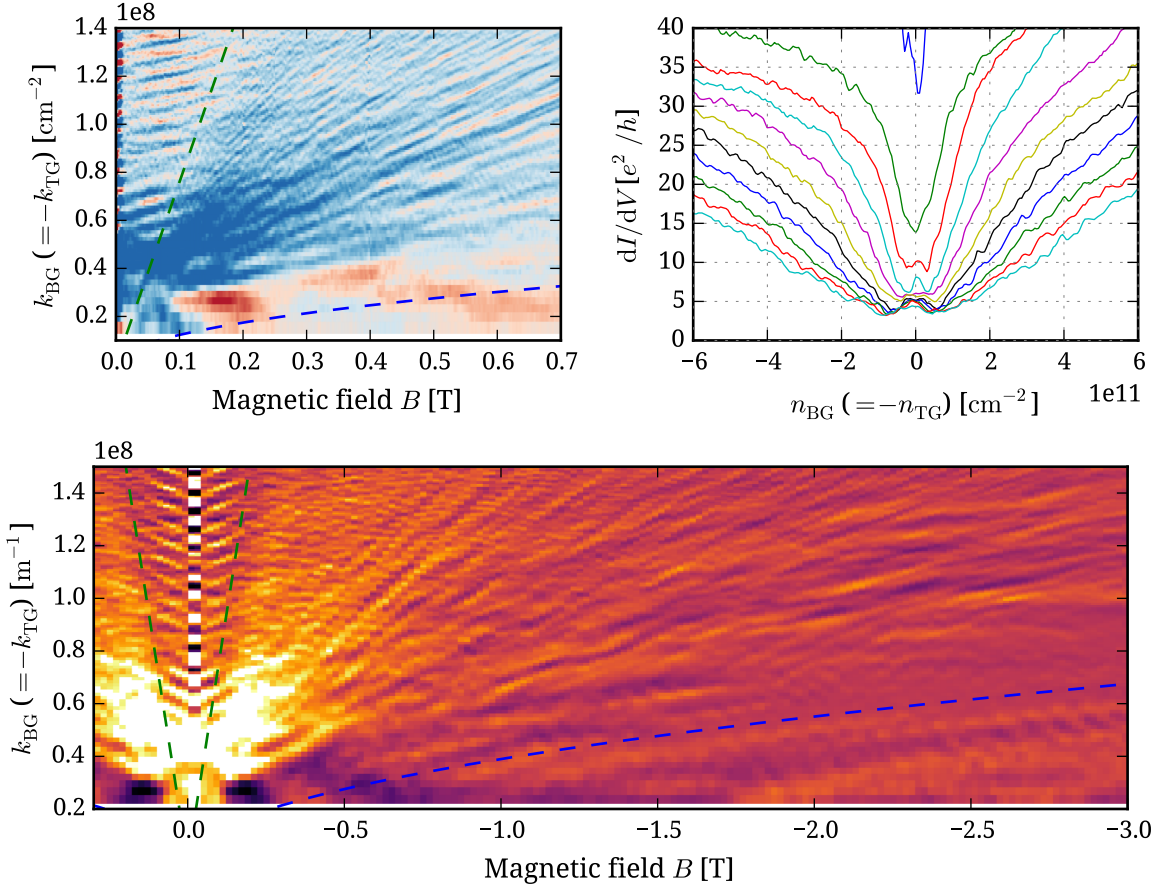


Figure 4.20: Additional plots of snake states. **Top left:** Snake states plotted versus k and B , green and blue lines correspond to the ones in 4.19. **Top right:** Line plots of the differential conductance dI/dV for $B = 0$ mT to 700 mT (top to bottom). **Bottom:** Extended measurement up to 3 T.

visible up to ≈ 1 T, but signs of snake states are still visible at $k = 1.4 \times 10^8 \text{ m}^{-1}$ and $B = 2.5$ T, corresponding to $r_C \approx 37$ nm. In these conditions, particles have to be transmitted $W/r_C \approx 135$ times through the interface to travel along the entire width of the p-n interface in the simplified model, where the junction is assumed perfectly sharp. Smoothing of the potential step causes an additional electrical field that elongates the trajectory along the interface, reducing the number of necessary orbits [Ric15b].

Since the conductance oscillations are caused by a partitioning process, one could expect a signature of snake states in shot noise measurements. But due to the small amplitude of the oscillations in this sample, attempts to measure it remained without result.

4.3 High Magnetic Fields

4.3.1 Shubnikov-de Haas Oscillations

If the magnetic field B_{\perp} is increased further, the cyclotron orbits that were investigated in the previous chapter become quantized and charge carriers in the bulk become localized. The sample undertakes a phase transition and enters the quantum Hall regime, a topological state where the bulk of the 2DEG turns insulating and charge transport occurs only through edge channels that emerge from the skipping orbit trajectories. In this situation, the density of states splits into Landau Levels, which are located at energies given in graphene by (2.20) as

$$E_N = \pm \sqrt{2e\hbar v_F^2 B \left(N + \frac{1}{2} \pm \frac{1}{2} \right)}, \quad N = 0, 1, 2 \dots$$

where the square-root dependence is unique to relativistic massless fermions. This change in the density of states is reflected in many quantities, and its effect on the conductivity is known as Shubnikov-de Haas effect.

Calculation of charge carrier densities

The filling factor depends on the charge carrier density and field strength as given by (2.20)

$$\nu = \frac{n}{4n_L} = \frac{nh}{eB}.$$

While a multi-terminal Hall bar structure would show the well known quantum Hall effect – exactly quantized plateaus in σ_{xy} and vanishing conductivity σ_{xx} within the plateaus – the two-terminal conductance G considered here shows a different behavior and depends on both σ_{xy} and σ_{xx} [Aba08; Wil09]. Furthermore, opposed to σ_{xy} and σ_{xx} , G depends on the sample geometry, i.e. the width over length ratio. Figure 4.21 (a) shows the calculated conductance

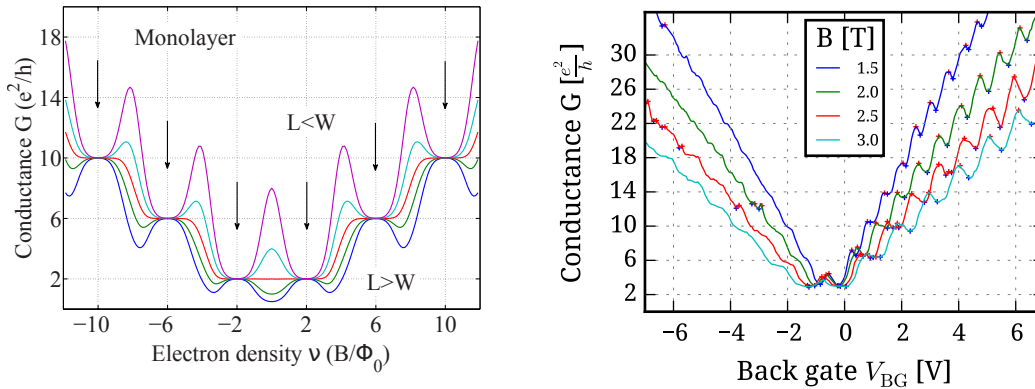


Figure 4.21: (a) Calculated two terminal conductance versus filling factor for various ratios for $W/L = 0.25, 0.5, 1, 2, 4$ (top to bottom). Source: [Aba08], ©2008 American Physical Society (b) Measured conductance versus gate voltage V_{BG} for $B = 1.5$ T to 3 T (top to bottom).

versus filling factor ν . The red curve corresponds to a square sample, where $G_{L=W} = \sqrt{\sigma_{xx}^2 + \sigma_{xy}^2}$, so $G = \sigma_{xy}$ within the plateaus of σ_{xy} . When deviating from the square shape, there is a qualitative difference whether the sample is elongated or widened, where in the first case minima appear between the points of incompressible densities (where no partially filled Landau levels exist), while in the latter case maxima appear. In either case, the conductance at the points of incompressible densities is independent of W/L and given by $G_\nu = \nu \frac{e^2}{h}$. In measurements presented here, the sample has a width over length ratio of $\frac{W}{L} = \frac{5 \mu\text{m}}{1 \mu\text{m}} = 5$, and the points of incompressible density are located at the minima of G . By determining the filling factor ν that corresponds to a certain gate voltage V_{BG} (charge carrier density n) and the external field B , this allows a precise measurement of the gate efficiency α_{BG} (defined as $n =: \alpha_{\text{BG}} V_{\text{BG}}$, where negative n corresponds to hole conduction). Figure 4.21 (b) shows a measurement of the conductance G versus the back gate voltage V_{BG} for $B = 1.5 \text{ T}$ to 3 T . The plateaus on the hole side (negative V_{BG}) are much less pronounced and show lower conductance than on the electron side, which can be explained from p-n junctions forming at the contacts due to the different work functions of graphene and Ti/Al. Thus, only electron conduction is considered for the determination of α_{BG} .

Figure 4.22 shows the conductance of sample B at $V_{\text{TG}} = 0$, differentiated with respect to the back gate voltage dG/dV_{BG} to enhance the visibility of Shubnikov-de Haas oscillations, versus a double sweep of back gate V_{BG} and field B . The three horizontal black lines indicate the sweeps shown in figure 4.21 (b), the line at $B = 0$ is due to the sample becoming superconducting. In

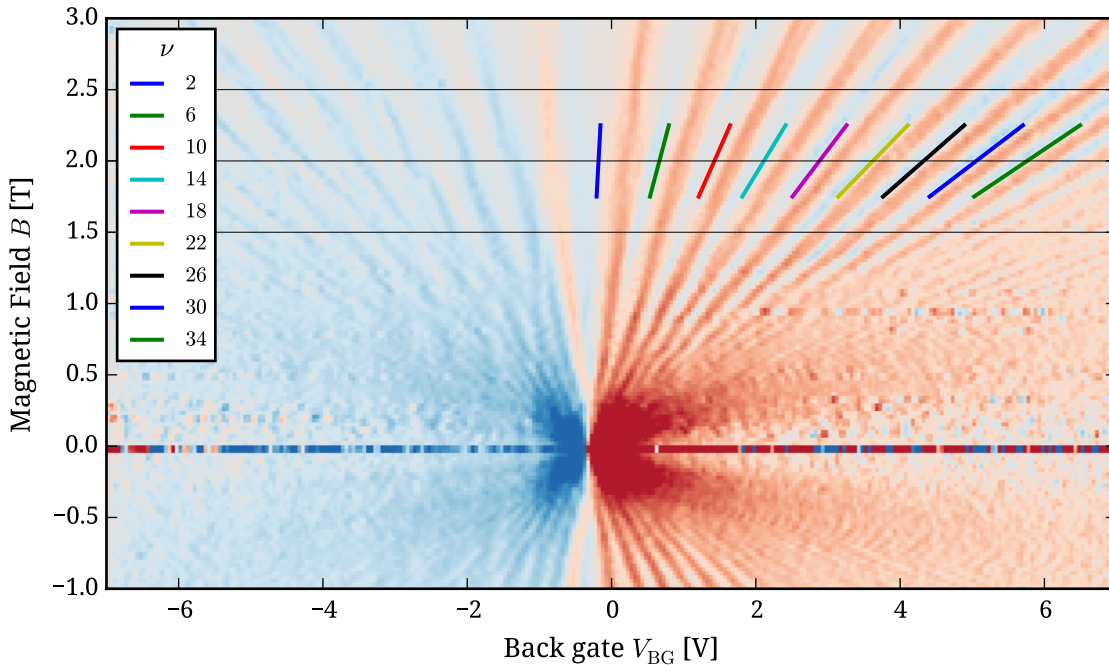


Figure 4.22: Landau fan: dG/dV_{BG} (A.U.) versus gate voltage V_{BG} and magnetic field B .

this representation, called Landau fan, the positions of the minima in conductance follow

$$V_{\text{BG}}^{\text{min}} = \frac{ve}{h\alpha_{\text{BG}}} B, \quad (4.12)$$

so α_{BG} can be precisely determined from the slope of linear fits. The positions of the local minima in $G(V_{\text{BG}})$ are found automatically for each curve (as shown by the blue crosses in fig. 4.21 (b)), assigned to filling factors and fitted linearly. Segments of these fitted lines and respective filling factors are shown in fig. 4.22. Note that the positions of minima in the conductance appear at zero crossings of the plotted dG/dV_{BG} . For the slope m_v of each line, $\alpha_{\text{BG}} = \frac{ve}{hm_v}$ is calculated, with an average of

$$\alpha_{\text{BG}} = 2.80 \times 10^{15} \text{ V}^{-1} \text{ cm}^{-2} \quad (4.13)$$

Using this value for α_{BG} , α_{TG} can be determined from the slope of the charge neutrality lines in the gate map 4.23, where

$$\frac{\Delta V_{\text{TG}}}{\Delta V_{\text{BG}}} = \frac{\alpha_{\text{TG}}}{\alpha_{\text{BG}}} = m_{\text{TG}} \Rightarrow \alpha_{\text{TG}} = 2.40 \times 10^{15} \text{ V}^{-1} \text{ cm}^{-2}, \quad (4.14)$$

and equivalently for the contribution of V_{TG} to n_{BG} , given by $\alpha'_{\text{TG}} = 1.32 \times 10^{14} \text{ V}^{-1} \text{ cm}^{-2}$. The gate efficiency of sample A was found by comparison of the hBN thickness.

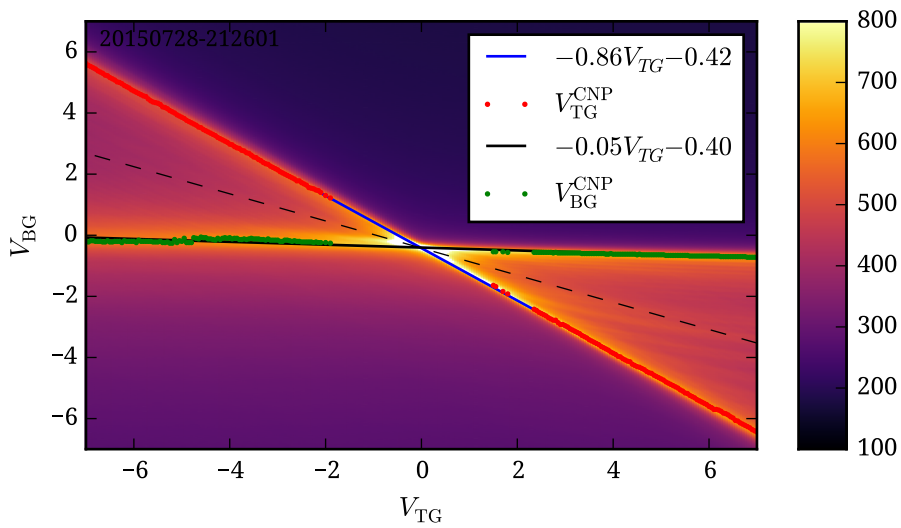


Figure 4.23: Fit of charge neutrality lines to determine α_{TG}

Parameter	Sample A	Sample B
$\alpha_{\text{BG}}^{\text{B}}$	$3.55 \times 10^{11} \text{ V}^{-1} \text{ cm}^{-2}$	$2.80 \times 10^{11} \text{ V}^{-1} \text{ cm}^{-2}$
α'_{TG}		$1.32 \times 10^{10} \text{ V}^{-1} \text{ cm}^{-2}$
α_{TG}		$2.40 \times 10^{11} \text{ V}^{-1} \text{ cm}^{-2}$
V_{Dirac}	-1.05 V	-0.40 V
$V_{\text{Dirac}}^{\text{TG}}$		-0.42 V

Table 4.2: Gate efficiencies

Contact Resistance

Figure 4.24 (a) shows the measured minimal conductance along the lines of incompressible density in fig. 4.22 with respect to the field B . For these lines, the conductance should be given by $G_{\nu} = \nu \frac{e^2}{h}$. The horizontal lines indicate the theoretical value, the dots of the same color show the measured values. For small filling factors or at small fields, the measured conductance is higher than $\nu \frac{e^2}{h}$. This can be explained from Landau level broadening, which smears the quantization so that the conductance minimum is not reached anymore. Higher levels at larger fields show a reduced conductance compared to the theoretical value, where the deviation seems to increase with ν . This deviation can be explained from an approximately constant series resistance, consisting of the contact resistance R_{co} and resistance of the leads R_{l} . Figure 4.24 (b) shows the deviation $\delta R = R_{\nu} - \frac{h}{\nu e^2}$ in units of resistance. For levels $\nu > 10$, the series resistance is in the order of 100Ω to 200Ω and seems to increase with field and charge carrier density. The drop towards smaller fields, reaching 0 at 1 T, is most likely not caused by a vanishing contact resistance, but by increased conductance from broadened Landau levels. The actual contact resistance could then be estimated from the asymptotic behavior for larger fields, yielding $R_{\text{co}} \approx 200 \Omega$.

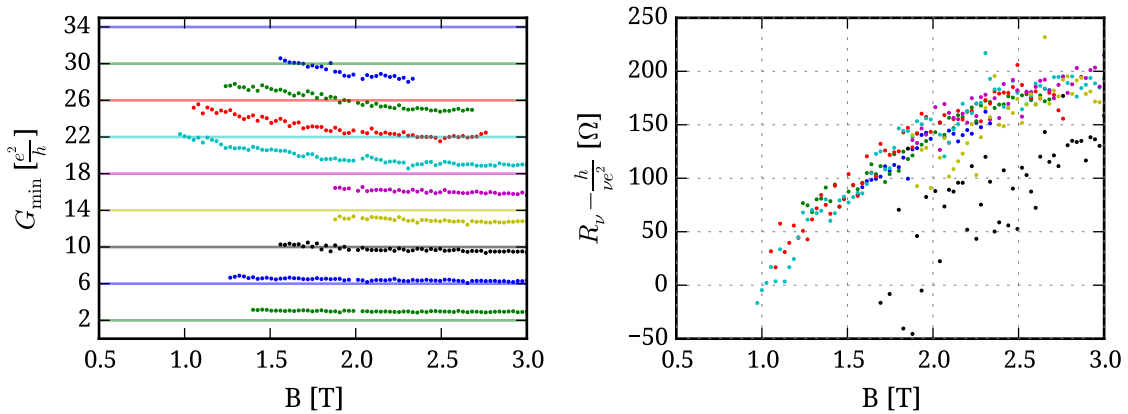


Figure 4.24: (a) Values of conductance minima along the lines of incompressible densities in fig. 4.22. Colored lines show theoretical values for the equally colored dots. (b) Deviation in units of resistance, colors are the same as in (a)

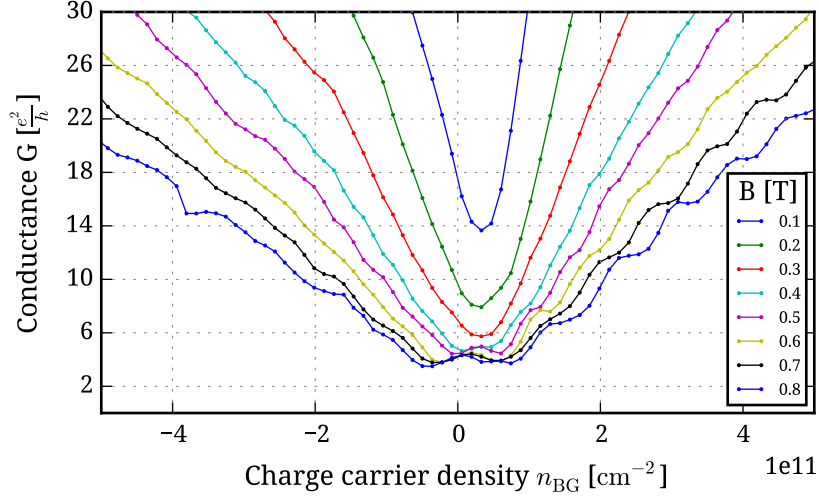


Figure 4.25: Onset of Shubnikov-de Haas oscillations at small fields.

Onset of Shubnikov-de Haas Oscillations

Looking at the onset of Shubnikov-de Haas oscillations at small fields, we can estimate a scattering time τ in a semi classical model, assuming that the oscillations appear when the charge carriers start to self-interfere after completing one cyclotron orbit without scattering [Bol08]. This condition translates into $\omega_C \tau \approx 1$. The cyclotron frequency is given by (2.18) as $\omega_C = \frac{2\pi}{T} = \frac{eBv_F}{\hbar\sqrt{\pi n}}$, so we get

$$\tau \approx \frac{1}{\omega_C} = \frac{\hbar\sqrt{\pi n_{\text{SdH}}}}{e v_F B_{\text{SdH}}}. \quad (4.15)$$

In the data shown in 4.25, the oscillations in the conductance start to emerge at a field of $B_{\text{SdH}} \approx 400$ mT and a charge carrier density of $n_{\text{SdH}} \approx 2 \times 10^{11} \text{ cm}^{-2}$, which translates into $\tau \approx 1.3 \times 10^{-13}$ s and $2\pi r_C = 2\pi \frac{\hbar\sqrt{\pi n_{\text{SdH}}}}{eB} \approx 820$ nm. τ can be seen as a measure of sample quality, but it is not equivalent to transport scattering times. For suspended graphene, Bolotin et al. found $\tau = 2 \times 10^{-13}$ s [Bol08].

4.3.2 Edge Mode Mixing

In the previous section, the sample was investigated in the unipolar regime, where the conductance at integer filling factor is defined by $\nu = \frac{nh}{eB}$. Using the local top gate, the charge carrier density can be adjusted separately in either half of the sample. And like the direction of the skipping orbit trajectories in section 4.2.4, the direction of edge modes in the quantum Hall regime can be inverted by electrostatic gating, while keeping B constant. As shown in figure 4.26, this leads to a qualitative difference in the conduction mechanism for the unipolar and bipolar regimes. In the unipolar case, with filling factors ν_1, ν_2 of the same sign, the conductance is ballistic and limited by the number of edge modes that travel along the entire sample, i.e.

$$G = \min(|\nu_1|, |\nu_2|) \frac{e^2}{h} \quad (4.16)$$

On the other hand, in the bipolar regime, no channels are directly connecting the contacts, and the conduction happens only due to disorder induced equilibration of the edge modes along the p-n interface. At the end of the p-n interface, the charge carriers are distributed into the available channels in either direction with equal probability, and the sample conductance is given by the simple ohmic sum of the resistance of either side,

$$R = R_{\nu_1} + R_{\nu_2} \Rightarrow G = \left(\frac{1}{|\nu_1|} + \frac{1}{|\nu_2|} \right)^{-1} \frac{e^2}{h} = \frac{|\nu_1||\nu_2|}{|\nu_1| + |\nu_2|} \frac{e^2}{h}. \quad (4.17)$$

These relations were found by D. A. Abanin et al. [Aba07], describing the experimental data of J. R. Williams et al. [Wil07] in a graphene sample on SiO₂.

The edge mode mixing relies on disorder and depends on the spatial separation of the edge modes at the p-n interface, but the exact mechanism is a matter of debate [Low09]. So far, most experimental data was measured in samples on SiO₂, typically with additional oxide or PMMA layers as top gate dielectric [Wil07][Mat15], using chemical doping [Loh09] or by introducing doping and disorder by scratching the graphene with an AFM tip [Sch13]. While the data of these disordered samples could mostly be explained by full edge mode mixing, more recent experiments on cleaner samples show deviations that are explained by incomplete mode mixing. Amet et al. [Ame14] investigated a graphene p-n-p junction on hBN with a suspended top gate, and found the mixing dependent on spin polarization of the edge modes. [Kli15] found very clear mixing of only the lowest Landau level in a multi terminal Hall bar sample on specially

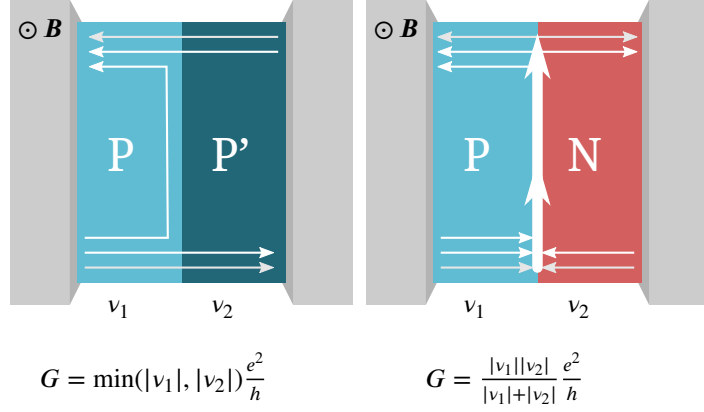


Fig. 4.26: Edge modes along a graphene p-n interface in the quantum Hall regime. **Left:** Independent modes, ballistic transport. **Right:** Full equilibration

prepared atomically smooth SiO₂ with buried split back gates. In this case, only the number of modes participating in the equilibration contribute to (4.17). In a very recent study by Kumada et al. [Kum15], shot noise measurements were performed, showing that the mode mixing is indeed quasi-elastic in short junctions and can be used as an electronic beam splitter. A review of experiments and theory can be found in [Mac15].

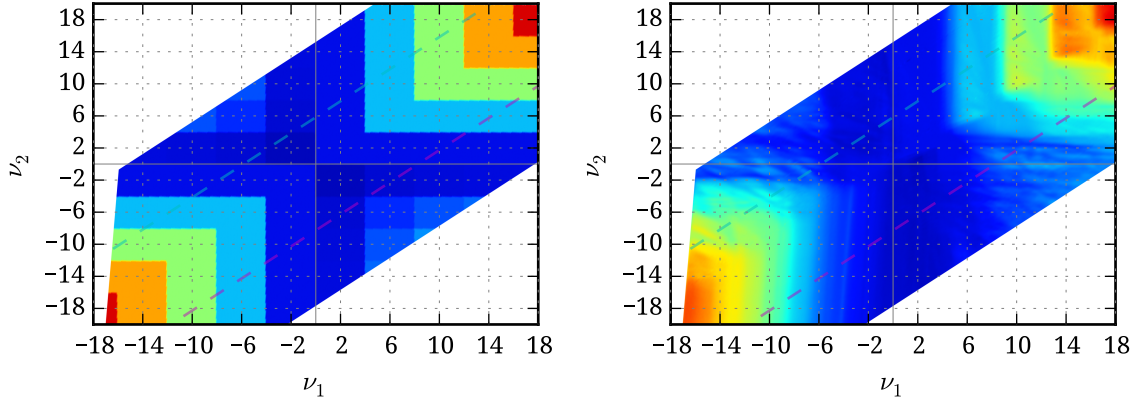


Figure 4.27: Conductance of p-n junction in quantum Hall regime. **Left:** Calculation for full mode mixing according to (4.17). **Right:** Measured dI/dV . The color scales are equal, the conductance in the calculated data for unipolar doping can serve as a reference

Figure 4.27 shows the theoretical conductance for full equilibration and the measured data at 4.2 K and 4 T. The filling factor was calculated as $\nu = \frac{nh}{eB}$, with charge carrier densities calculated using the gate efficiencies $\alpha_{BG, TG}$ that were derived in the previous section. The charge neutrality point was adjusted to $V_{BG} = -1.2$ V, $V_{TG} = -0.49$ V to align the position of the pattern with respect to the indicated filling factors. Filling factor ν_1 corresponds to the region without topgate, and ν_2 respectively corresponds to the top gated region. The measured data matches the expectation in the regions of unipolar doping ($\nu_1 \nu_2 > 0$). The plateaus for electron doping ($\nu_1, \nu_2 > 0$, top right) are well defined except for $\nu_2 = 2$, whereas the plateaus for hole conduction ($\nu_1, \nu_2 < 0$, bottom left) are smeared out, as already observed in the Shubnikov-de Haas oscillation pattern at $V_{TG} = 0$ V.

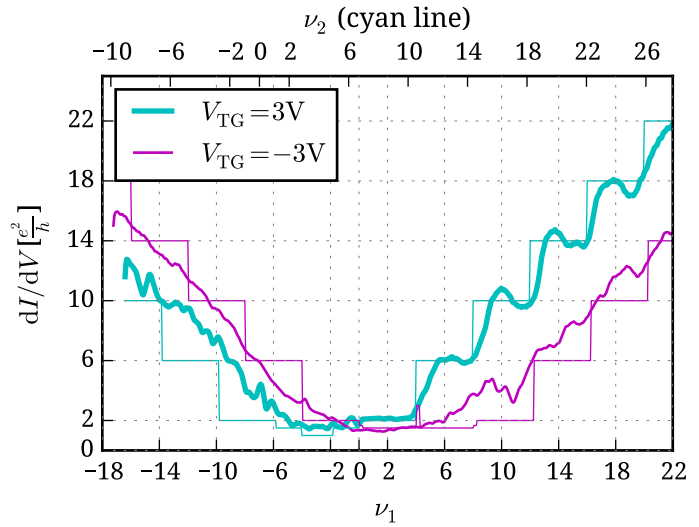


Fig. 4.28: Plot of conductance dI/dV along the cyan and magenta lines in figure 4.27, measured at 4 T for constant V_{TG} (same data as the color map). The thin lines show the calculation assuming full equilibration.

Due to the lower conductance, the behavior in the bipolar regions is better visible in figure

4.29, where the color scale shows the differential resistance dV/dI . Here, the plateaus are not as well defined as in the unipolar electron doped region, and they show additional structure. Nevertheless, a clear, qualitative deviation of the data compared to the behavior expected for full mode mixing can be seen. The plot shows an unexpected asymmetry with respect to either diagonal, i.e. different behavior for p-n and n-p doping, and different behavior in terms of switching $\nu_1 \leftrightarrow -\nu_2$.

In the p-n region ($\nu_1 < 0$, $\nu_2 > 0$), the overall resistance is lower than expected. Nevertheless, signs of the plateaus are visible. In the n-p region ($\nu_1 < 0$, $\nu_2 > 0$), the conductance for the single edge mode $\nu_1 = 2$ is independent of ν_2 , leading to the vertical red line. This can be interpreted by assuming that only the first (and maybe the second) mode of ν_2 take part in the equilibration, while further increase of ν_2 only adds modes that don't contribute to the conductance, as shown in the bottom right figure of 4.29. The resulting conductance, assuming only mixing of the first two modes $\nu_2^{\text{mix}} = 6$, is given by

$$G(\nu_1 = 2) = \frac{\nu_1 \nu_2^{\text{mix}}}{\nu_1 + \nu_2^{\text{mix}}} \frac{e^2}{h} = \frac{2 \cdot 6}{2 + 6} \frac{e^2}{h} = \frac{3}{2} \frac{e^2}{h}, \quad (4.18)$$

which corresponds to $R \approx 17.2 \text{ k}\Omega$ and is in agreement with the data, as shown in the top figure of 4.30, where the resistance is plotted along the magenta dashed line in figure 4.29.

Both the color map 4.29 and the plot of resistance along the magenta line 4.30 show deviation from the theoretical expectation even in the unipolar regime for $|\nu_2| = 2$, where the measured conductance is higher than expected (in the color plot 4.29, compared to theory, the green horizontal lines are missing). Only starting at the second mode $\nu_2 = 10$, it starts aligning with the calculation, as visible in the plot of conductance, 4.28.

On the other hand, when increasing the number of modes ν_1 in the n-p region, the conductance drops, and for example $G(\nu_1 = 10, \nu_2 = -2) \gg G(\nu_1 = 2, \nu_2 = -10)$.

In addition to the explanation of the fractional conductance plateaus in the bipolar regime, D. A. Abanin et al. proposed that the partitioning at the end of the p-n interface should lead to shot noise, described by a Fano factor of

$$\mathcal{F} = \frac{|\nu_1| |\nu_2|}{(|\nu_1| + |\nu_2|)^2}, \quad (4.19)$$

for full mixing, while the dissipation free conduction in the unipolar regime should be noiseless. The measurement of shot noise thus can serve as a tool to investigate this qualitative change in the conductance mechanism, which is not as obvious from the conductance data, and it would help understanding edge mode mixing. At the time of the measurements presented here, this prediction had not yet been confirmed, but in the very recent publication by Matsuo et al. [Mat15], the expected result for full mode mixing was found in a disordered sample on SiO_2 .

Measuring shot noise requires sweeping the DC bias V_{DS} , so the data was recorded in a separate measurement and at a field of $B = 5 \text{ T}$. Sweeps of V_{DS} were recorded for each point along the magenta line in 4.29, the green line in fig. 4.30 is a slice of the data at $V_{\text{DS}} = 0$. Figure 4.31 shows the resulting plots for resistance and differential Fano factor (3.15) $F_d(V_{\text{DS}}) = \left| \frac{1}{2e} \frac{dS_I}{dI} \right|$, normalized with the maximum value of $F_d^{\text{max}} = 0.008$ and calculated using $\text{GBW} = 3.16 \times 10^{18} \text{ Hz}$

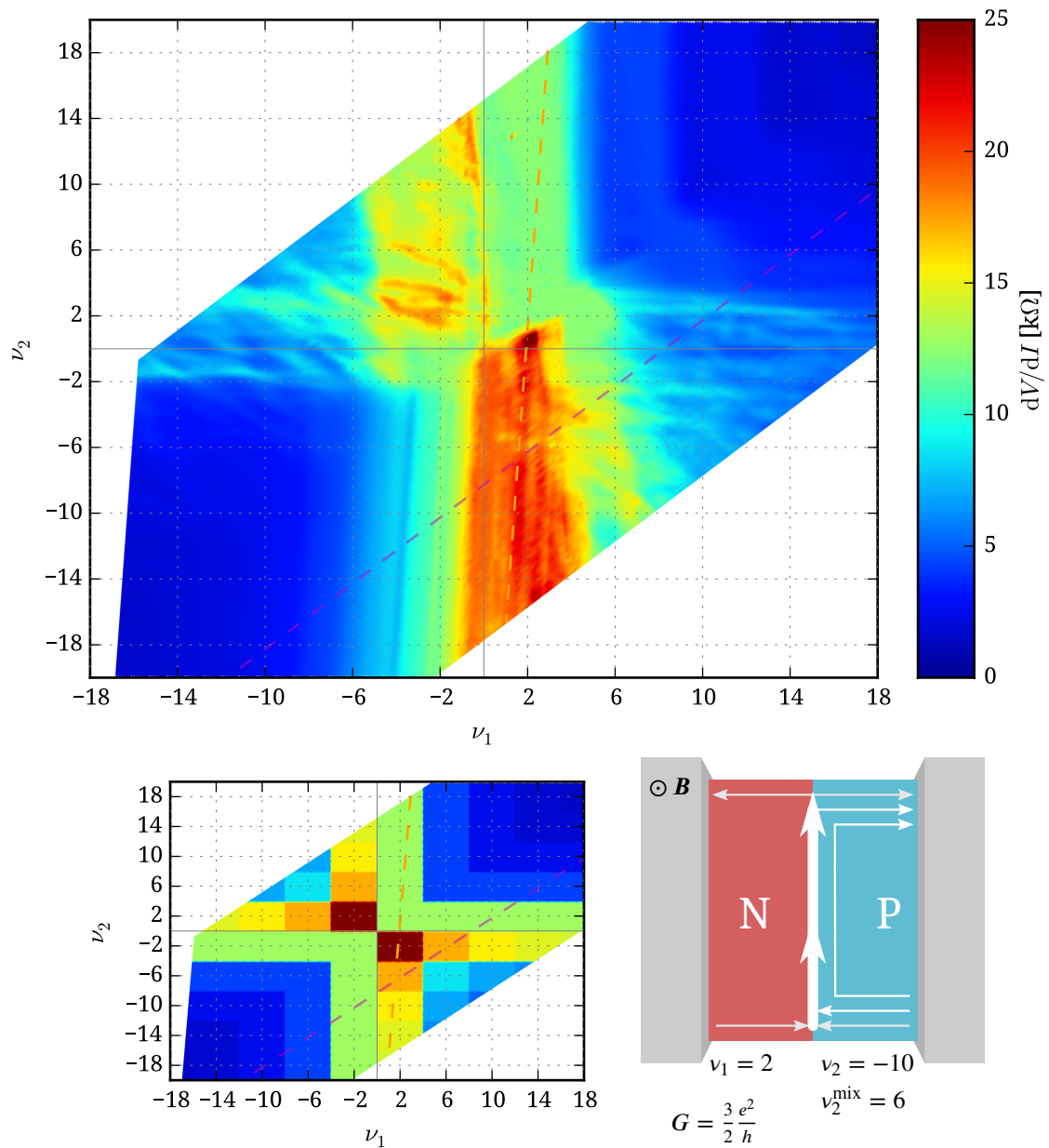


Figure 4.29: Partial equilibration of quantum Hall edge modes. **Top:** Measured dV/dI of the p-n junction in quantum Hall regime. **Bottom left:** Calculated resistance for full equilibration. The color scale is the same. **Bottom right:** Schematic image of partial equilibration.

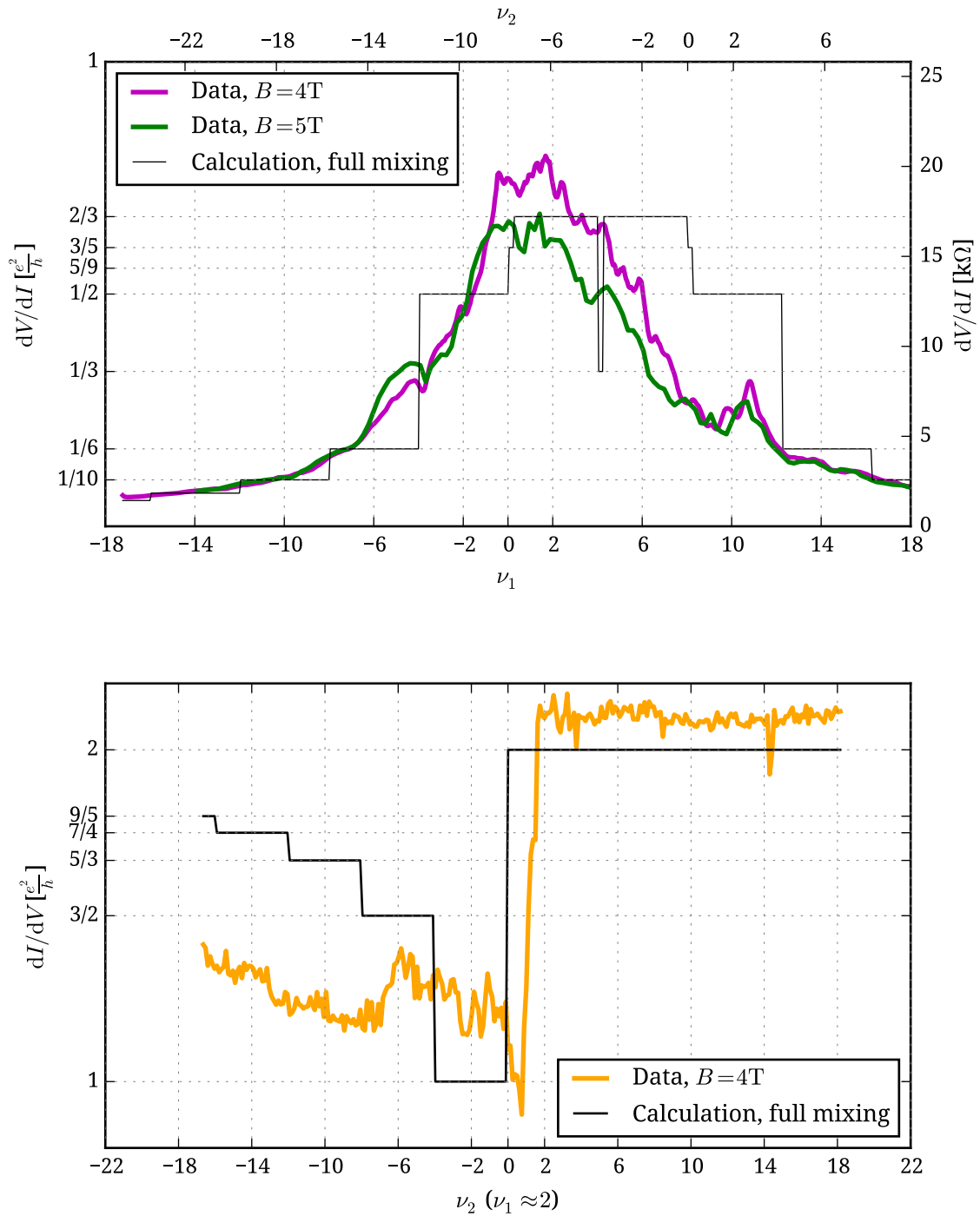


Figure 4.30: Slices of 4.29. **Top:** Plots of resistance dV/dI along the magenta line in figure 4.29, measured at 4 T (same data as the color map) and 5 T (same data as noise measurement). **Bottom:** Plot of the conductance dI/dV along the orange line, where $\nu_1 \approx 2$. The black lines shows the calculation assuming full equilibration.

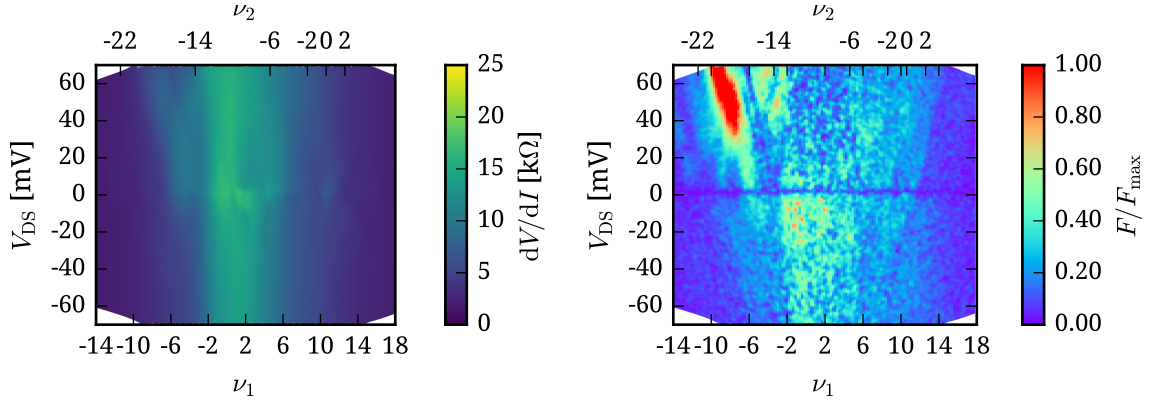


Figure 4.31: Bias sweeps along the magenta line in 4.29. **Left:** Resistance. **Right:** Differential Fano Factor as defined in 3.15, normalized with the maximum value of $F_d^{\max} = 0.008$

from a previous cool down.

Independent of the calibration, the expectation of a finite Fano factor in the bipolar regime (given by (4.19)), and noiseless conduction in the unipolar regime should be visible in the data. Although the overall noise level is very low, two features can be seen in the plot of F_d . First, at filling factor $\nu_1 = -6$, a sharp peak appears for high positive bias of about 40 mV. The peak in the differential noise corresponds to a peak in the resistance that is visible for $\nu = -6$ in 4.30.

At positive $\nu_1 \approx 12$ and zero bias, a sharp drop of the noise is observed, when the conductance shown in figure 4.30 starts aligning with the expectation for the unipolar regime. This could indicate that the first edge mode $\nu_2 = 2$ of the top gated area is not fully ballistic.

4.4 Proximity Induced Superconductivity

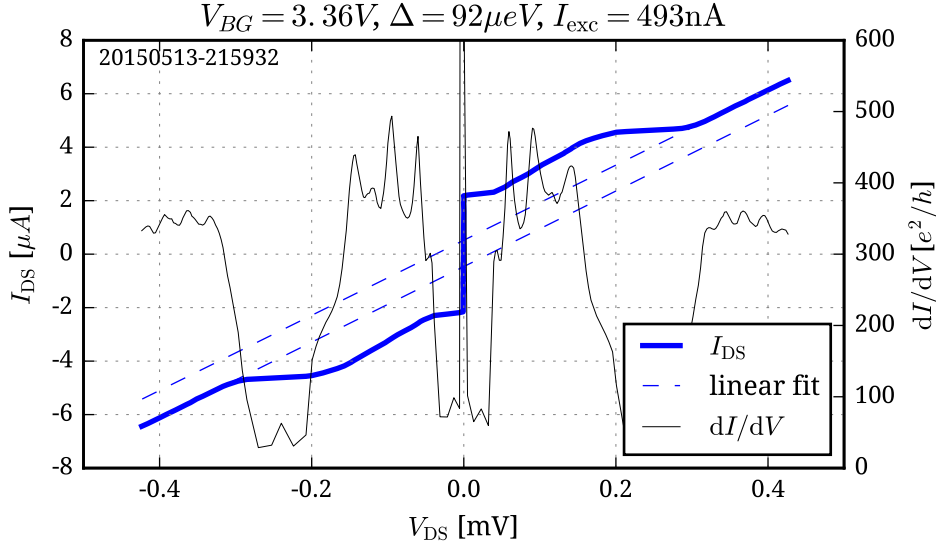


Figure 4.32: IV characteristic of sample A at $T_{MC} = 15$ mK, $B = 0$ T.

At very low temperature and field, the Ti/Al contact leads turn superconducting and supercurrent can be transmitted via Andreev bound states if the current is below the critical current I_C , as described in 2.2. Figure 4.32 shows the IV characteristic of sample A at 15 mK at $B = 0$ T, together with the differential resistance. Multiple features that will be investigated in the following chapter can be identified. Most prominently, up to a current I_C , there is not voltage drop, and the sample is superconducting. Outside of the superconducting region, multiple steps in the current can be observed, that show as peaks in the differential conductance. These peaks are caused by multiple Andreev reflection, and will be investigated in section 4.4.3. At a bias of $V_{DS} = 2\Delta e$, direct transmission of quasiparticles starts being possible. Extrapolating the lines back to zero bias, one can find the excess current I_{exc} , which originates from MAR processes. The big dips in the differential conductance above 2Δ are most likely caused by effects in the electrodes.

Graphene Josephson junctions were first investigated by Heersche et al. [Hee07]. They are especially interesting due to the effect of *specular* Andreev reflection. [Bee08] The observation of these effects requires transport of Josephson current in the ballistic regime [Du08], which has first been reached recently in hBN encapsulated graphene [Cal15][Miz13].

4.4.1 Gate and Temperature Dependence of the Critical Current

The features identified in the IV curve depend on the charge carrier density. Figure 4.33 shows the differential resistance with respect to the current I_{DS} and the gate voltage V_{BG} , so every vertical line corresponds to a bias sweep as shown in figure 4.32. In the plot against current, I_C can be clearly identified as an area of zero resistance, with a height equal to $2I_C$. The conductance dips at high bias turn into sharp peaks in the differential resistance when plotted versus current. I_C was extracted by detecting the position of the peaks in the differential resistance and setting

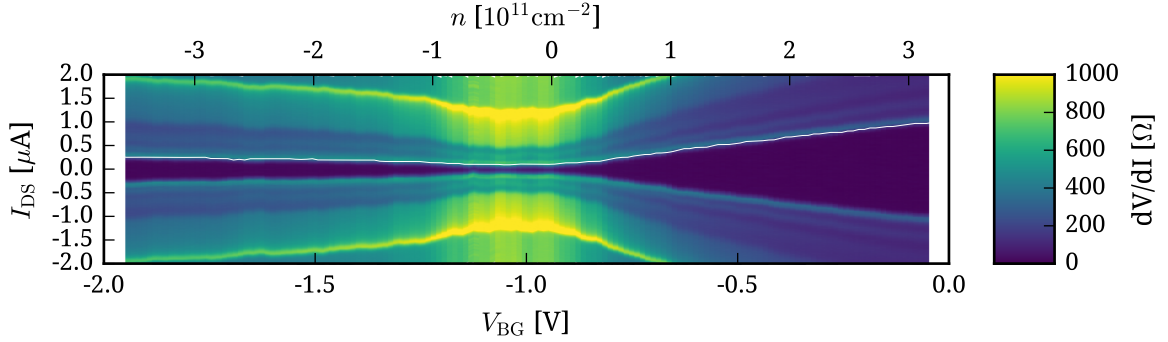


Figure 4.33: Gate dependence of the differential resistance of sample A at $T = 15$ mK, white line indicates extracted I_C

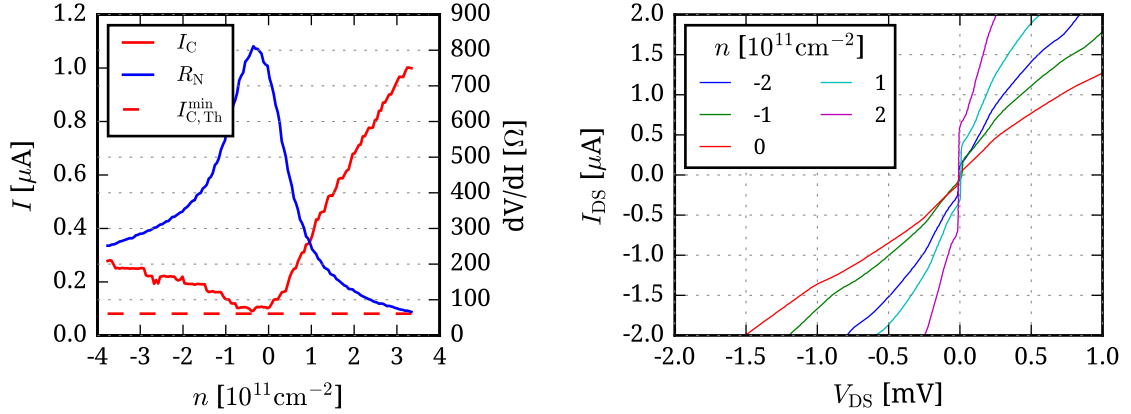


Figure 4.34: Left: Critical current I_C extracted from the data shown in fig. 4.33 and resistance in normal state (with $B = 20$ mT). Right: Selected IVs at low charge carrier density

a threshold at half of their height. The resulting I_C are shown in figure 4.34. Due to reduced transmission because of the contact doping, the supercurrent for hole conduction is smaller than for electron conduction. The maximal critical current of $I_C^{\max} = 2.38 \mu A$ was measured at $n = 1.8 \times 10^{12} \text{ cm}^{-1}$ (not shown). In this sample, a finite supercurrent of $I_C^{\min} = 91 \text{ nA}$ remains even at the Dirac point.

In the short junction limit $W \ll L, \xi$, at low density $n = 0$, Titov et al. predict a critical current of [Tit06]

$$I_{C,Th}^{\min} \approx 1.33 \frac{e\Delta_0}{\hbar} \frac{W}{\pi L} \quad \text{and} \quad I_{C,Th} \approx 1.22 \frac{e\Delta_0}{\hbar} \frac{E_F W}{\pi \hbar v_F} \quad \text{for} \quad E_F \gg \hbar v_F/L. \quad (4.20)$$

Using $\Delta_0 = 92 \mu eV$ for sample A, found from the position of MAR peaks, the coherence length $\xi = \frac{\hbar v_F}{\Delta_0} \approx 7 \mu m$ is much larger than $L = 350 \text{ nm}$, and $I_{C,Th}^{\min} = 81 \text{ nA}$, close to the measured value.

The critical current and the resistance in normal state are related, and in theory given by a universal value of $I_C R_N = 2.08 \frac{\Delta}{e}$ at the Dirac point with $E_F \ll \frac{\hbar v_F}{L}$, and $I_C R_N = 2.44 \frac{\Delta}{e}$ at higher energies [Tit06]. Figure 4.35 shows the measured $I_C R_N$ product.

Figure 4.36 shows the gate dependence of I_C in the dual-gated sample B. No supercurrent

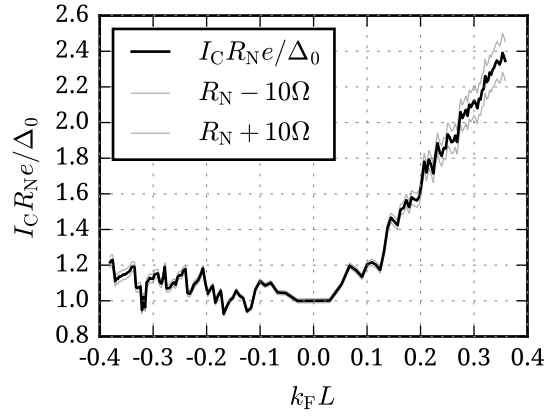


Figure 4.35: $I_C R_N$ of sample A. Resistance in normal state was measured at $B = 20$ mT

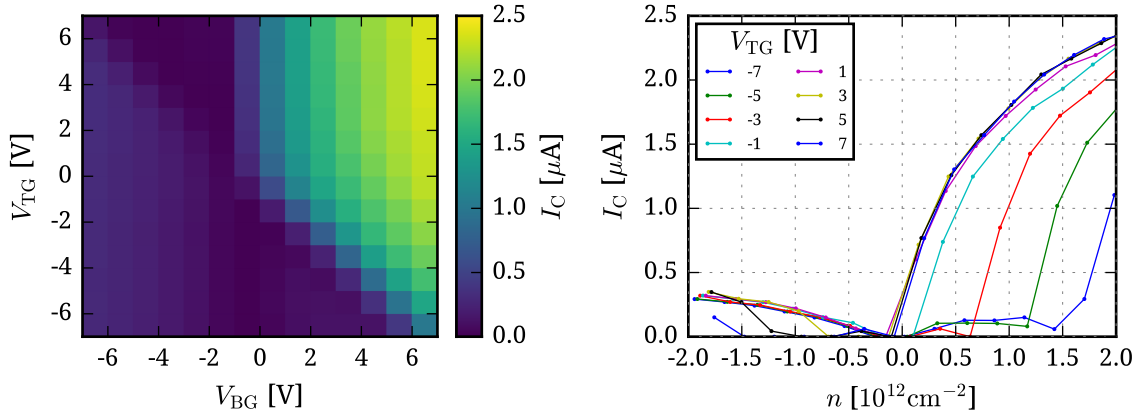


Figure 4.36: **Left:** Top gate and back gate dependence of critical current I_C for the p-n junction (sample B). **Right:** Slices at constant V_{TG}

was observed in the bipolar p-n region. In the n-p region only a small supercurrent up to $I_C^{NP} = 128$ nA was measured, the maximum for hole doping was $I_C^{PP} = 310$ nA, and the overall maximum measured at $V_{BG} = V_{TG} = 7$ V was $I_C^{nn} = 2.25$ μ A.

The temperature dependence of I_C and $I_C R_N$ in sample B are shown in figure 4.37. The normal state resistance R_N was taken from the gate map at 4 K 4.11.

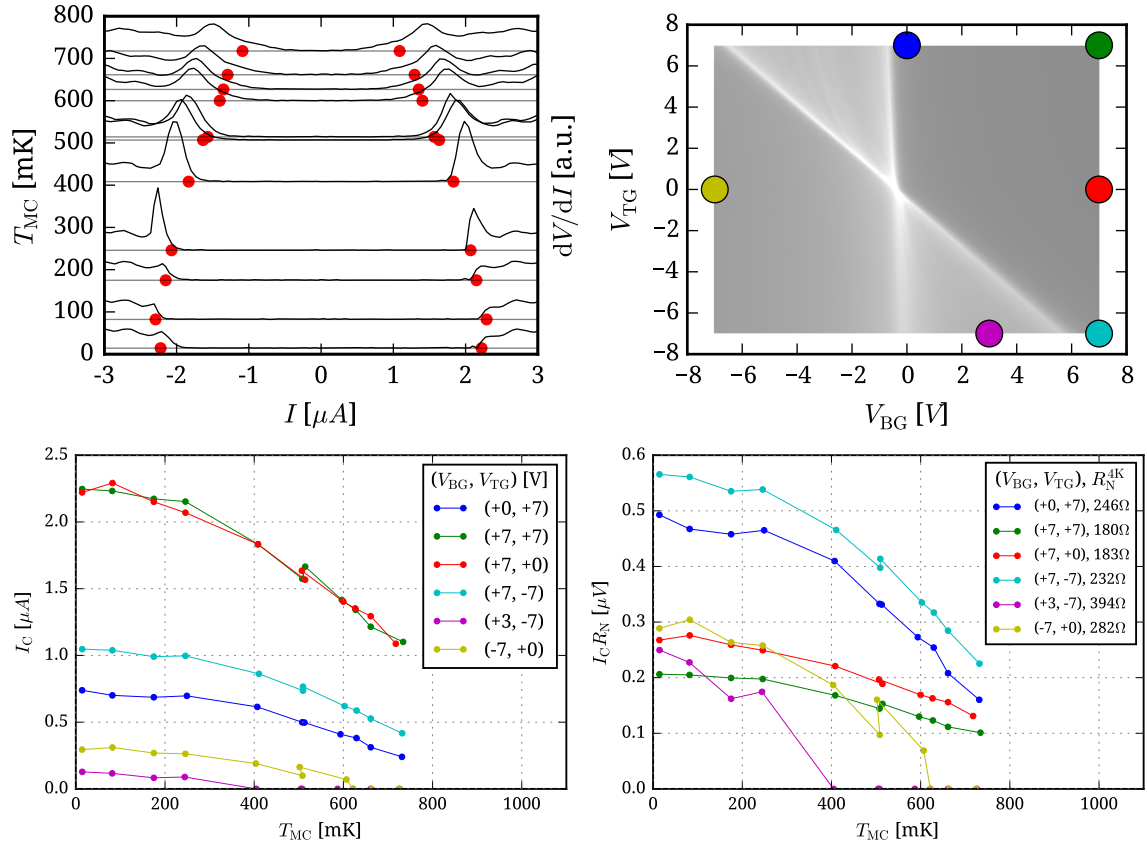


Figure 4.37: Temperature dependence. **Top Left:** Automatic extraction of I_C for $V_{BG} = 7$ V, $V_{TG} = 0$ V using a threshold in dV/dI of 20. The plot shows $\pm I_C$ as red dots and the respective dV/dI curve in arbitrary (but common) units at each temperature. **Bottom:** I_C and $I_C R_N$ in sample B plotted versus mixing chamber temperature T_{MC} for various gate voltages, indicated by the dots of same color as in the gate map.

4.4.2 Current Distribution Analysis

When applying a perpendicular magnetic field B_{\perp} , a position dependent phase difference

$$\delta\varphi(x) = \frac{2\pi}{\Phi_0} B_z (L + 2\lambda_B)x \quad (4.21)$$

between the macroscopic wave functions of the superconducting leads is introduced, where x is the coordinate across the width of the junction, B_z is the perpendicularly applied field, L is the length, and λ_B is an additional effective length due to the Meissner effect in the leads. From the current-phase relation, this causes an oscillating supercurrent density $J_s(x) = J_C(x) \sin\left(2\pi\frac{B_z}{\Phi_0}(L + 2\lambda_B)x + \varphi_0\right)$ with respect x , and a characteristic oscillation pattern of the total critical current versus the applied field $I_C(B)$, which is associated with the real space distribution of the Josephson current across the junction[Dyn71]. The total critical current is given by the integral of the local maximum current density $J_C(x)$

$$I_C(B) = \left| \int_{-W/2}^{W/2} J_C(x) e^{2\pi i \frac{B_z}{\Phi_0} L_B x} dx \right| \quad (4.22)$$

with the flux quantum $\Phi_0 = \frac{h}{2e}$, width of the junction W and an effective length $L_B = L + 2\lambda_B$. This integral is equal to the amplitude of a complex Fourier transformation of the real space current distribution and can be used as a tool to probe it [Dyn71][Har14][All15]. For a homogeneous $J_C(x)$, the interference pattern takes the shape of the Fraunhofer pattern

$$I_C(B) = I_C^0 \left| \frac{\sin \pi \frac{\Phi}{\Phi_0}}{\pi \frac{\Phi}{\Phi_0}} \right|, \quad (4.23)$$

equivalent to the interference pattern of waves passing a single slit.

Figure 4.38 shows this interference pattern as a color map of the $\frac{dV}{dI}$, measured on sample A at $V_{BG} = 4$ V, at $n = 1.8 \times 10^{12} \text{ cm}^{-2}$. The red line is a fit of 4.23 to the extracted critical current $I_C(B)$, which is shown as black crosses. The fit perfectly describes the observed pattern, proving completely homogeneous current distribution. The fit parameters are the critical current $I_C = 2.38 \mu\text{A}$ and the junction area $A_B = 2.53 \mu\text{m}^2$, which results in an effective length $L_{\text{eff}} \frac{W}{A_B} = 842 \text{ nm}$.

Since the measured value can only represent the magnitude of the Fourier transformed current distribution, and phase information is lost, the imaginary part has to be recovered [Dyn71]. A simplification can be made by assuming a symmetric current distribution, in which case

$$I_C(B) = \left| \int_{-W/2}^{W/2} J_C(x) \cos\left(\frac{2\pi}{\Phi_0} L_B B x\right) dx \right|. \quad (4.24)$$

A corresponding current profile is shown in figure 4.39.

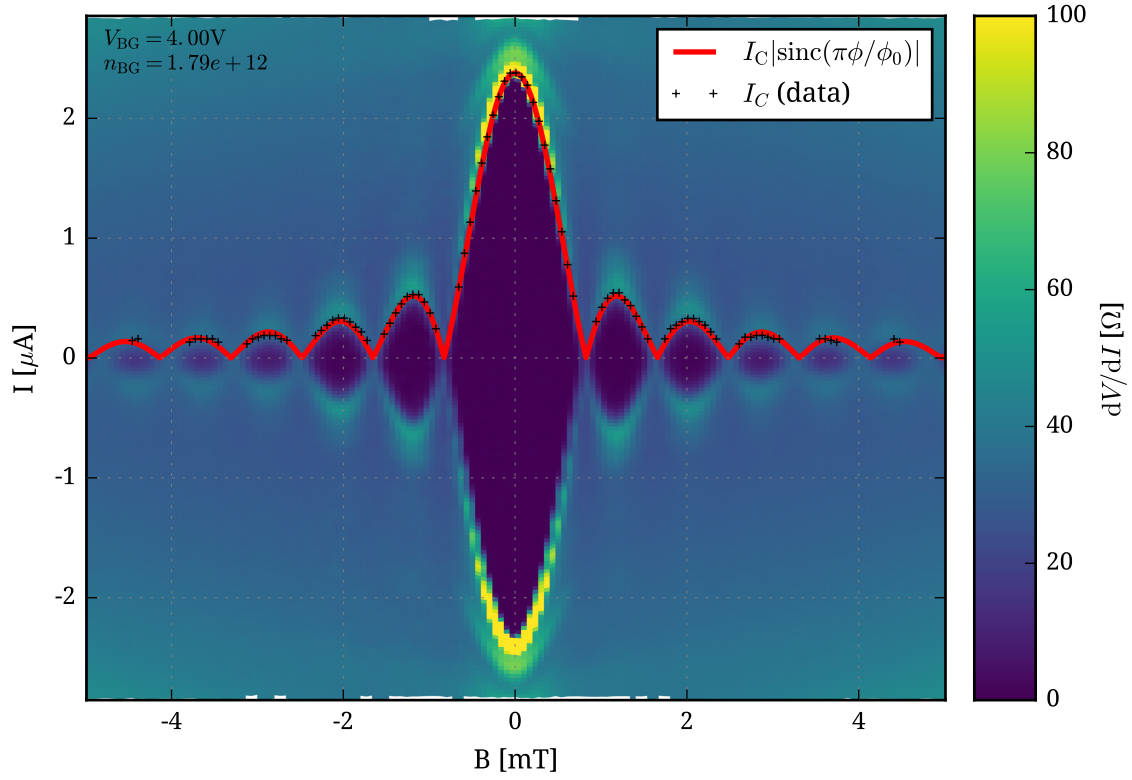


Figure 4.38: Field dependence of the critical current in sample A at $V_{\text{BG}} = 4\text{V}$

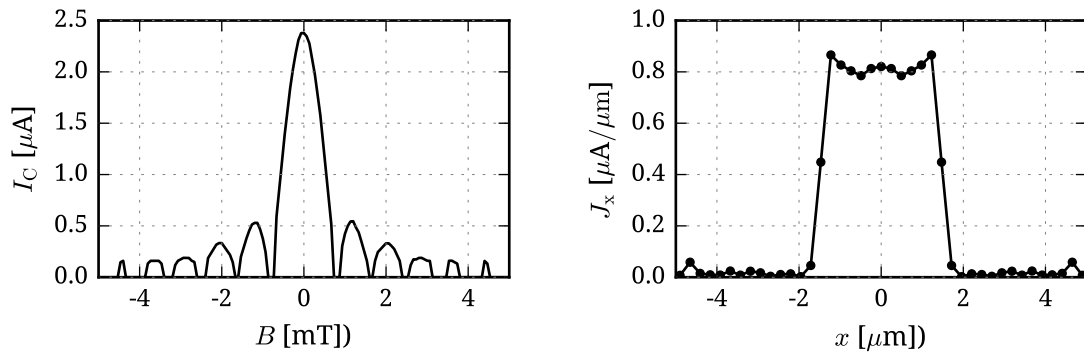


Figure 4.39: Extracted critical current from 4.38 and Fourier transformation, revealing the real space current distribution

4.4.3 Multiple Andreev Reflection

When the current is increased beyond the critical current I_C , oscillations in the conductance at characteristic bias voltages given by integer fractions of $V_{DS} = \frac{2\Delta_0}{N}$ can be observed. These oscillations can be understood from the MAR process explained in 2.2, where quasiparticles that cannot be directly transmitted due to the superconducting gap Δ in the leads can successively gain energy by reflecting back and forth within the junction until they can reach the quasiparticle continuum. From the position of the MAR peaks in the differential conductance, we can estimate Δ_0 , as was done in the left panel of fig. 4.40 for sample A, where $\Delta_0 \approx 92 \mu\text{eV}$ was found. While the peaks at Δ_0 , $2\Delta_0/3$ can be clearly identified, the peak at $2\Delta_0$ is obscured by the conductance dip. For pure Al films, a gap of $\Delta_{\text{Al}} = 200 \mu\text{eV}$ to $300 \mu\text{eV}$ was reported for thin films[Cou08], while $\Delta_{\text{Al}}^{\text{bulk}} = 180 \mu\text{eV}$ for bulk aluminium[Gro14]. In the samples presented here, a Ti adhesion layer was used, which lowers Δ_0 . The right panel of figure 4.40 shows a gate and bias sweep, where each vertical slice corresponds to a measurement as shown on the left. In this representation versus the bias voltage V_{DS} , the gate independent, energy dependent position of the MAR peaks becomes apparent.

In sample B, the oscillations in the conductance are even more pronounced for electron conduction, while only very weak features are visible for hole conduction, as shown in the left panel of figure 4.41. Here, peaks at $2\Delta_0$, Δ_0 and $\frac{2}{3}\Delta_0$ can be identified, with $\Delta_0 \approx 115 \mu\text{eV}$. The additional peak at lower bias is not aligned with $\frac{1}{2}\Delta_0$ as expected, but located closer to $\frac{2}{5}\Delta_0$. The difference in the amplitude of the MAR signal for hole and electron conduction is also reflected in the excess current, which is caused by the contribution of MAR to the current at high bias. It is much larger for electron conduction, as shown in the right panel of 4.41. The very large amplitude of MAR in both samples indicates a high transmission [Pos94].

Since the MAR are an indicator for the value of Δ_0 , it is interesting to study the temperature dependence, as shown in figure 4.43 for sample B. The positions remain relatively stable up to about 500 mK, where both Δ and the MAR amplitude start to decline. Figure 4.44 shows the positions of the MAR peaks divided by $N = \frac{2}{3}, 1, 2$, i.e. the value of Δ_0 corresponding to each peak position, versus the temperature.

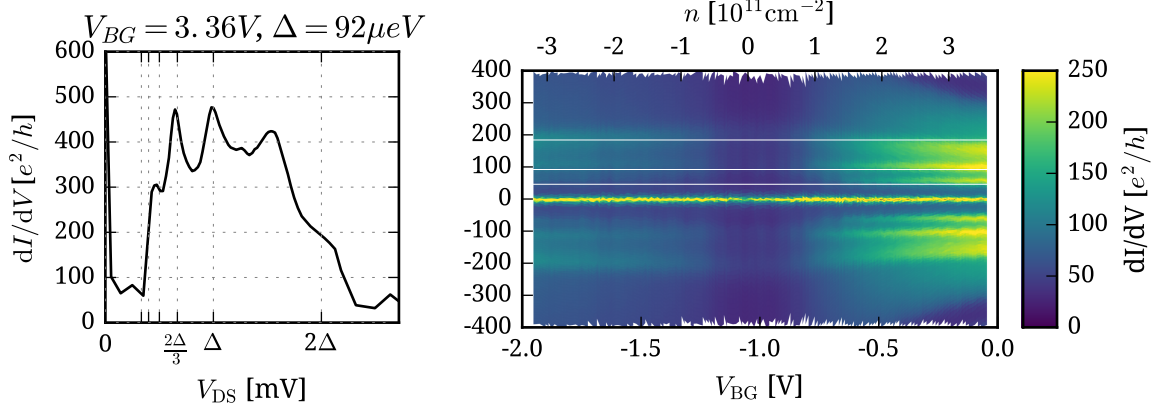


Figure 4.40: Multiple Andreev Reflection in sample A, $T = 15$ mK. **Left:** At $V_{BG} = 3.36$ V, with $\Delta_0 = 92 \mu\text{eV}$. **Right:** Double sweep of bias and gate voltage at low charge carrier density

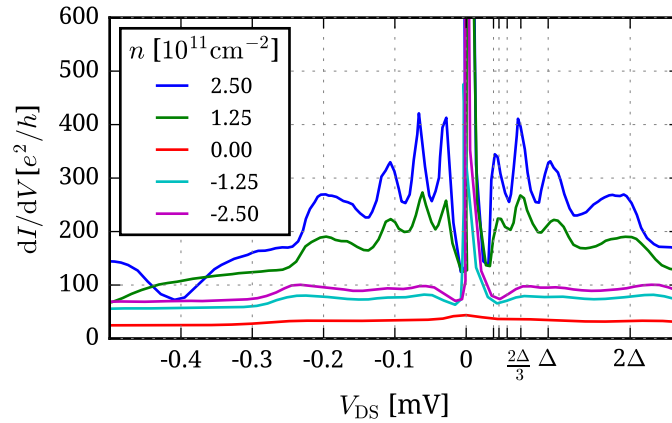


Figure 4.41: Multiple Andreev Reflection in sample B for various charge carrier densities at $V_{TG} = 0$, $T = 14$ mK, with $\Delta_0 = 115 \mu\text{eV}$

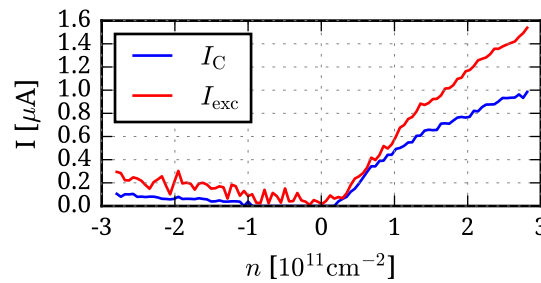


Figure 4.42: Critical current and excess current corresponding to the data shown in 4.41

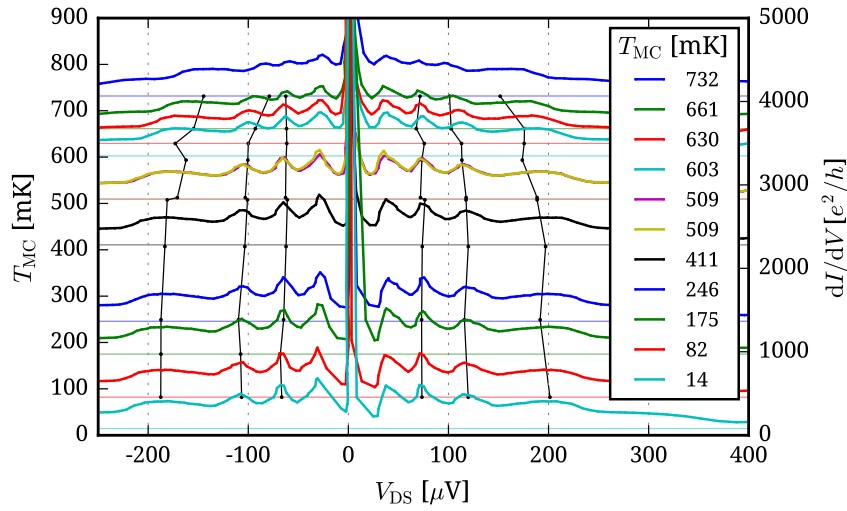


Figure 4.43: Temperature dependence of MAR. The horizontal lines indicate the baselines for each conductance curve with the same color. They are shifted such that the position of each baseline indicates the measurement temperature. The black lines show the positions of MAR peaks at 2Δ , Δ , and $\Delta/2$.

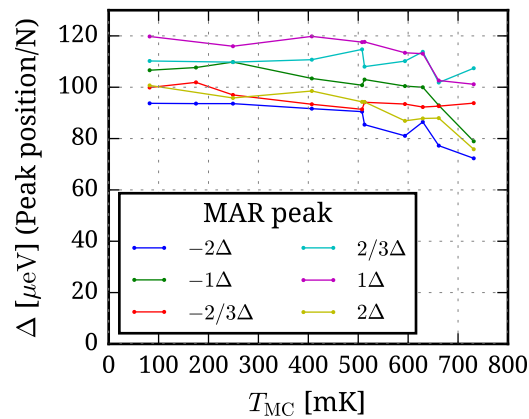


Figure 4.44: Temperature dependence of Δ_0 , extracted by dividing V_{DS} of the MAR positions in 4.43 by $N = \frac{2}{3}, 1, 2$.

Shot Noise of Multiple Andreev Reflection

While no previous experimental work on shot noise of MAR in graphene exists, enhanced noise due to the increased effective charge quanta $q_{\text{eff}} \approx (1 + \frac{2\Delta_0}{eV})e$ that are coherently transferred by each MAR process was observed in metallic systems. [Die97] investigated NbN/MgO/NbN superconductor-insulator-superconductor (SIS) tunnel junctions. The shot noise was found to be enhanced by MAR in pinholes in the oxide barrier, where the transmission of these pinholes is estimated as $T \approx 0.17$. [Hos00] found MAR enhanced shot noise in diffusive Al wires, and [Cro01] in atomic point contacts (break junctions) with varying transmission probabilities. The enhanced shot noise agrees with theoretical predictions [Ave96; Bez99; Cue99a; Nav99]. Additionally to these experimental studies performed on systems with relatively low transparency, [Cam05] found MAR enhanced shot noise in a ballistic 2DEG, with $\mu = 3.5 \times 10^5 \text{ V s cm}^{-2}$, $n = 6.6 \times 10^{11} \text{ cm}^{-1}$, and a corresponding mean free path of $l_{\text{mfp}} = 4.6 \mu\text{m}$.

In contrast to previous experiments and theory, the raw data of our shot noise measurements shows a clear suppression of the noise at the positions of MAR resonance. The suppression could be qualitatively reproduced in a theoretical model by Ulf Briskot and Igor Gornyi, where the noise can be reduced at the resonance due to the high transparency of the device. The directly measured signal at the output of the noise detection diode, V_{Noise} , is shown in fig. 4.45 in red for sample A at $V_{\text{BG}} = -1 \text{ V}$, along with the differentially measured and integrated dV_{Noise} in blue (with integration constant set to align with the DC data). Features of suppressed noise at the MAR resonances at $2\Delta_0$ and Δ_0 are very clear in the data of the lock-in measurement, and already visible in the directly measured data.

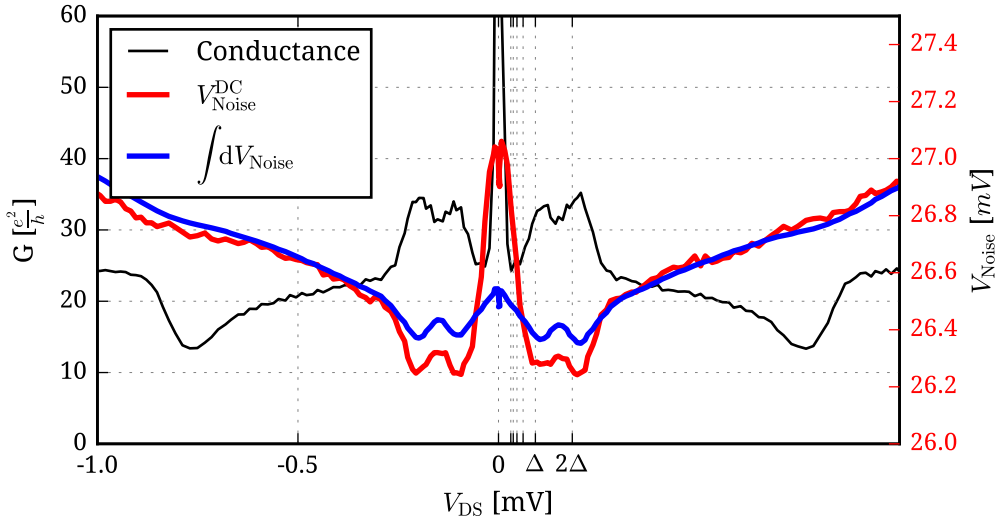


Figure 4.45: Noise measurement raw data. Conductance (black), DC measured $V_{\text{Noise}}^{\text{DC}}$ and integrated, dV_{Noise} from lock-in measurement.

The suppression is most obvious in sample A. It can be observed across the entire accessed gate range, as shown in Figure 4.46, where the differential Fano factor, calculated from (3.16), is plotted versus back gate and bias voltage around the Dirac point and at high electron density. In the data of the top gated sample B, the MAR is even more pronounced in the conductance, but less visible in the noise, as shown in fig. 4.47.

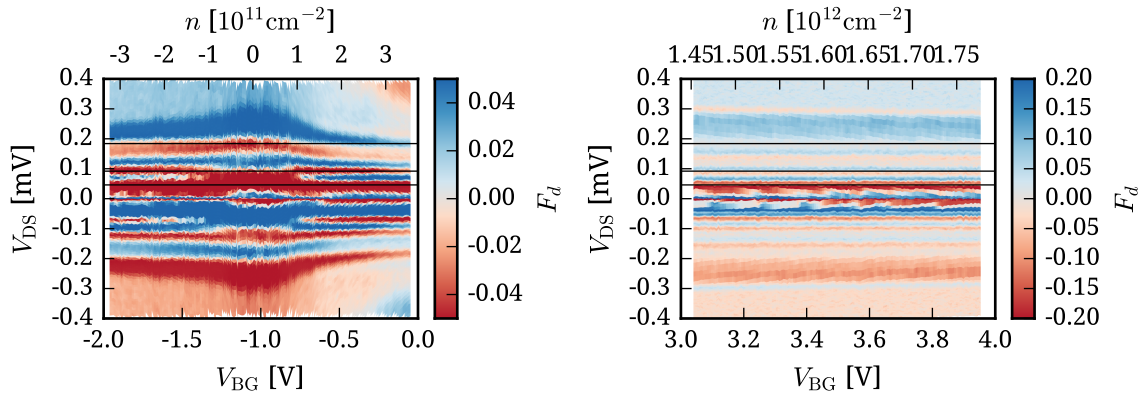


Figure 4.46: Differential Fano factor F_d of sample A at the Dirac point and at high density

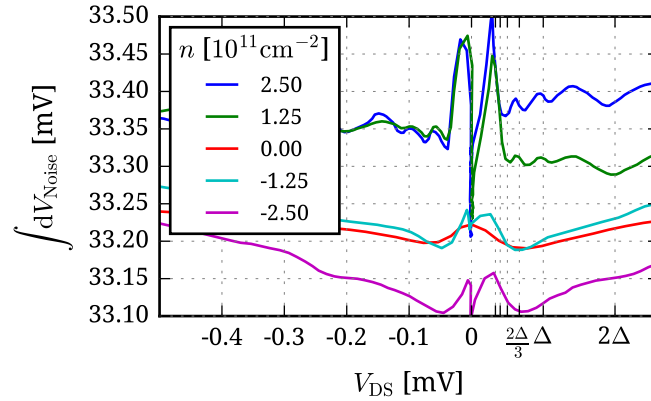


Figure 4.47: Noise signal of density dependent MAR in sample B. The plot shows the noise detector output voltage, integrated from differentially measured dV_{Noise} for the bias sweeps at $V_{\text{TG}} = 0$ shown in fig. 4.41

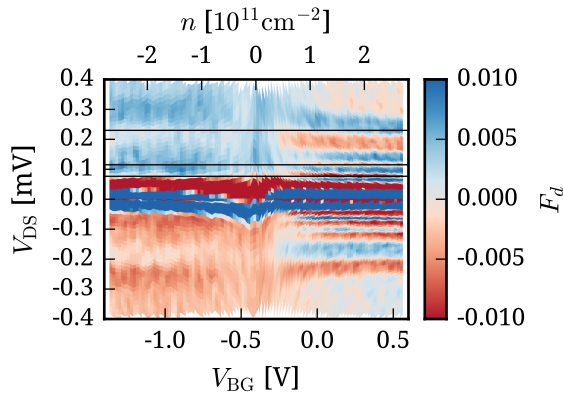


Figure 4.48: Differential Fano factor F_d of sample B at the Dirac point, with $V_{\text{TG}} = 0$

Correction of Nonlinear R_d for MAR Shot Noise

Measuring the shot noise signal of MAR is particularly challenging, since they appear only at fixed, small bias, which doesn't allow increasing the current to improve the signal, and second, because the nonlinearity in the conductance may change the coupling of the sample to the measurement setup, thereby distorting the data.

The measured voltage at the detector diode is proportional to the power at the input of the amplifier and can be converted using the gain bandwidth product GBW from a calibration measurement and the diode sensitivity α_D . Constant additional noise that is added after the first amplifier only adds a small part to the signal and can be treated together with the noise of the first amplifier. For a linear sample, the original noise $S_{I,s}$ can then be recovered according to (3.11) and (3.18).

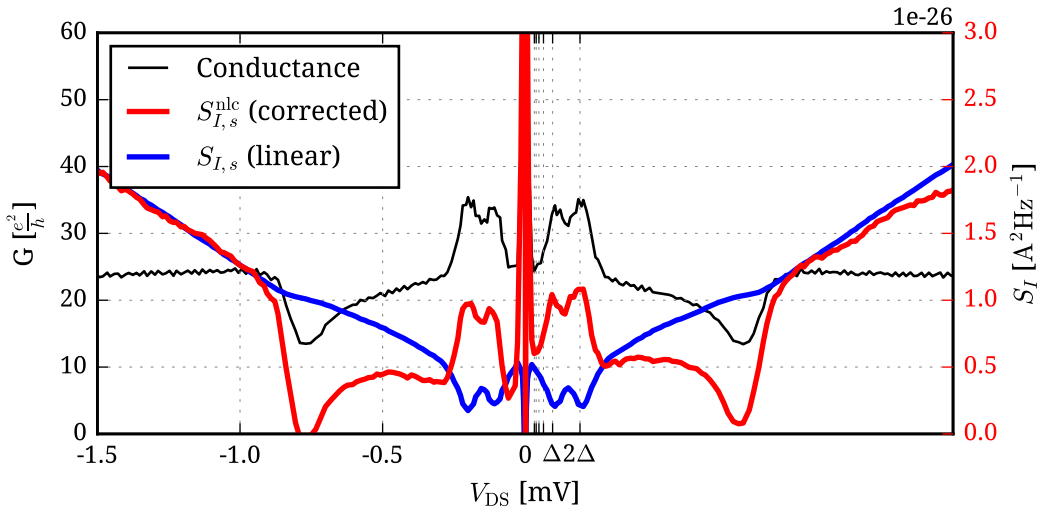


Figure 4.49: Spectral density of excess noise calculated assuming a sample with linear IV (blue) and taking into account the nonlinear corrections given by (3.23) with naive assumption $T_N = 3$ K, $T_e = 300$ mK, leading to an unphysical, overcompensated signal (red).

The correction term for samples with nonlinear IV (3.23) consists of three parts that are proportional to the noise $S_{I,s}$ itself, the shunt resistor noise temperature T_N , and the electronic temperature T_e . Finally, by integration of (3.23), the “corrected” noise $S_{I,s}^{nlc}$ is found, and depending on the parameters used for the correction, it can lower, eliminate or overcompensate the apparent noise suppression. The parameters used for the compensation shown in fig. 4.49 were an electronic temperature $T_e = 300$ mK, extracted from a fit to the low bias shot noise of the reference tunnel junction, and the actual shunt resistor temperature $T_N = 3$ K. As a third parameter, the gain bandwidth product GBW enters the equation, as it is required to find the actual power of the shot noise originating from the sample. The effect of the correction terms depends on the ratio of the power of the sample noise and the power of the spurious noise sources. By overestimating GBW, the original signal is underestimated, and the compensation terms get too big. This is the case for the data shown in figure 4.49, where the “corrected” data overcompensates the noise suppression, leading to an unphysical behavior. The most important term in (3.23) is the correction with respect to T_N , the noise power originating from

the shunt resistor on the circulator. It enters the equation with a coefficient $|\Gamma|^2$, and since the MAR features appear at a low resistance close to or at 50Ω , its variation cannot be neglected. During the measurement of sample B, the shunt was mounted on the still plate at $T_N = 800$ mK instead of $T_N = 3$ K during the measurement of sample A, which might explain the reduced amplitude of the MAR in the noise signal. At higher bias, where $\frac{dR_d}{dV} = 0$, the data with and without corrections are equal. A problem for the calculation of the corrections for nonlinear

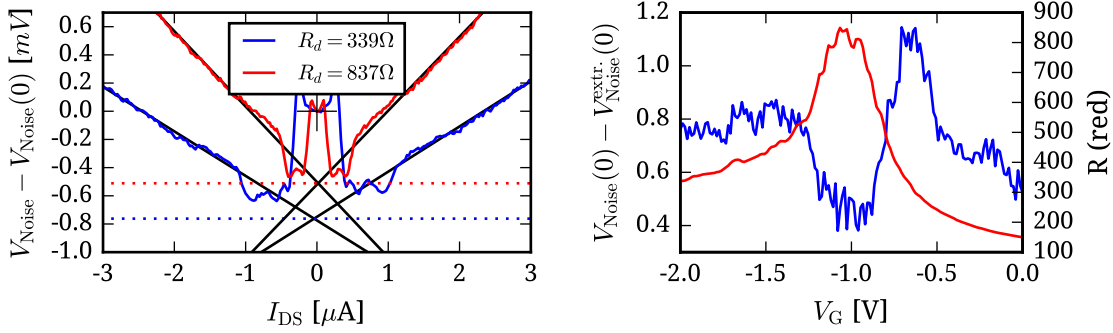


Figure 4.50: Using the noise in the superconducting state as a reference point, the effect of the variation of $|\Gamma|^2$ can be clearly seen. **Left:** The noise background of the curves at high bias is lower than the noise in the superconducting state. **Right:** The difference between the background noise at high bias, extracted by extrapolation of the linear part, and the zero bias noise in the superconducting state and the sample resistance are plotted versus the gate voltage, showing the variation of the background noise by varying R_d

IVs is finding the correct value for the noise power originating from the shunt resistor that actually reaches the sample, where it is reflected. We can try to estimate it by considering the noise at zero bias in the superconducting state as a fixed reference, where $R_d \equiv 0$, $|\Gamma|^2 = 1$ and all of T_N is reflected. The measured noise background $T_{\text{Noise}} = T_N + T_0$ (contributions by shunt resistor and constant addition by the amplifier) becomes constant and maximal. This behavior can be seen in the DC measured data in fig. 4.45, where V_{Noise} is indeed increased at zero bias when the sample turns superconducting. The additional noise cannot originate from the sample, it must be caused by reflection of thermal noise. The left panel of 4.50 shows a plot of V_{Noise} at two different gate settings, i.e. for two different values for R_d . The noise in the superconducting state was subtracted, it serves as a reference for the maximum background noise level. By extrapolating the curve from high bias to zero, we can find the noise baseline of $T_{\text{Noise}} = T_0 + |\Gamma|^2 T_N$ at the given sample resistance R_d . The shift between the two curves shows the relatively large influence of Γ in this particular measurement. The difference of the noise background level at high bias (i.e. finite R_d) and in the superconducting state depends on R_d , and the relation can be made visible by plotting the shift of the noise baseline versus sample resistance R_d , as shown in 4.51. The data can be fitted with $T_N \approx 0.1$ K, $T_0 \approx 1.4$ K, which indicates that T_N is reduced compared to the shunt temperature.

In conclusion, both samples show very strong MAR oscillations in the conductance, which confirm a high transparency. The bare noise signal shows clear signs of noise suppression at the positions of the MAR, which can be explained with the high transparency in a theoretical toy model. However, the influence of spurious thermal noise that is reflected at the sample with a resistance-dependent coefficient Γ^2 might be superimposed with the shot noise signal and could

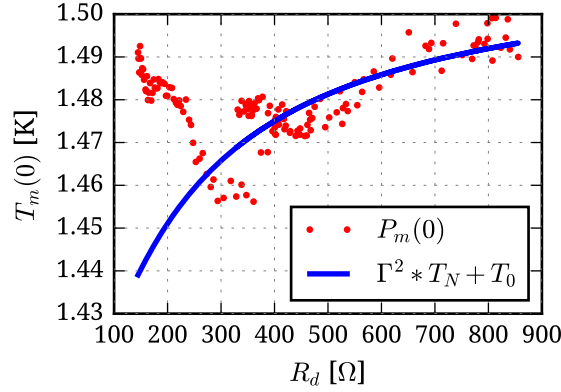


Figure 4.51: Variation of the noise background level with the sample resistance R_d . The plot shows the difference of the noise background extracted by extrapolation from high bias and the noise in the superconducting state, offset by the mean noise in the superconducting state.

cause a similar pattern in the measured signal, depending on the values of the model parameters T_N and GBW. While a naïve estimation leads to an overcompensation of the signal, T_N might effectively be much smaller than expected from the shunt temperature, and further investigation is required. Furthermore, the sharp conductance dip outside of the gap (at ≈ 0.7 mV in fig. 4.45) barely affects the measured noise data, which indicates that the measured noise is in fact not as dependent on R_d as expected from the model. To reduce the effect of the variation of Γ^2 on the measured noise signal, in future measurements of samples with nonlinear IV characteristic, the shunt resistor should be placed at mixing chamber temperature.

CHAPTER 5

Summary and Outlook

In this thesis, conductance and shot noise measurements of hBN encapsulated graphene were presented. By adapting the residue free fabrication technique with one-dimensional edge contacts, as first demonstrated in [Wan13], samples showing ballistic transport over distances in the order of the sample dimensions were fabricated. The devices show a rich variety of physical phenomena, which were investigated by tuning the charge carrier density through global or local electrostatic gating, varying the perpendicular magnetic field, and the temperature.

The characterization in the normal state at low temperature showed clear Fabry-Pérot interference patterns, which indicate ballistic transport. In this regime, theory predicts “pseudodiffusive” transport at low charge carrier densities [Two06], i.e. ballistic graphene showing transport properties of diffusive metal, which is reflected by a density dependent Fano factor with $\mathcal{F} = 1/3$ and a minimum conductivity of $\sigma_{\min} = \frac{4e^2}{\pi h}$ at the Dirac point. The hBN encapsulated samples in this work seem to be predestined for the investigation of transport at low charge carrier density, but while ballistic transport was achieved, the measured shot noise level was much lower than expected from theory. The Fano factor, which was determined by comparison to simultaneously measured tunnel junction samples, was found to be only $\mathcal{F} \approx 0.016$ at the Dirac point, instead of $\mathcal{F} = \frac{1}{3}$. Similar values were found in measurements during three cool downs, using two graphene samples with different W/L ratios, at 4 K and at base temperature. This very small value is in disagreement with theory for both ballistic and diffusive transport in graphene. To exclude a problem of asymmetric attenuation of the sample and reference measurement lines, the attenuation of the setup was measured at room temperature, where both lines were found to be equal. Yet, the attenuation within the sample holder could not be measured, and it cannot be excluded that a bad connection only became noticeable after cooling down. Apart from the low absolute value, the Fano factor was found to be gate dependent with a maximum at the Dirac point. However, qualitatively similar to [Dan08], the gate dependence was weaker than expected from theory.

Due to the ambipolar field effect in graphene, electrostatic gates can introduce p-n junctions that act as mirrors for Dirac fermions, creating a Fabry-Pérot interferometer, where the Fermi wavelength can be tuned in either half of the sample by adjusting the bias voltage and the elec-

trostatic gates. These interference patterns reveal information about charge carrier dynamics and the effective size of the area affected by the local top gate.

Shot noise measurements on the graphene p-n junction were hampered by technical difficulties. Due to the failure of the reference sample, the shot noise data could not be calibrated accurately, and the calibration data of a previous cool down was used instead. Thus, the noise data for sample B cannot be directly compared to the unipolar sample A. While the noise background was similar to the previous measurement, the signal was found to be even smaller than before.

Within the bipolar regime, introducing a perpendicular magnetic field causes charge carrier trajectories to form “snake states” along the p-n interface, which lead to oscillations in the conductance with respect to tuning the cyclotron radius $r_C = \frac{\hbar\sqrt{\pi n}}{eB}$ by varying either the magnetic field or the charge carrier density. While the oscillations are small, the expected pattern of lines along curves of constant r_C could be clearly identified, which indicates ballistic transport on the length scale of the sample width ($W = 5 \mu\text{m}$) in sample B.

Further increasing the field, the sample enters the quantum Hall regime, and transport occurs solely through topologically protected, unidirectional edge states. In the unipolar regime, the two-terminal conductance shows Shubnikov-de Haas oscillations that allow extracting the exact gate efficiencies and charge carrier densities in the sample. The direction of edge states can be inverted using electrostatic gating in graphene due to the ambipolar field effect, which causes parallel states at either side of a p-n interface. Depending on the disorder in the sample, these edge states can mix at the interface, making it serve as an “electronic beam splitter”. The conductance data presented in this thesis shows partial mixing of only the lowest states in the top gated region, while additional states don’t contribute to the conductance.

At low temperature, the Ti/Al leads turn superconducting, and effects related to proximity induced superconductivity were investigated. The field dependence of the critical current can serve as a probe for the real space current distribution, which was found to be perfectly homogeneous in the non-top gated sample. Above the critical current, features of multiple Andreev reflection were observed both in the conductance and the shot noise measurements. However, the nonlinear conductance caused by MAR lead to changes in the coupling between the graphene sample and the noise measurement setup that may have distorted the measured signal. To discriminate effects of this varying coupling and actual changes in the noise signal, a model was employed, but further investigation is required.

With a more sensitive, fully functional noise detection, the conductance oscillation caused by the snake states at the p-n interface, as well as the partial mode-mixing in the quantum Hall regime should show a characteristic signature in the shot noise that would help to better understand the underlying mechanisms, especially the role of disorder. In photon optics, waveguides and beam splitters are the most fundamental building blocks. Charge carrier guiding through snake-states and edge-mode mixing can be seen as respective realizations for Dirac fermions, which may in the future be used for the fabrication of more sophisticated devices.

Acknowledgments

Many people have contributed to the completion of this thesis, both scientifically and through personal support. First, I would like to thank my doctoral advisor Prof. Hilbert von Löhneysen and Prof. Ralph Krupke for their continuous support and many interesting discussions. On a daily basis, my work was supervised Romain Danneau. I could always rely on his support and his door was always open. Additional support was given by Fan Wu, who taught me experimental DC and high frequency measurement techniques with much patience. I also owe a lot to my colleagues and former PhD candidates Renjun Du, Christian Benz, Julien Bordaz, and Pablo Robert.

The metal deposition was performed with support by Stefan Kolenda in the UHV evaporator of Detlef Beckmann. Mechanical parts of the measurement and transfer setups were produced with great precision by Michael Schlenker and his team.

I really enjoyed the international atmosphere at the Institute of Nanotechnology and I share a lot of good memories with many colleagues from all around the world who I had the pleasure to work with: Geethu Balachandran, Pranauv Balaji, Muraleetharan Boopathi, Marco Giambra, Saumya Gupta, Kristina Hönes, Simon Ketterer, Svetlana Khasminskaya, Nicolas Kurz, Jürgen Mathes, Himadri Pandey, Nayancee Pandey, Preeti Pandey, Felix Pyatkov, Chirojyoti Rava, Joachim Schönle, Ruby Singh, Maximillian Thürmer, Nicolai Walter, Julian Winter, Philipp Zukowsky. Special thanks go to Christian Benz and Rainer Kraft for proof reading this thesis.

This work was made using mostly open source software, and I'd like to thank the contributors to all of these projects as well: KLayout (<http://www.klayout.de>), used for the design of GDSII files for electron beam lithography; Gwyddion (<http://www.gwyddion.net>), used for analyzing AFM images; QTLab (<https://github.com/heeres/qtlab>), the basis for the software controlling our measurement setup; Python, Jupyter, NumPy, SciPy, pandas, gnuplot, and matplotlib, used for data analysis and plotting; Inkscape, Gimp, used for creating vector and raster graphics Lua \LaTeX , Texstudio, and Matthias Pospiech (<http://www.matthiaspospiech.de>), whose \LaTeX template served as basis for this document.

Finally, I would like to thank my parents and my siblings Anita and Dirk for their constant support throughout this endeavor.

Bibliography

- [Aba07] Abanin, D. A. and Leonid S. Levitov: ‘Quantized Transport in Graphene p-n Junctions in a Magnetic Field’. *Science* (Aug. 2007), vol. 317(5838): pp. 641–643 (cit. on pp. 67, 69).
- [Aba08] Abanin, Dmitry a. and Leonid S. Levitov: ‘Conformal invariance and shape-dependent conductance of graphene samples’. *Physical Review B - Condensed Matter and Materials Physics* (2008), vol. 78(3): pp. 1–9 (cit. on p. 62).
- [All15] Allen, Monica T., Oles Shtanko, Ion Cosma Fulga, A. R. Akhmerov, K. Watanabe, Takashi Taniguchi, Pablo Jarillo-Herrero, Leonid S. Levitov, and Amir Yacoby: ‘Spatially resolved edge currents and guided-wave electronic states in graphene’. *Nature Physics* (Nov. 2015), vol. (November): p. 1504.07630 (cit. on p. 77).
- [Ame14] Amet, F, J. R. Williams, K. Watanabe, T. Taniguchi, and D. Goldhaber-Gordon: ‘Selective Equilibration of Spin-Polarized Quantum Hall Edge States in Graphene’. *Physical Review Letters* (May 2014), vol. 112(19): p. 196601 (cit. on p. 67).
- [And64] Andreev, A F: ‘The thermal conductivity of the intermediate state in superconductors’. *Sov Phys JETP* (1964), vol. 19: pp. 1228–1231 (cit. on p. 11).
- [Ave96] Averin, D. and H. T. Imam: ‘Supercurrent Noise in Quantum Point Contacts’. *Physical Review Letters* (May 1996), vol. 76(20): pp. 3814–3817 (cit. on p. 82).
- [Bak87] Bak, Per, Chao Tang, and Kurt Wiesenfeld: ‘Self-organized criticality: An explanation of the 1/f noise’. *Physical Review Letters* (1987), vol. 59(4): pp. 381–384 (cit. on p. 13).
- [Bal13] Balandin, Alexander A.: ‘Low-frequency 1/f noise in graphene devices’. *Nature Nanotechnology* (Aug. 2013), vol. 8(8): pp. 549–555 (cit. on p. 13).
- [Bar57] Bardeen, J., L. N. Cooper, and J. R. Schrieffer: ‘Theory of superconductivity’. *Physical Review* (1957), vol. 108(5): pp. 1175–1204 (cit. on p. 9).
- [Bee08] Beenakker, C. W. J.: ‘Colloquium : Andreev reflection and Klein tunneling in graphene’. *Reviews of Modern Physics* (Oct. 2008), vol. 80(4): pp. 1337–1354 (cit. on p. 73).
- [Bee92] Beenakker, CWJ and M Büttiker: ‘Suppression of shot noise in metallic diffusive conductors’. *Physical Review B* (1992), vol. 46(3): pp. 1889–1892 (cit. on p. 20).

- [Bez99] Bezuglyi, E. V., E. N. Bratus', V. S. Shumeiko, and G. Wendin: 'Multiple Andreev Reflections and Enhanced Shot Noise in Diffusive Superconducting-Normal-Superconductor Junctions'. *Physical Review Letters* (Sept. 1999), vol. 83(10): pp. 2050–2053 (cit. on p. 82).
- [Bla00] Blanter, Ya.M. and M Büttiker: 'Shot noise in mesoscopic conductors'. *Physics Reports* (Sept. 2000), vol. 336(1-2): pp. 1–166 (cit. on pp. 15, 16, 18, 20).
- [Bol08] Bolotin, KI, KJ Sikes, Z Jiang, M Klima, G. Fudenberg, J. Hone, P. Kim, and H.L. Stormer: 'Ultrahigh electron mobility in suspended graphene'. *Solid State Communications* (June 2008), vol. 146(9-10): pp. 351–355 (cit. on pp. 51, 66).
- [Bor13] Bordaz, Julien: 'Proximity-induced superconductivity in single-layer and bilayer graphene'. PhD thesis. Karlsruhe Institute of Technology, 2013 (cit. on pp. 23, 31).
- [Büt92] Büttiker, M.: 'Role of scattering amplitudes in frequency-dependent current fluctuations in small conductors'. *Physical Review B* (Feb. 1992), vol. 45(7): pp. 3807–3810 (cit. on p. 18).
- [Cal15] Calado, V E, S Goswami, G Nanda, M Diez, A R Akhmerov, Kenji Watanabe, Takashi Taniguchi, T M Klapwijk, and L M K Vandersypen: 'Ballistic Josephson junctions in edge-contacted graphene'. *Nature Nanotechnology* (July 2015), vol. 10(9): pp. 761–764 (cit. on pp. 49, 50, 73).
- [Cam05] Camino, F. E., V. V. Kuznetsov, E. E. Mendez, Th Sch??pers, V. A. Guzenko, and H. Hardtdegen: 'Shot noise of large charge quanta in superconductor/semiconductor/ superconductor junctions'. *Physical Review B - Condensed Matter and Materials Physics* (2005), vol. 71(2): pp. 2–5 (cit. on p. 82).
- [Cas09] Castro Neto, A. H., F. Guinea, N. M. R. Peres, K. S. Novoselov, and A. K. Geim: 'The electronic properties of graphene'. *Reviews of Modern Physics* (Jan. 2009), vol. 81(1): pp. 109–162 (cit. on pp. 4, 5).
- [Che06] Cheianov, Vadim V. and Vladimir I. Fal'ko: 'Selective transmission of Dirac electrons and ballistic magnetoresistance of n-p junctions in graphene'. *Physical Review B* (July 2006), vol. 74(4): p. 041403 (cit. on p. 57).
- [Che07] Cheianov, Vadim V., Vladimir Fal'ko, and B. L. Altshuler: 'The Focusing of Electron Flow and a Veselago Lens in Graphene p-n Junctions'. *Science* (Mar. 2007), vol. 315(5816): pp. 1252–1255 (cit. on p. 51).
- [Cho11] Cho, Sungjae and Michael Fuhrer: 'Massless and massive particle-in-a-box states in single- and bi-layer graphene'. *Nano Research* (Apr. 2011), vol. 4(4): pp. 385–392 (cit. on pp. 51, 52).
- [Cou08] Court, N. A., A. J. Ferguson, and R. G. Clark: 'Energy gap measurement of nanostructured aluminium thin films for single Cooper-pair devices'. *Superconductor Science and Technology* (2008), vol. 21(1): p. 015013 (cit. on p. 79).
- [Cro01] Cron, R., M. F. Goffman, D. Esteve, and C. Urbina: 'Multiple-Charge-Quanta Shot Noise in Superconducting Atomic Contacts'. *Physical Review Letters* (Apr. 2001), vol. 86(18): pp. 4104–4107 (cit. on p. 82).

- [Cue99a] Cuevas, J. C., A. Martín-Rodero, and a. Levy Yeyati: ‘Shot Noise and Coherent Multiple Charge Transfer in Superconducting Quantum Point Contacts’. *Physical Review Letters* (May 1999), vol. 82(20): pp. 4086–4089 (cit. on p. 82).
- [Cue99b] Cuevas, Juan Carlos: ‘Electronic Transport in Normal and Superconducting Nanostructures’. PhD thesis. Universidad Autónoma de Madrid, 1999: p. 265 (cit. on p. 11).
- [Dan08] Danneau, R., F. Wu, MF F. Craciun, S. Russo, M. Y. Tomi, J. Salmilehto, a. F. Morpurgo, and P. J. Hakonen: ‘Shot Noise in Ballistic Graphene’. *Physical Review Letters* (May 2008), vol. 100(19): p. 196802 (cit. on pp. 1, 48, 49, 87).
- [Das11a] Das Sarma, S., Shaffique Adam, E. H. Hwang, and Enrico Rossi: ‘Electronic transport in two-dimensional graphene’. *Reviews of Modern Physics* (May 2011), vol. 83(2): pp. 407–470 (cit. on p. 5).
- [Das11b] Das Sarma, S. and E. H. Hwang: ‘Conductivity of graphene on boron nitride substrates’. *Physical Review B* (Mar. 2011), vol. 83(12): p. 121405 (cit. on p. 49).
- [Dea10] Dean, C R, A F Young, I Meric, C Lee, L Wang, S. Sorgenfrei, K. Watanabe, T. Taniguchi, P. Kim, K L Shepard, and J. Hone: ‘Boron nitride substrates for high-quality graphene electronics’. *Nature Nanotechnology* (2010), vol. 5(10): pp. 722–726 (cit. on pp. 1, 21, 23, 47).
- [Dec11] Decker, Régis, Yang Wang, Victor W Brar, William Regan, Hsin-Zon Tsai, Qiong Wu, William Gannett, Alex Zettl, and Michael F Crommie: ‘Local Electronic Properties of Graphene on a BN Substrate via Scanning Tunneling Microscopy’. *Nano Letters* (June 2011), vol. 11(6): pp. 2291–2295 (cit. on p. 49).
- [DiC08] DiCarlo, L., J. Williams, Yiming Zhang, D. McClure, and C. Marcus: ‘Shot Noise in Graphene’. *Physical Review Letters* (Apr. 2008), vol. 100(15): p. 156801 (cit. on pp. 1, 48, 49).
- [Die97] Dieleman, P., H. G. Bukkems, T. M. Klapwijk, M. Schicke, and K. H. Gundlach: ‘Observation of Andreev Reflection Enhanced Shot Noise’. *Physical Review Letters* (Nov. 1997), vol. 79(18): pp. 3486–3489 (cit. on p. 82).
- [Dol77] Dolan, G. J.: ‘Offset masks for liftoff photoprocessing’. *Applied Physics Letters* (1977), vol. 31(5): pp. 337–339 (cit. on p. 28).
- [Du15] Du, Renjun: ‘Quantum transport in bilayer graphene van der Waals heterostructures’. PhD thesis. Karlsruhe Institute of Technology, 2015 (cit. on p. 23).
- [Du08] Du, Xu, Ivan Skachko, Anthony Barker, and Eva Y. Andrei: ‘Approaching ballistic transport in suspended graphene’. *Nature Nanotechnology* (2008), vol. 3(8): pp. 491–495 (cit. on pp. 47, 51, 73).
- [Dyn71] Dynes, R. C. and T. A. Fulton: ‘Supercurrent density distribution in josephson junctions’. *Physical Review B* (1971), vol. 3(9): pp. 3015–3023 (cit. on p. 77).
- [Gei13] Geim, A.K. and I. V. Grigorieva: ‘Van der Waals heterostructures’. *Nature* (July 2013), vol. 499(7459): pp. 419–425 (cit. on p. 21).

- [Gio08] Giovannetti, G., P. a. Khomyakov, G. Brocks, V. M. Karpan, J. Van Den Brink, and P. J. Kelly: ‘Doping graphene with metal contacts’. *Physical Review Letters* (2008), vol. 101(2): pp. 3–6 (cit. on p. 52).
- [Gla09] Glattli, D. C.: ‘Quantum shot noise of conductors and general noise measurement methods’. *The European Physical Journal Special Topics* (June 2009), vol. 172(1): pp. 163–179 (cit. on p. 32).
- [Goe11] Goerbig, M.: ‘Electronic properties of graphene in a strong magnetic field’. *Reviews of Modern Physics* (Nov. 2011), vol. 83(4): pp. 1193–1243 (cit. on p. 8).
- [Gro10] Gross, Rudolf and Achim Marx: *Applied Superconductivity*. München, 2010 (cit. on p. 9).
- [Gro14] Gross, Rudolf and Achim Marx: *Festkörperphysik*. 2. Auflage. De Gruyter, 2014: p. 1006 (cit. on p. 79).
- [Gru13] Grushina, Anya L, Dong-keun Ki, and Alberto F Morpurgo: ‘A ballistic pn junction in suspended graphene with split bottom gates’. *Applied Physics Letters* (2013), vol. 102(22): p. 223102 (cit. on p. 51).
- [Hai12] Haigh, S. J., A. Gholinia, R. Jalil, S. Romani, L. Britnell, D. C. Elias, K. S. Novoselov, L. A. Ponomarenko, A. K. Geim, and R. Gorbachev: ‘Cross-sectional imaging of individual layers and buried interfaces of graphene-based heterostructures and superlattices’. *Nature Materials* (2012), vol. 11(9): pp. 764–767 (cit. on p. 25).
- [Har14] Hart, Sean, Hechen Ren, Timo Wagner, Philipp Leubner, Mathias Mühlbauer, Christoph Brüne, Hartmut Buhmann, Laurens W. Molenkamp, and Amir Yacoby: ‘Induced superconductivity in the quantum spin Hall edge’. *Nature Physics* (2014), vol. 10(September): pp. 1–10 (cit. on p. 77).
- [Hee07] Heersche, Hubert B, Pablo Jarillo-Herrero, Jeroen B Oostinga, Lieven M K Vandersypen, and Alberto F Morpurgo: ‘Bipolar supercurrent in graphene’. *Nature* (Mar. 2007), vol. 446(7131): pp. 56–59 (cit. on p. 73).
- [Hos00] Hoss, T, C Strunk, T Nussbaumer, R Huber, U Staufer, and C. Schönenberger: ‘Multiple Andreev reflection and giant excess noise in diffusive superconductor/normal-metal/superconductor junctions’. *Physical Review B* (Aug. 2000), vol. 62(6): pp. 4079–4085 (cit. on p. 82).
- [Ihn10] Ihn, Thomas: *Semiconductor Nanostructures: Quantum states and electronic transport*. Oxford University Press, 2010: p. 580 (cit. on p. 13).
- [Jeh00] Jehl, X., M. Sanquer, R. Calemczuk, and D. Mailly: ‘Detection of doubled shot noise in short normal-metal/ superconductor junctions’. *Nature* (May 2000), vol. 405(6782): pp. 50–53 (cit. on p. 19).
- [Joh25] Johnson, J. B.: ‘The Schottky effect in low frequency circuits’. *Physical Review* (1925), vol. 26(1): pp. 71–85 (cit. on p. 13).
- [Joh27] Johnson, J. B.: ‘Thermal Agitation of Electricity in Conductors’. *Physical Review* (July 1927), vol. 2984(119): pp. 97–109 (cit. on p. 14).

- [Jon97] Jong, M. J. M. and C W J Beenakker: ‘Shot Noise in Mesoscopic Systems’. *Mesoscopic Electron Transport*. Ed. by Kouwenhoven, L. P., L. L. Sohn, and Gerd Schoen. Dordrecht: Springer Netherlands, Nov. 1997: pp. 225–258 (cit. on p. 19).
- [Kat11] Katsnelson, Mikhail I.: ‘Quantum Transport via Evanescent Waves in Undoped Graphene’. *Journal of Computational and Theoretical Nanoscience* (2011), vol. 8(6): pp. 912–918 (cit. on p. 48).
- [Kat06a] Katsnelson, Mikhail I.: ‘Zitterbewegung, chirality, and minimal conductivity in graphene’. *The European Physical Journal B* (May 2006), vol. 51(2): pp. 157–160 (cit. on p. 48).
- [Kat06b] Katsnelson, Mikhail I., K S Novoselov, and A K Geim: ‘Chiral tunnelling and the Klein paradox in graphene’. *Nature Physics* (Aug. 2006), vol. 2(9): pp. 620–625 (cit. on pp. 2, 6, 57).
- [Khl87] Khlus, VA a: ‘Current and voltage fluctuations in microjunctions between normal metals and superconductors’. *Sov Phys JETP* (1987), vol. 66(6): p. 1243 (cit. on p. 18).
- [Kle29] Klein, O.: ‘Die Reflexion von Elektronen an einem Potentialsprung nach der relativistischen Dynamik von Dirac’. *Zeitschrift für Physik* (1929), vol. 53(3-4): pp. 157–165 (cit. on p. 6).
- [Kli15] Klimov, Nikolai N., Son T. Le, J. Yan, Pratik Agnihotri, Everett Comfort, Ji Ung Lee, David B. Newell, and Curt A. Richter: ‘Edge-state transport in graphene p-n junctions in the quantum Hall regime’. *Physical Review B* (Dec. 2015), vol. 92(24): p. 241301 (cit. on p. 67).
- [Kre14] Kretinin, A V et al.: ‘Electronic Properties of Graphene Encapsulated with Different Two-Dimensional Atomic Crystals’. *Nano Letters* (June 2014), vol. 14(6): pp. 3270–3276 (cit. on p. 50).
- [Kum15] Kumada, N., F. D. Parmentier, H. Hibino, D. C. Glatli, and P. Roulleau: ‘Shot noise generated by graphene p–n junctions in the quantum Hall effect regime’. *Nature Communications* (2015), vol. 6: p. 8068 (cit. on p. 68).
- [Kum96] Kumar, A, L Saminadayar, D. C. Glatli, Y. Jin, and B. Etienne: ‘Experimental Test of the Quantum Shot Noise Reduction Theory’. *Physical Review Letters* (Apr. 1996), vol. 76(15): pp. 2778–2781 (cit. on p. 19).
- [Lan98] Landauer, Rolf: ‘Condensed-matter physics: The noise is the signal’. *Nature* (Apr. 1998), vol. 392(6677): pp. 658–659 (cit. on p. 12).
- [Lan41] Landon, V.D.: ‘The Distribution of Amplitude with Time in Fluctuation Noise’. *Proceedings of the IRE* (Feb. 1941), vol. 29(2): pp. 50–55 (cit. on p. 13).
- [Lee15] Lee, Gil-Ho, Geon-hyoung Park, and Hu-jong Lee: ‘Observation of negative refraction of Dirac fermions in graphene’. *Nature Physics* (Sept. 2015), vol. 11(11): pp. 925–929 (cit. on p. 51).
- [Les89] Lesovik, G B: ‘Excess quantum noise in 2D ballistic point contacts’. *ZhETF Pis ma Redaktsiiu* (1989), vol. 49: p. 513 (cit. on p. 19).

- [Lew08] Lewenkopf, C. H., E. R. Mucciolo, and A. H. Castro Neto: ‘Numerical studies of conductivity and Fano factor in disordered graphene’. *Physical Review B - Condensed Matter and Materials Physics* (2008), vol. 77(8): pp. 3–6 (cit. on pp. 49, 50).
- [Lie94] Liefink, F, J. I. Dijkhuis, M. J. M. de Jong, L. W. Molenkamp, and H. van Houten: ‘Experimental study of reduced shot noise in a diffusive mesoscopic conductor’. *Physical Review B* (May 1994), vol. 49(19): pp. 14066–14069 (cit. on p. 20).
- [Loh09] Lohmann, Timm, Klaus von Klitzing, and Jurgen H Smet: ‘Four-Terminal Magneto-Transport in Graphene p-n Junctions Created by Spatially Selective Doping’. *Nano Letters* (May 2009), vol. 9(5): pp. 1973–1979 (cit. on p. 67).
- [Low09] Low, Tony: ‘Ballistic-Ohmic quantum Hall plateau transition in graphene pn junction’. *Physical Review B* (Aug. 2009), vol. 80(20): p. 205423 (cit. on p. 67).
- [Mac15] Machida, Tomoki, Sei Morikawa, Satoru Masubuchi, Rai Moriya, Miho Arai, Kenji Watanabe, and Takashi Taniguchi: ‘Edge-Channel Transport of Dirac Fermions in Graphene Quantum Hall Junctions’. *Journal of the Physical Society of Japan* (Dec. 2015), vol. 84(12): p. 121007 (cit. on p. 68).
- [Mat15] Matsuo, Sadashige, Shunpei Takeshita, Takahiro Tanaka, Shu Nakaharai, Kazuhito Tsukagoshi, Takahiro Moriyama, Teruo Ono, and Kensuke Kobayashi: ‘Edge mixing dynamics in graphene p–n junctions in the quantum Hall regime’. *Nature Communications* (Sept. 2015), vol. 6: p. 8066 (cit. on pp. 67, 69).
- [May11] Mayorov, Alexander S., Roman V. Gorbachev, Sergey V. Morozov, Liam Britnell, Rashid Jalil, Leonid A. Ponomarenko, Peter Blake, Kostya S. Novoselov, Kenji Watanabe, Takashi Taniguchi, and A. K. Geim: ‘Micrometer-scale ballistic transport in encapsulated graphene at room temperature.’ *Nano letters* (June 2011), vol. 11(6): pp. 2396–9 (cit. on pp. 1, 21).
- [Mia07] Miao, F., S. Wijeratne, Y. Zhang, U. C. Coskun, W. Bao, and C. N. Lau: ‘Phase-coherent transport in graphene quantum billiards.’ *Science (New York, N.Y.)* (Sept. 2007), vol. 317(5844): pp. 1530–3 (cit. on pp. 51, 52).
- [Miz13] Mizuno, Naomi, Bent Nielsen, and Xu Du: ‘Ballistic-like supercurrent in suspended graphene Josephson weak links.’ *Nature communications* (2013), vol. 4: p. 2716 (cit. on p. 73).
- [Moh11] Mohrmann, Jens: ‘Herstellung von Feldeffektanordnungen mit sehr glatten Graphen-Lagen’. Diplomarbeit. Karlsruhe Institute of Technology, 2011 (cit. on p. 23).
- [Mos14] Mostovov, Andrey: ‘Quantum Shot Noise in Graphene’. PhD thesis. Université Pierre et Marie Curie - Paris VI, 2014 (cit. on pp. 1, 48, 49).
- [Nav99] Naveh, Y. and D. V. Averin: ‘Nonequilibrium Current Noise in Mesoscopic Disordered Superconductor–Normal-Metal–Superconductor Junctions’. *Physical Review Letters* (May 1999), vol. 82(20): pp. 4090–4093 (cit. on p. 82).
- [Nie76] Niemeyer, J. and V. Kose: ‘Observation of large dc supercurrents at nonzero voltages in Josephson tunnel junctions’. *Applied Physics Letters* (1976), vol. 29(6): p. 380 (cit. on p. 28).

- [Nie74] Niemeyer, Jürgen: ‘Eine einfache Methode zur Herstellung kleiner Josephson-Elemente’. *PTB-Mitteilungen* (1974), vol. 84: p. 251 (cit. on p. 28).
- [Nov05a] Novoselov, Kostya S., Andre K. Geim, Sergey V. Morozov, D. Jiang, M I Katsnelson, I V Grigorieva, SV V Dubonos, and AA A Firsov: ‘Two-dimensional gas of massless Dirac fermions in graphene’. *Nature* (Nov. 2005), vol. 438(7065): pp. 197–200 (cit. on p. 8).
- [Nov04] Novoselov, Kostya S., Andre K. Geim, Sergey V. Morozov, D Jiang, Y Zhang, S V Dubonos, I V Grigorieva, and A A Firsov: ‘Electric field effect in atomically thin carbon films.’ *Science (New York, N.Y.)* (Oct. 2004), vol. 306(5696): pp. 666–9 (cit. on p. 22).
- [Nov05b] Novoselov, Kostya S., D Jiang, F Schedin, T J Booth, V V Khotkevich, S V Morozov, and A K Geim: ‘Two-dimensional atomic crystals’. *Proceedings of the National Academy of Sciences* (July 2005), vol. 102(30): pp. 10451–10453 (cit. on p. 21).
- [Nyq28] Nyquist, H.: ‘Thermal Agitation of Electric Charge in Conductors’. *Physical Review* (July 1928), vol. 32(1): pp. 110–113 (cit. on p. 14).
- [Per10] Peres, N.: ‘Colloquium: The transport properties of graphene: An introduction’. *Reviews of Modern Physics* (2010), vol. 82(3): pp. 2673–2700 (cit. on p. 7).
- [DeP98] De-Picciotto, R., M. Reznikov, M. Heiblum, V. Umansky, G. Bunin, and D. Mahalu: ‘Direct observation of a fractional charge’. *Physica B: Condensed Matter* (June 1998), vol. 249-251(September): pp. 395–400 (cit. on pp. 19, 20).
- [Pos94] Post, N. van der, E. T. Peters, I. K. Yanson, and J. M. van Ruitenbeek: ‘Subgap Structure as Function of the Barrier in Atom-Size Superconducting Tunnel Junctions’. *Physical Review Letters* (Nov. 1994), vol. 73(19): pp. 2611–2613 (cit. on p. 79).
- [Poz12] Pozar, David M.: *Microwave Engineering*. 2012 (cit. on pp. 14, 36).
- [Rei02] Reich, S, J Maultzsch, C Thomsen, and P. Ordejón: ‘Tight-binding description of graphene’. *Physical Review B* (July 2002), vol. 66(3): p. 035412 (cit. on p. 4).
- [Rei08] Reina, Alfonso, Hyungbin Son, Liying Jiao, Ben Fan, Mildred S. Dresselhaus, Zhong-Fan Liu, and Jing Kong: ‘Transferring and Identification of Single- and Few-Layer Graphene on Arbitrary Substrates’. *Journal of Physical Chemistry C* (Nov. 2008), vol. 112(46): pp. 17741–17744 (cit. on p. 21).
- [Rez95] Reznikov, M., M. Heiblum, Hadas Shtrikman, and D. Mahalu: ‘Temporal Correlation of Electrons: Suppression of Shot Noise in a Ballistic Quantum Point Contact’. *Physical Review Letters* (1995), vol. 75(18): pp. 3340–3343 (cit. on p. 19).
- [Ric15a] Rickhaus, Peter, Ming-Hao Liu, Péter Makk, Romain Maurand, Samuel Hess, Simon Zihlmann, Markus Weiss, Klaus Richter, and Christian Schönenberger: ‘Guiding of Electrons in a Few-Mode Ballistic Graphene Channel’. *Nano Letters* (Sept. 2015), vol. 15(9): pp. 5819–5825 (cit. on p. 51).
- [Ric15b] Rickhaus, Peter, Péter Makk, Ming-Hao Liu, Endre Tóvári, Markus Weiss, Romain Maurand, Klaus Richter, and Christian Schönenberger: ‘Snake trajectories in ultra-clean graphene p–n junctions’. *Nature Communications* (2015), vol. 6: p. 6470 (cit. on pp. 51, 59, 61).

- [Ric13] Rickhaus, Peter, Romain Maurand, Ming-Hao Liu, Markus Weiss, Klaus Richter, and Christian Schönenberger: ‘Ballistic interferences in suspended graphene.’ *Nature communications* (2013), vol. 4: p. 2342 (cit. on p. 51).
- [Rod07] Roddaro, S, P Pingue, V Piazza, V Pellegrini, and F Beltram: ‘The Optical Visibility of Graphene: Interference Colors of Ultrathin Graphite on SiO₂’. *Nano Letters* (Sept. 2007), vol. 7(9): pp. 2707–2710 (cit. on p. 22).
- [Sam97] Saminadayar, L., D. Glattli, Y. Jin, and B. Etienne: ‘Observation of the $e/3$ Fractionally Charged Laughlin Quasiparticle’. *Physical Review Letters* (1997), vol. 79(13): pp. 2526–2529 (cit. on pp. 19, 20).
- [Sch13] Schmidt, H., J. C. Rode, C. Belke, D. Smirnov, and R. J. Haug: ‘Mixing of edge states at a bipolar graphene junction’. *Physical Review B* (Aug. 2013), vol. 88(7): p. 075418 (cit. on p. 67).
- [Sch18] Schottky, Walter: ‘Über spontane Stromschwankungen in verschiedenen Elektrizitätsleitern’. *Annalen der Physik* (1918), vol. 362(23): pp. 541–567 (cit. on pp. 14, 15).
- [She94] Sherman, Robert: ‘Surface cleaning with the carbon dioxide snow jet’. *Journal of Vacuum Science & Technology A: Vacuum, Surfaces, and Films* (July 1994), vol. 12(4): p. 1876 (cit. on p. 22).
- [Sho98] Shon, Nguyen Hong and Tsuneya Ando: ‘Quantum Transport in Two-Dimensional Graphite System’. *Journal of the Physics Society Japan* (July 1998), vol. 67(7): pp. 2421–2429 (cit. on p. 7).
- [Spi03] Spietz, Lafe, K. W. Lehnert, I Siddiqi, and Rob J Schoelkopf: ‘Primary electronic thermometry using the shot noise of a tunnel junction.’ *Science (New York, N.Y.)* (June 2003), vol. 300(5627): pp. 1929–32 (cit. on pp. 18, 19).
- [Ste96] Steinbach, Andrew H., John M. Martinis, and Michel H. Devoret: ‘Observation of Hot-Electron Shot Noise in a Metallic Resistor’. *Physical Review Letters* (May 1996), vol. 76(20): pp. 3806–3809 (cit. on p. 20).
- [Tan07] Taniguchi, T. and K. Watanabe: ‘Synthesis of high-purity boron nitride single crystals under high pressure by using Ba-BN solvent’. *Journal of crystal growth* (2007), vol. 303(2): pp. 525–529 (cit. on pp. 21, 22).
- [Tay15] Taychatanapat, Thiti, Jun You Tan, Yuting Yeo, Kenji Watanabe, Takashi Taniguchi, and Barbaros Özyilmaz: ‘Conductance oscillations induced by ballistic snake states in a graphene heterojunction’. *Nature Communications* (Feb. 2015), vol. 6: p. 6093 (cit. on p. 59).
- [Thü12] Thürmer, Maximilian: ‘Towards a set-up for shot-noise measurements at microwave frequencies in mesoscopic graphene structures’. Diplomarbeit. Karlsruhe Institute of Technology, 2012 (cit. on p. 32).
- [Tit06] Titov, M. and C. W J Beenakker: ‘Josephson effect in ballistic graphene’. *Physical Review B - Condensed Matter and Materials Physics* (2006), vol. 74(4): pp. 1–4 (cit. on p. 74).

- [Two06] Tworzydo, J., B. Trauzettel, M. Titov, A. Rycerz, and C.W.J. W. J. Beenakker: ‘Sub-Poissonian Shot Noise in Graphene’. *Physical Review Letters* (June 2006), vol. 96(24): p. 246802 (cit. on pp. 7, 48, 49, 87).
- [Vak11] Vakil, A. and N. Engheta: ‘Transformation Optics Using Graphene’. *Science* (June 2011), vol. 332(6035): pp. 1291–1294 (cit. on p. 51).
- [Wal47] Wallace, P.R.: ‘The band theory of graphite’. *Physical Review* (1947), vol. 71(9): pp. 622–634 (cit. on p. 4).
- [Wan13] Wang, L., I. Meric, P. Y. Huang, Q. Gao, Y. Gao, H. Tran, T. Taniguchi, K. Watanabe, L. M. Campos, D. A. Muller, J. Guo, P. Kim, J. Hone, K. L. Shepard, and C. R. Dean: ‘One-dimensional electrical contact to a two-dimensional material.’ *Science (New York, N.Y.)* (Nov. 2013), vol. 342(6158): pp. 614–7 (cit. on pp. 1, 21, 23, 25, 47, 87).
- [Wat04] Watanabe, Kenji, Takashi Taniguchi, and Hisao Kanda: ‘Direct-bandgap properties and evidence for ultraviolet lasing of hexagonal boron nitride single crystal.’ *Nature materials* (June 2004), vol. 3(6): pp. 404–9 (cit. on pp. 21, 22).
- [Wil07] Williams, J. R., L. DiCarlo, and C. M. Marcus: ‘Quantum Hall Effect in a Gate-Controlled p-n Junction of Graphene’. *Science* (Aug. 2007), vol. 317(5838): pp. 638–641 (cit. on p. 67).
- [Wil11] Williams, J. R. and C. M. Marcus: ‘Snake states along graphene p-n junctions’. *Physical Review Letters* (2011), vol. 107(4): pp. 1–4 (cit. on p. 59).
- [Wil09] Williams, J., D. Abanin, L. DiCarlo, L. Levitov, and C. Marcus: ‘Quantum Hall conductance of two-terminal graphene devices’. *Physical Review B* (July 2009), vol. 80(4) (cit. on p. 62).
- [Wu07] Wu, F., P. Queipo, A. Nasibulin, T. Tsuneta, T. H. Wang, E. Kauppinen, and P. J. Hakonen: ‘Shot Noise with Interaction Effects in Single-Walled Carbon Nanotubes’. *Physical Review Letters* (Oct. 2007), vol. 99(15): p. 156803 (cit. on pp. 32, 38).
- [Ye95] Ye, P D, D Weiss, R R Gerhardtts, M Seeger, K von Klitzing, K Ebert, and H Nickel: *Electron in a Periodic Magnetic Field Induced by a Regular Array of Micromagnets*. 1995 (cit. on p. 59).
- [You09] Young, Andrea F. and Philip Kim: ‘Quantum interference and Klein tunnelling in graphene heterojunctions’. *Nature Physics* (Feb. 2009), vol. 5(3): pp. 222–226 (cit. on pp. 6, 51, 53).
- [Zha05] Zhang, Yuanbo, Yan-wen Tan, Horst L Stormer, and Philip Kim: ‘Experimental Observation of Quantum Hall Effect and Berry’s Phase in Graphene’. *Nature* (Sept. 2005), vol. 438(7065): pp. 201–204 (cit. on pp. 8, 22).

